UNIVERSITY OF CALIFORNIA,
IRVINE

Microfluidic Technology for Cell Engineering and Analysis

DISSERTATION

submitted in partial satisfaction of the requirements
for the degree of

DOCTOR OF PHILOSOPHY

in Biomedical Engineering

by

Mohammad Aghaamoo

Dissertation Committee:
Professor Abraham P. Lee, Chair
Professor Wendy Liu
Professor Weian Zhao

2021

DEDICATION

To

my parents, sister, and friends

in recognition of their unconditional love and unending support.

TABLE OF CONTENTS

LIST OF FIGURES

Page

LIST OF TABLES

LIST OF MOVIES

ACKNOWLEDGMENTS

I would like to thank and express the deepest appreciation to my advisor and committee chair, Prof. Abraham P. Lee, for all his endless support during my PhD studies. With his encouragement, positive criticism, and support, I became a better researcher, experimentalist, and person. During my PhD studies, Dr. Lee always encouraged me to explore new things without being afraid of failure. Not only he taught me valuable skills to become an independent researcher, but he also showed me how to be a team builder to tackle multidisciplinary scientific projects. Without Dr. Lee's guidance and support, this dissertation would not have been possible. Aside from scientific and academic help, I am very grateful for Dr. Lee's emotional support. As an international student living thousands of miles away from my home, Dr. Lee and his lovely family were always there for me and my other lab members.

I gratefully acknowledge the members of my committee, Prof. Wendy Liu, Prof. Weian Zhao, Prof. Suzanne Sandmeyer, and Prof. Jered Haun. Their valuable inputs and suggestions during my PhD qualifying examination significantly helped me to better prioritize and shape my research projects.

My sincerest gratitude to all the fantastic members of the BioMiNT Lab. I have been fortunate to be in this wonderful lab and learn so many skills from each individual researcher. Especially, I would like to thank Joy (Yu-Hsi) Chen for her enormous contribution to the intracellular delivery project. While I was struggling with further developing the AESOP technology, her addition to the project was a game changer. I would like to thank my dear friends, Dr. Xuan Li and Dr. Neha Garg, for all their help that made me a better researcher.

Especially, they were instrumental in developing the concept of the AESOP intracellular delivery technology. I want to thank Dr. G. K. Kurup and Marzieh Ataei for all their great support and contribution to the droplet-encapsulation project. I would also like to thank Roy Jiang and Braulio Cardenas Benitez for their major contribution to the dielectrophoresis (DEP)-based sorting project. I am grateful to Dr. Dohyun Lee for teaching me the fundamental skills for the DEP-based microfluidic technology. I am also very thankful to Alan Jiang. He was one of the first persons who taught me how to perform microfluidic and DEP experiments.

Each one of my projects is the result of multiple collaborations and for that, I want to thank Center for Advanced Design and Manufacturing of Integrated Microfluidics (CADMIM) and Dr. Gisela Lin for introducing me and exposing me to incredible opportunities. I am also sincerely grateful to Dr. Yue Yun, the former lead of Transformational Technologies at Corteva Agriscience (the agricultural division of DowDuPont), who has been a great supporter and mentor to me.

In addition, I want to express my respect and gratitude to the staffs in the UCI Integrated Nanosystems Research Facility (INRF). Microfabrication is an integral part of microfluidic technology. Their enormous help and technical support facilitated developments of many of our projects.

Aside from scientific and academic help and encouragement from people who I mentioned above, I am extremely thankful to my parents, sister, and friends who have given me tremendous mental and emotional support. Spending more than 5 years without seeing your child/brother is not an easy task for any family member. Therefore, I am even more profoundly thankful of them and am hoping to see them again soon!

CURRICULUM VITAE

Mohammad Aghaamoo

Education

2008-2013 B.S. in Mechanical Engineering
University of Tehran, Tehran, Iran

2014-2016 M.S. in Mechanical Engineering
Wahington State University Vancouver, Vancouver, WA, USA

2016-2021 Ph.D. in Biomedical Engineering
University of California, Irvine, CA, USA

Honors and Scholarship

2019 University of California Irvine 2019 Grad Slam Top-Ten Finalists

2021-2022 NIH-funded TL1 Post-Doctoral Training Award
The Institute for Clinical and Translational Science
University of California, Irvine, CA, USA

Work Experience

June 2019 – September 2019 Summer Intern in Advanced Engineering
Illumina, Inc., Foster City, CA, USA

Patent

US. 11052395B2 & WO2020041463A1, A. P. Lee, **M. Aghaamoo**, X. Li, N. Garg, and Y.H. Chen, "Lateral cavity acoustic transducer (LCAT) for shear-induced cell transfection"

Selected Peer-Reviewed Journal Publications (* co-first author)

M. Aghaamoo*, Y. H. Chen*, X. Li, N. Garg, R. Jiang, and A. P. Lee, "High-throughput and dosage-controlled intracellular delivery of large cargos by an acoustic-electric micro-vortices platform," Advanced Science (2021), In press

G. Kamalakshakurup*, **M. Aghaamoo***, M. Ataei, N. Zhang, and A. P. Lee, "Shear-dependent microvortices in liquid–liquid flow-focusing geometry: A theoretical, numerical, and experimental study," Physics of Fluids 33, 032016 (2021).

R. Jiang, S. Agrawal, **M. Aghaamoo**, R. Parajuli, A. Agrawal, and A. P. Lee, "Rapid isolation of circulating cancer associated fibroblasts by acoustic microstreaming for assessing metastatic propensity of breast cancer patients," Lab on a Chip 21, 875 (2021)

A. Y. L. Jiang, A. R. Yale, **M. Aghaamoo**, D. H. Lee, A. P. Lee, T. N. G. Adams, and L. A. Flanagan, "High-throughput continuous dielectrophoretic separation of neural stem cells," Biomicrofluidics 13, 064111 (2019)

N. Ma, G. Kamalakshakurup, **M. Aghaamoo**, A. P. Lee, and M. A. Digman, "Label-Free Metabolic Classification of Single Cells in Droplets Using the Phasor Approach to Fluorescence Lifetime Imaging Microscopy," Cytometry Part A 95, 93 (2019)

X. Li, **M. Aghaamoo**, S. Liu, D.-H. Lee, and A. P. Lee, "Lipoplex-Mediated Single-Cell Transfection via Droplet Microfluidics," Small 14, 1802055 (2018)

A. P. Lee, **M. Aghaamoo**, T. N. G. Adams, and L. A. Flanagan, "It's Electric: When Technology Gives a Boost to Stem Cell Science," Current Stem Cell Reports 4, 116 (2018).

Selected Peer-Reviewed Conference Publications

Y. H. Chen, **M. Aghaamoo**, C.W. Hughes, and A. P. Lee, "An Acoustic-Electrical Microfluidic Platform for mRNA-Based Cell Engineering", 25th International Conference on Miniaturized Systems for Chemistry and Life Sciences (MicroTAS 2021), October 10-14, 2021

M. Ataei, **M. Aghaamoo**, G.K. Kurup, and A. P. Lee, "Theoretical, Computational and Experimental Characterization of Shear-Dependent Micro-Vortices in Liquid—Liquid Flow-Focusing Geometry", 25th International Conference on Miniaturized Systems for Chemistry and Life Sciences (MicroTAS 2021), October 10-14, 2021

L. R. McGrale, S. N. Munoz, Y. H. Chen, **M. Aghaamoo**, and A. P. Lee, "Lateral Cavity Acoustic Transducer (LCAT) Platform for Studying Mechanical Properties of Cells", 25th International Conference on Miniaturized Systems for Chemistry and Life Sciences (MicroTAS 2021), October 10-14, 2021

M. Aghaamoo, R. Jiang, B. Cardenas. A. P. Lee, "A Microfluidic 3-Part Differential Sorter", 24th International Conference on Miniaturized Systems for Chemistry and Life Sciences (MicroTAS 2020), October 4-9, 2020

Y. H. Chen, **M. Aghaamoo**, and A. P. Lee, "An Acoustic-Electrical Shear Opening Poration (AESOP) Platform for Intracellular Delivery", 24th International Conference on Miniaturized Systems for Chemistry and Life Sciences (MicroTAS 2020), October 4-9, 2020

M. Aghaamoo, N. Garg, X. Li, and A. P. Lee, "A Multimodal Transfection Device for High Efficiency, Intracellular Delivery of Biomolecules", 23rd International Conference on Miniaturized Systems for Chemistry and Life Sciences (MicroTAS 2019), Basel, Switzerland, October 27-31, 2019

G.K. Kurup, **M. Aghaamoo**, and A. P. Lee, "Controlled One Cell-One Bead Encapsulation in Droplets by Liquid-Liquid Interfacial Shearing", 21st International Conference on Miniaturized Systems for Chemistry and Life Sciences (MicroTAS 2017), Savannah, Georgia, USA, October 22-26, 2017

X. Li, **M. Aghaamoo**, S. Liu, A. P. Lee, "Lipoplex-mediated Efficient Single-cell Transfection via Droplet Microfluidics", 21st International Conference on Miniaturized Systems for Chemistry and Life Sciences (μTAS 2017), Savannah, U.S., October 22-26, 2017, pp 918-919

ABSTRACT OF THE DISSERTATION

Microfluidic Technology for Cell Engineering and Analysis

By

Mohammad Aghaamoo

Doctor of Philosophy in Biomedical Engineering

University of California, Irvine, 2021

Professor Abraham P. Lee, Chair

In recent years, cellular and gene therapies have been transforming medicine. With the 2018 Nobel Prize awarded to pioneers in the field of cancer immunotherapy, more and more advances in cell engineering are being developed to produce genetic-modified and reprogrammed cells for cellular and gene therapies. One promising category is *ex-vivo* cell/gene therapy in which the target cells are isolated from patients, the therapy is administrated to the cells outside of the body *in vitro*, and the cells are then transferred back into the body. However, challenges remain in terms of (i) isolating the target cells to be engineered, (ii) developments of efficient, safe, and controllable methods for intracellular delivery of gene-editing cargos, and (iii) development of efficient quality control (QC) approaches based on single-cell analysis of engineered cells. This dissertation is set out to develop microfluidic technologies to address the challenges in cell engineering and analysis. First, a high-throughput non-viral intracellular delivery platform is introduced for the transfection of large cargos with dosage-control. This platform, termed Acoustic-Electrical Shear Orbiting Poration (AESOP), optimizes the delivery of intended cargo sizes with

uniform poration of the cell membranes via mechanical shear followed by the modulated expansion of these nanopores via electric field. Furthermore, AESOP utilizes acoustic microstreaming vortices wherein up to millions of cells are trapped and mixed uniformly with exogenous cargos, enabling the delivery of cargos into cells with targeted dosages. With this platform, we demonstrated large-plasmid (>9kbp) transfection for CRISPR-Cas9 at 1 million cells/min per single chip.

Second, toward development of more efficient 1–1 droplet encapsulation methods for single-cell analysis, the mechanism of particle trapping and release at the flow-focusing microfluidic droplet generation junction, utilizing the hydrodynamic micro-vortices generated in the dispersed phase, is described. This technique is based solely on our unique flow-focusing geometry and the flow control of the two immiscible phases and, thus, does not require any on-chip active components. The effectiveness of this technique to be used for particle trapping and the subsequent size selective release into the droplets depends on the fundamental understanding of the nature of the vortex streamlines. Therefore, theoretical, computational, and experimental fluid dynamics were utilized to study in detail these micro-vortices and parameters affecting their formation, trajectory, and magnitude.

Third, an integrated microfluidic platform is presented that provides 3-part differential sorting of WBCs from whole blood. The proposed system accomplishes 3-part differential sorting of WBCs by: (1) On-chip lysis of RBCs from the blood sample, and (2) Downstream isolation of subpopulation of WBCs using dielectrophoresis (DEP) technology. The developed platform is capable of efficient isolation of viable monocytes, granulocytes, and lymphocytes from undiluted whole blood sample with volumes as low as 50 ul.

CHAPTER 1: INTRODUCTION

An overview of cellular and gene therapies

In recent years, cellular and gene therapies have been transforming medicine. To treat diseases, gene therapy replaces, inactivates, or introduces the genetic material (e.g., DNA or RNA) in the cells.[1] On the other hand, cellular therapy transfers healthy, restored, or altered cells into the body for treatment of diseases.[2] In some therapies, the two approaches are combined by genetically modifying specific types of cells and transferring them into the body. With the 2018 Nobel Prize awarded to pioneers in the field of cancer immunotherapy, more and more advances in cell engineering are being developed to produce genetic-modified and reprogrammed cells for cellular and gene therapies. So far, the U.S. Food and Drug Administration (FDA) has approved over twenty cellular and gene therapy products (Table 1.1) while many other clinical trials are currently being conducted.

Type	Proper name	Trade name	Manufacturer	Indication
ex-vivo cell/gene therapy (CAR-T immunotherapy)	idecabtagene vicleucel	ABECMA	Celgene Corporation, a Bristol-Myers Squibb Company	adult patients with relapsed or refractory multiple myeloma (MM)
	lisocabtagene maraleucel	BREYANZI	Juno Therapeutics, Inc., a Bristol-Myers Squibb Company	adult patients with relapsed or refractory large B-cell lymphoma
	tisagenlecleucel	KYMRIAH	Novartis Pharmaceuticals Corporation	pediatric and young adult patients (age 3-25 years) with B-cell precursor acute lymphoblastic leukemia (ALL)
	brexucabtagene autoleucel	TECARTUS	Kite Pharma, Inc.	adult patients with relapsed/refractory mantle cell lymphoma (r/r MCL)
	axicabtagene ciloleucel	YESCARTA	Kite Pharma, Inc.	adult patients with relapsed or refractory large B-cell lymphoma

Type	Proper name	Trade name	Manufacturer	Indication
ex-vivo cell/gene therapy (immunotherapy)	sipuleucel-T	PROVENGE	Dendreon Corporation	asymptomatic or minimally symptomatic metastatic castrate resistant (hormone refractory) prostate cancer
in-vivo gene therapy	talimogene laherparepvec	IMLYGIC	Amgen Inc.	patients with melanoma recurrent
	voretigene neparvovec-rzyl	LUXTURNA	Spark Therapeutics, Inc.	patients with confirmed biallelic RPE65 mutation-associated retinal dystrophy
	onasemnogene abeparvovec-xioi	ZOLGENSMA	AveXis, Inc	Spinal Muscular Atropy (Type 1)
Cell therapy	Allogeneic Cultured Keratinocytes and Fibroblasts in Bovine Collagen	GINTUIT	Organogenesis Incorporated	mucogingival conditions
	Laviv	Azficel-T	Fibrocell Technologies, Inc.	Moderate to severe nasolabial fold wrinkles in adults
	Autologous Cultured Chondrocytes on a Porcine Collagen Membrane	MACI	Vericel Corporation	symptomatic cartilage damage of the adult knee
	plasminogen, human-tvmh	RYPLAZIM	Prometic Biotherapeutics Inc.	patients with plasminogen deficiency type 1 (hypoplasminogenemia)
	allogeneic cultured keratinocytes and dermal fibroblasts in murine collagen-dsat	STRATAGRAFT	Stratatech Corporation	adults with thermal burns containing intact dermal elements
Stem cell therapy	HPC, Cord Blood	ALLOCORD	SSM Cardinal Glennon Children's Medical Center	disorders affecting the hematopoietic system

Type	Proper name	Trade name	Manufacturer	Indication
Stem cell therapy	HPC, Cord Blood	Clevecord	Cleveland Cord Blood Center	disorders affecting the hematopoietic
	HPC, Cord Blood	Ducord	Duke University School of Medicine	disorders affecting the hematopoietic
	HPC, Cord Blood	Hemacord	New York Blood Center, Inc	disorders affecting the hematopoietic
	HPC, Cord Blood	None	MD Anderson Cord Blood Bank	disorders affecting the hematopoietic
	HPC, Cord Blood	None	Clinimmune Labs, University of Colorado Cord Blood Bank	disorders affecting the hematopoietic
	HPC, Cord Blood	None	LifeSouth Community Blood Centers, Inc.	disorders affecting the hematopoietic
	HPC, Cord Blood	None	Bloodworks	disorders affecting the hematopoietic

Table 1.1 List of FDA-approved cellular and gene therapy products

Overall, gene therapy can be classified into (i) *in-vivo* gene therapy: the therapy is administrated directly to the patient in the body, and (ii) *ex-vivo* cell/gene therapy: the target cells are isolated from patients, the therapy is administrated to the cells outside of the body *in vitro*, and the cells are then transferred back into the body. Luxturna and Zolgensma are two prominent FDA-approved *in-vivo* gene therapy products for treatment of patients with Biallelic RPE65 mutation-associated retinal dystrophy and children less than two years of age with spinal muscular atrophy (SMA), respectively.[3, 4] On the other hand, chimeric antigen receptors (CAR)-T cell immunotherapy is one type of *ex-vivo* cell/gene therapy that has already achieved success in the clinic showing tremendous promise for cancer treatment.[5] For example, in two of these products, Kymriah and Yescarta, the patient's own cells are reprogrammed to attack children's advanced leukemia and adult lymphoma, respectively.[6] Besides cell therapy, cells can be reprogrammed to biomanufacture antibodies and other proteins for therapeutics. It can be used to deliver the powerful gene editing technology - the

clustered regularly interspaced short palindromic repeats (CRISPR)–associated protein-9 (Cas9) nuclease - to further modify or improve engineered cell products.[5] Moreover, cell reprogramming can have a significant impact on basic research in cell and molecular biology to produce cell lines, for studying molecular pathways, and understanding progenitors and stem cells.

Intracellular delivery of gene-editing molecules: a key step in gene and cell-based therapies

Intracellular delivery is an important yet challenging step in gene and cell-based therapies,[7-9] biomanufacturing,[10, 11] and basic research (e.g. cell biology, drug discovery, and genetics). To reprogram cells, various methods have been adopted for delivery of gene-editing cargos into cells (Fig. 1.1). Viral vectors are the most widely intracellular delivery method adopted in clinical applications due to their high efficiency and specificity. However, key challenges remain in terms of cytotoxicity, immunogenicity, risk of insertional toxicity, manufacturing, and limited packaging capacity.[12] They also require specific cell surface receptors for intracellular entry. Methods based on cationic lipids or polymers relies on lipoplexes or polyplexes (complexes they form with DNA) merging with the cell membranes and entering the cells by endocytosis. Cationic lipids and polymers are among attractive non-viral candidates to replace viral methods, as they cause lower adverse immune responses and have the potential for low-cost and large-scale production. Nevertheless, low delivery efficiency for suspension cells and concerns over cytotoxicity are two major obstacles for these synthetic vectors.[13, 14] Bulk electroporation is another popular non-viral method for intracellular delivery. Despite its success in delivery of wide range of cargos into most types

of cell, including hard-to-transfect cells, high cell mortality is still a major challenge.[15-17] In addition, due to their bulk nature, cationic lipids/polymers and electroporation do not offer uniform and dosage-controlled delivery across cell population.[18] Tables 1 is a general summary of the conventional transfection methods.

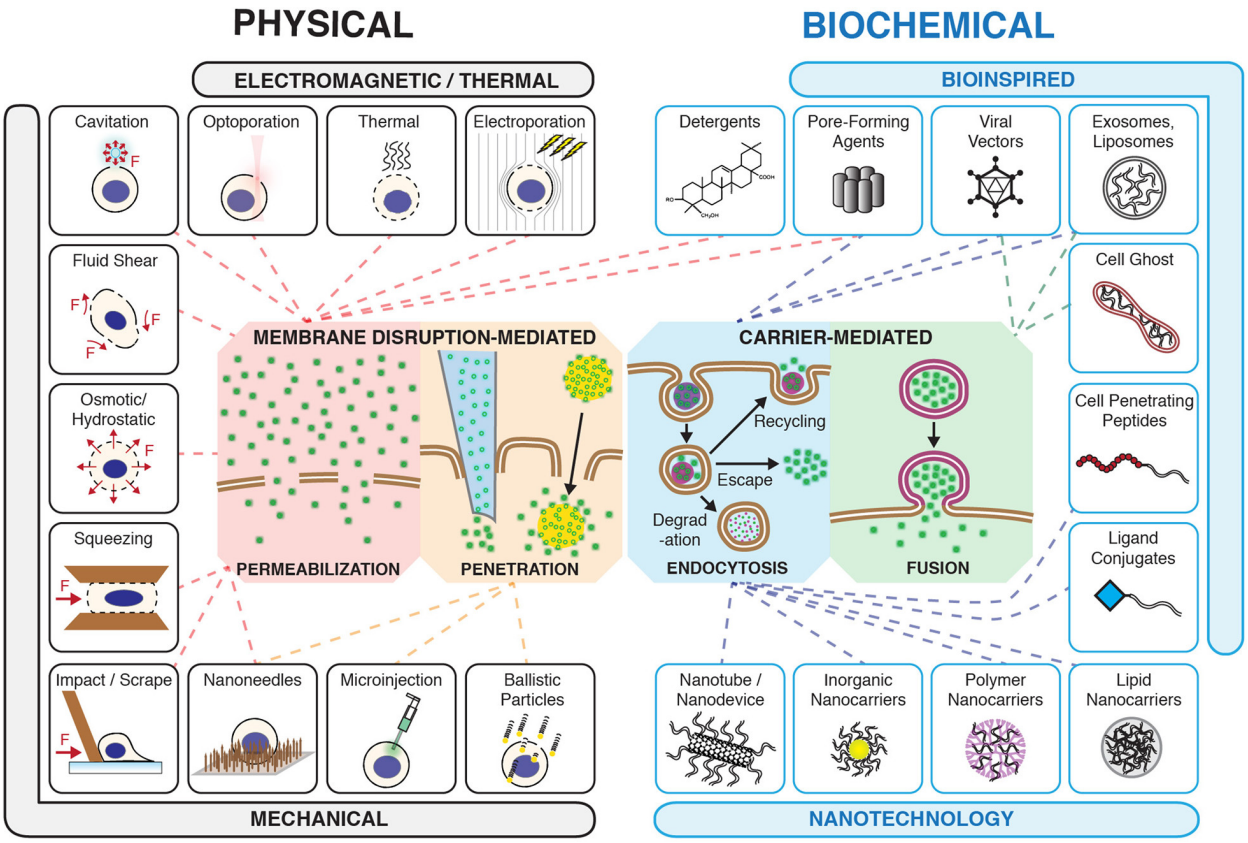

Figure 1.1 Different methods developed for intracellular delivery of gene-editing cargos. Reprinted (adapted) with permission from ref (19).[19] Copyright © 2018 American Chemical Society.

To address the challenges facing viral and conventional non-viral techniques, microfluidics and nanotechnology have appeared as powerful tools that have shown tremendous potential for adoption in clinical settings and research labs.[19] Notable examples include methods based on cell deformation,[20-23] nanostructures for localized electroporation,[18, 24-26] mechanoporation,[27, 28] acoustofluidics sonoporation,[29] flow-through electroporation,[30] droplet microfluidics,[31, 32] and inertial microfluidics.[28, 33] For safe, efficient, and controllable

intracellular delivery, these methods focus on precise control of cellular permeabilization and uptake, down to the single-cell level. To achieve this, cells are usually treated in a 1D or 2D manner. 1D methods flow cells one-by-one and/or usually have channel dimensions at the scale of single cells,[20, 28-31] while 2D methods are based on monolayer cell culturing or cell interaction with a substrate.[18, 24-27] Particularly, several existing micro- and nanotechnology methods have adopted such strategies to outperform viral and conventional non-viral techniques in (i) dosage-controlled delivery,[18, 33-37] which enables the cell population to receive the right concentration of cargo and, thus, minimizes overdose and underdose intracellular delivery, and (ii) intracellular delivery of large cargos,[21, 25, 38-40] which plays a key role in many genome-editing approaches such as those using CRISPR-Cas9 technology. However, these methods are either low in throughput, limited to specific cell types (e.g., adherent vs. suspension cells), or complicated to operate with. Thus, there is a great need for gene transfection technologies that are safe, efficient, and with controlled delivery of target materials into the cells.[31]

Droplet microfluidics for quality control and single-cell analysis of cellular and gene therapy products

Quality control (QC) testing is an integral part of cellular and gene therapy products.[41] In addition to compliance with current good manufacturing practice (CGMP), QC also utilizes wide range of analytical and biological approaches to ensure the manufactured genetic-modified and reprogrammed cells are safe, effective, potent, pure, and stable.[42] Examples include flow cytometry,[43] mass cytometry,[44] single-cell RNA sequencing (scRNA-seq),[45] digital polymerase chain reaction (PCR),[46] cytotoxicity assays,[47] etc. In recent years, droplet

microfluidics has positively impacted QC of gene therapy products by improving methods such as scRNA-seq and digital PCR. For example, precise quantification and analysis of vector copy number (VCN) in targeted cells is important in evaluating the safety and effectiveness of the therapy. While cells with zero or few VCN may not have effective therapeutic effects, the ones with high VPN are potentially toxic to the body. Unlike real-time PCR, droplet digital PCR (ddPCR) have shown to be more precise with a wider dynamic range.[48] ddPCR has been utilized to measure the VCN in QC of gene therapies including CAR-T cell immunotherapy[49] and stem cell gene therapy.[50, 51] Moreover, droplet microfluidic technology has evolved into a powerful platform for performing single cell analysis,[52] nucleic acid sequencing,[53, 54] and cytotoxicity screening[55] of manufactured cell products. Most of these applications require controlled confinement of cells, particles, and biomolecules in pL-nL droplets. Therefore, cell/particle manipulation techniques are essential to achieve these operations. Generally, particle manipulation techniques can be classified into active or passive control designs. Active techniques include dielectrophoretic,[56,57] magnetophoretic,[58] acoustophoretic,[59,60] thermophoretic[61] and optical methods.[62,63] These techniques require active components such as electrodes and actuators to perform the operation.[64,65] In contrast, passive techniques do not require additional on-chip transducers, and rely on hydrodynamic flow control that include inertial,[66,67,68] viscoelastic,[69] pinched flow fractionation,[70] and gravitational fields.[71,72] Passive single cell/particle encapsulation in droplets is realized by both deterministic and non-deterministic methods.[73] In non-deterministic methods, single cell encapsulation in droplets is often dictated by Poisson statistics. Non-uniform spatial distribution and random arrival time of cells at the droplet generation junction often add uncertainty to whether a droplet contain a single cell, multiple cells or no cells at all.[74] Within

the Poisson regime, the cell concentration and the relative flow rates of the dispersed and continuous phase is typically optimized to achieve improved single cell encapsulation efficiency. On the other hand, the deterministic methods leverage unique hydrodynamic flow control techniques to overcome the Poisson hurdle.[75] One such technique employs Rayleigh-Plateau instability jet breakup where the cell-encapsulated droplets have a larger diameter than the empty droplets. Using lateral induced drift and steric interactions between the droplets at the bifurcation, larger droplets with single cells are sorted at 79.2% efficiency.[76] Another technique utilizes Rayleigh-Plateau instability jet breakup along with DLD (Deterministic Lateral Displacement) pillar arrays to sort large-sized single-cell encapsulated droplets from the small empty ones.[77] High efficiency single cell encapsulation can also be achieved using inertial ordering. Incorporating a long, high aspect ratio microchannel[78] or a spiral channel[79] upstream improves the single cell encapsulation efficiency up to 80%. However, the requirement of high cell concentration and the need to synchronize the ordered cells with the droplet generation rate adds complexity to the technique. To perform single cell encapsulation at low cell concentrations and when the sample contains various-sized cells or particles, the techniques listed above often fall short.

Isolation and enrichment of target cells: An essential step in *ex-vivo* cell/gene therapies

Efficient isolation of target cells from patients is another important step in *ex-vivo* cell/gene therapies. For example, Strimvelis, a European Commission (EC) approved stem cell gene therapy for treatment of patients with severe combined immunodeficiency due to adenosine deaminase deficiency (ADA-SCID), requires isolation of CD34+ cells from patient's bone

marrow.[80] In CAR-T cell immunotherapy, efficient isolation of T cells plays a key role in efficacy of manufacturing CAR-T cells.[41] In a process, called leukapheresis, peripheral blood mononuclear cells (PBMCs) are isolated from the patient's blood. Then, the isolated PBMCs can be further processed for enrichment of T cells and, depending on the type of CAR-T cell therapy, into specific sub-population of T cells (e.g., $CD4^+$, $CD8^+$) by magnetic-based enrichment techniques. In some cases, leukapheresis and downstream genetic modification can be challenging. Depending on different factors such as underlying diseases, prior treatments, timing of cell collection, etc. patients may have lower count of PBMCs or T cells that are affected phenotypically and genotypically.[81-83] Therefore, developing an efficient method capable of isolation of different subpopulation of WBCs (specifically T cells) from small volume of patient's blood (down to a drop) for pre-screening and analysis could potentially benefit CAR-T cell therapy in improving both cell collection as well as downstream genetic modification. The capability to process small volume of blood is especially highly advantageous for cases where drawing large volume of blood is sometimes not feasible for cancer patients with critical conditions.

Research Aims

This dissertation is set out to develop microfluidic technologies to address key challenges in cellular and gene therapies by: (i) Development of an acoustic-electric micro-vortices platform for high-throughput and dosage-controlled intracellular delivery of large cargos, (ii) Development of more efficient 1–1 droplet encapsulation methods by theoretical, numerical, and experimental study of shear-dependent microvortices in liquid–liquid flow-focusing geometry, and (iii) Development of a dielectrophoresis (DEP)-based microfluidic 3-

part differential sorter for isolation of three major subpopulations of white blood cells (WBCs) (lymphocytes, monocytes and granulocytes) from undiluted whole blood.

Accordingly, in chapter 2, a high-throughput non-viral intracellular delivery platform is introduced for the transfection of large cargos with dosage-control. This platform, termed Acoustic-Electrical Shear Orbiting Poration (AESOP), optimizes the delivery of intended cargo sizes with uniform poration of the cell membranes via mechanical shear followed by the modulated expansion of these nanopores via electric field. Furthermore, AESOP utilizes acoustic microstreaming vortices wherein up to millions of cells are trapped and mixed uniformly with exogenous cargos, enabling the delivery of cargos into cells with targeted dosages. Intracellular delivery of a wide range of molecule sizes (<1 kDa to 2 MDa) with high efficiency (>90%), cell viability (>80%) and uniform dosages (<60% Coefficient of Variance (CV)) simultaneously into 1 million cells/min per single chip was demonstrated. AESOP was successfully applied to two gene editing applications that require the delivery of large plasmids: i) eGFP plasmid (6.1 kbp) transfection, and ii) CRISPR-Cas9-mediated gene knockout using a 9.3 kbp plasmid DNA encoding Cas9 protein and sgRNA. Compared to alternative platforms, this platform offers dosage-controlled intracellular delivery of large plasmids simultaneously to large populations of cells while maintaining cell viability at comparable delivery efficiencies.

In chapter 3, the mechanism of particle trapping and release at the flow-focusing microfluidic droplet generation junction, utilizing the hydrodynamic microvortices generated in the dispersed phase, is described. This technique is based solely on our unique flow-focusing geometry and the flow control of the two immiscible phases and, thus, does not require any on-chip active components. The effectiveness of this technique to be used for particle

trapping and the subsequent size selective release into the droplets depends on the fundamental understanding of the nature of the vortex streamlines. Therefore, theoretical, computational, and experimental fluid dynamics were utilized to study in detail these microvortices and parameters affecting their formation, trajectory, and magnitude. The presented theoretical and CFD study supported by experimental results provide detailed understanding of shear-dependent microvortices in liquid–liquid flow-focusing designs, which can be used for developing more efficient 1–1 droplet encapsulation methods.

In chapter 4, an integrated microfluidic platform is presented that provides 3-part differential sorting of WBCs from whole blood. The proposed system accomplishes 3-part differential sorting of WBCs by: (1) On-chip lysis of RBCs from the blood sample, and (2) Downstream isolation of subpopulation of WBCs using DEP technology. The developed platform is capable of efficient isolation of viable monocytes, granulocytes, and lymphocytes from undiluted whole blood sample with volumes as low as 50 ul.

CHAPTER 2: HIGH-THROUGHPUT AND DOSAGE-CONTROLLED INTRACELLULAR DELIVERY OF LARGE CARGOS BY AN ACOUSTIC-ELECTRIC MICRO-VORTICES PLATFORM

Introduction

Non-viral intracellular delivery of cargos that can rival viral vectors in throughput, viability, and uniformity is an elusive goal for the field of cell engineering. Many promising applications, such as CRISPR-Cas9 gene editing and the biomanufacturing of CAR T cells, rely on effective methods to uniformly deliver large cargos at precise doses across the cell membranes. However, current non-viral delivery solutions are capable of either precise delivery dosage control or high throughput processing but generally not both. Here, we present an Acoustic-Electrical Shear Orbiting Poration (AESOP) platform for intracellular delivery of a wide range of cargos with high efficiency, uniformity, cell viability, and throughput of 1 million cells/min per single chip. Compared to existing methods that offer intracellular delivery of large cargos and/or dosage-controlled capability, AESOP is an order of magnitude higher in throughput, compatible with both adherent and suspension cell types, and simple to operate. AESOP incorporates our lateral cavity acoustic transducer (LCAT) technology assisted by interdigitated array (IDA) electrodes for intracellular delivery (Fig. 2.1A-C, and Movie 2.1). Once the cells are introduced into the platform, they are consecutively trapped in the array of acoustic microstreaming vortices generated by the LCATs. Since delivery cargos are also pumped along with the cells, they uniformly mix with cells trapped in the microvortices. We hypothesize 3 underlying principles of our AESOP platform: (1) cells trapped in acoustic microstreaming vortices experience modest and

uniform mechanical shear near oscillating air-liquid interfaces that opens nanopores on their cell membranes; shear-induced cell membrane poration facilitates intracellular delivery of small molecules (<10KDa) into cells, is cell-dependent, and can be controlled by tuning acoustic transducers, (2) rapid tumbling of cells in the streaming orbits expose them to uniform strength electric fields that uniformly enlarges the pre-existing pores; for formation of large pores, our two-step membrane permeabilization strategy only requires gentle and low-strength electric fields that, alone, are not effective in the absence of microvortices, and (3) vortices induce chaotic mixing, enabling uniform, dosage-controlled and rapid delivery of exogenous materials into the cells.

We tested the performance of AESOP with different sizes of molecules, ranging from <1 kDa to 2 MDa, and obtained >90% delivery efficiency with >80% cell viability for both adherent and suspension cell lines. In the next step, we transfected HeLa, K562, and Jurkat cells with a green fluorescent protein (GFP)-expressing plasmid (pmaxGFP™, 3.5 kbp) and obtained high transfection efficiencies of >90%, >70%, and >60%, respectively, with >80% cell viability. To evaluate AESOP performance for intracellular delivery of large cargos, we first picked a 6.1 kbp enhanced green fluorescent protein (eGFP)-expressing plasmid, and could achieve >80%, >50%, and >40% transfection efficiency for HeLa, K562, and Jurkat cells, respectively, while still maintaining high cell viability of >80% for all these cell lines. Using AESOP platform, CRISPR-Cas9-mediated gene editing was demonstrated by a 9.3 kbp plasmid DNA encoding Cas9 and sgRNA to knockout PTEN gene in K562 cells. We showed >80% intracellular delivery of CRISPR plasmid and up to 20% gene knockout across cell population. The large size of the plasmid DNA for eGFP transfection (i.e. 6.1 kbp) and CRISPR-Cas9 gene knockout (i.e. 9.3 kbp) were chosen to challenge the packaging limit of some of

the common viral vectors including adeno-associated viruses (AAVs).[84] In AESOP, dosage-controlled delivery capability is achieved by the acoustic microstreaming vortices in the key steps of intracellular delivery: (i) membrane disruption: by uniform exposure to mechanical shear and electric field, and (ii) cellular uptake: by uniform mixing of cells with exogenous materials. Delivery analysis of YOYO 1-labelled plasmid DNA confirmed uniform and controllable intracellular delivery across cell population.

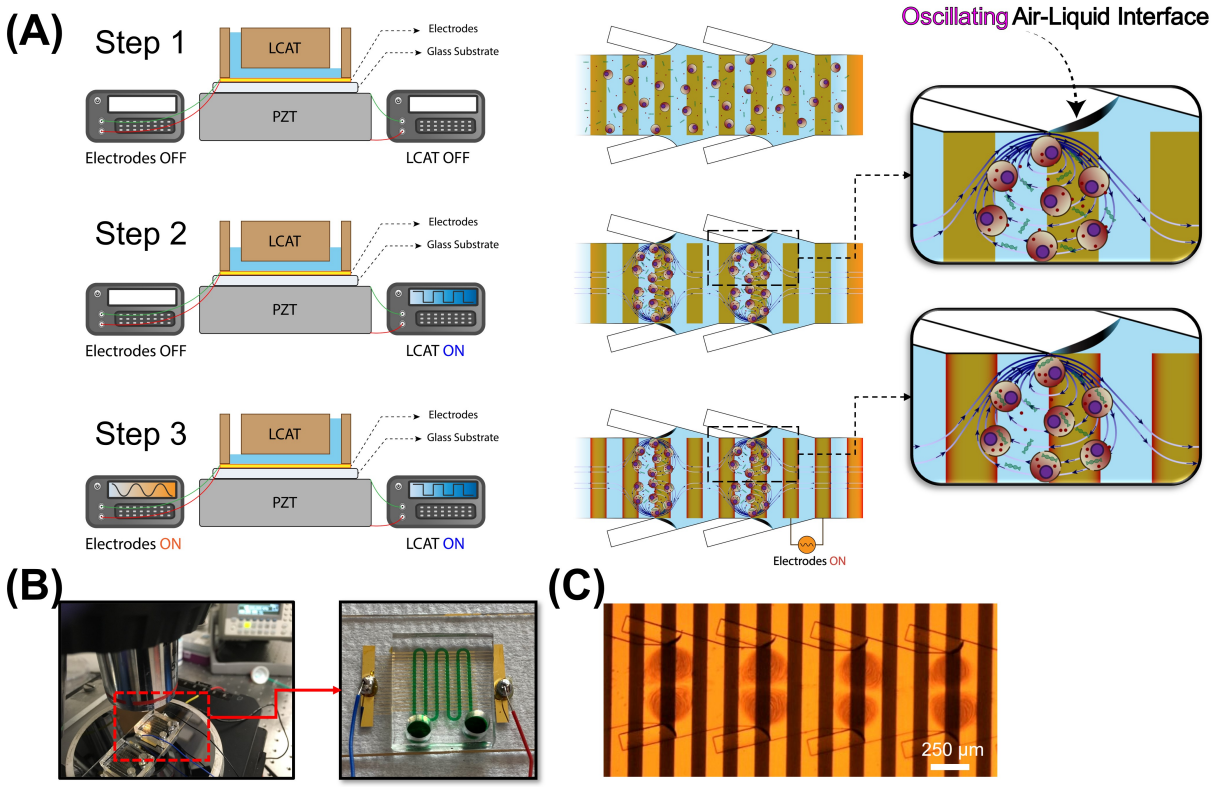

Figure 2.1 Design and operation of AESOP
(**A**) AESOP's operational principle is based on three steps: (1) loading the cells and cargos into the chip. Once the solution primes the main channel, air-liquid interfaces will be formed between the main and side channels. (2) Turning on LCAT by applying a resonating square-wave signal to a piezoelectric transducer underneath the chip. The acoustic wave, transmitted from the piezoelectric transducer to the chip, oscillates the air-liquid interfaces, resulting in formation of acoustic microstreaming vortices. The cells trapped in these vortices experience modest and uniform mechanical shear that creates nanopores on their membrane. (3) Uniform enlargement of pores by uniform exposure of the cells, rotating in vortices, to the electric field. The cargos are uniformly delivered into cells by chaotic mixing generated by acoustic microstreaming vortices (**B**) AESOP device setup, and (**C**) Microscope image of cells rotating in acoustic microstreaming vortices, on top of electrodes.

Compared to existing methods, our system not only can deliver a wide range of molecular sizes at high efficiency, viability, and uniformity, but it also offers unique sample processing advantages. For example, the unique design of LCATs generates a bulk flow that eliminates the need and complexity of external pumping. In addition, since cells are trapped and suspended in microstreaming vortices, the microfluidic channels are wider, making them higher throughput and less prone to clogging. Furthermore, we have demonstrated a single-chip AESOP platform at a relatively high throughput of up to 1 million cells/min per single chip. This scalability in throughput is relatively straightforward without reduction in system performance.

Results

Shear-induced cell membrane poration by acoustic microstreaming vortices

To eliminate the need for applying high electric fields for intracellular delivery, AESOP initiates nanopores on the cell membrane by mechanical shear and enlarges the pre-existing nanopores at lower electric field strengths. To achieve this, AESOP incorporates LCAT technology to trap cells inside acoustic microstreaming vortices and uniformly expose them to modest mechanical shear. The basic structure design of LCAT is illustrated in Fig. 2.2A consisting of a main fluid channel with slanted dead-end side channels. Once the main channel is primed with the sample, air-liquid interfaces are formed along the channel length. When placed on a piezoelectric transducer (PZT), the acoustic energy is transmitted to the air-liquid interfaces of LCATs, causing them to oscillate and generate microstreaming vortices in the microfluidic channel. The orientation and positioning of the air-liquid cavities result in both bulk flow liquid pumping and size-selective trapping of cells.[85, 86] The trapped

cells orbiting in these micro-vortices are subjected to oscillatory mechanical shear near the oscillating air-liquid interfaces. Based on the theory developed by Nyborg for acoustic microstreaming velocity near an oscillating bubble,[87] Rooney estimated the viscous shear stress near the bubble as

$$S = \frac{2\pi^{\frac{3}{2}}\epsilon_0^2(\rho f^3 \eta)^{\frac{1}{2}}}{R_0} \quad (2.1)$$

where ρ is the fluid density, η is the fluid shear viscosity, f is the oscillation frequency, R_0 is the bubble radius, and ϵ_0 is the displacement amplitude of the vibrating bubble (Movie 2.2, and Fig. S2, Supporting Information).[88-90] For the case of a moving cell rather than a stationary point near an oscillating bubble, equation (2.1) can be used to estimate the upper bound of shear stress. According to equation (2.1), the mechanical shear exerted on cells can be controlled by varying the interface oscillation amplitude excited by the PZT.

In the first step, particle tracking velocimetry (PTV) was employed to characterize micro-vortices and measure the velocity and trajectory of cells at different PZT applied voltages (Fig. 2.2C, D; Fig. S3 to S5, Supporting Information). For all three different cell types (HeLa, K562, Jurkat) tested, although the general patterns of microstreaming vortices are similar, higher number of Jurkat cells can be trapped per each vortex due to their smaller size (~1200 cells/vortex for Jurkat, ~700 cells/vortex for HeLa and K562). This results in formation of more streaming orbits for Jurkat cells per each vortex. The PTV results also indicate that the cells' maximum velocity is reached near the air-liquid interface (Fig. 2.2C), and its magnitude is directly proportional to the PZT applied voltage (Fig. 2.2D). In addition, by increasing the PZT applied voltage, the device pumping rate increases linearly (Fig. S6).

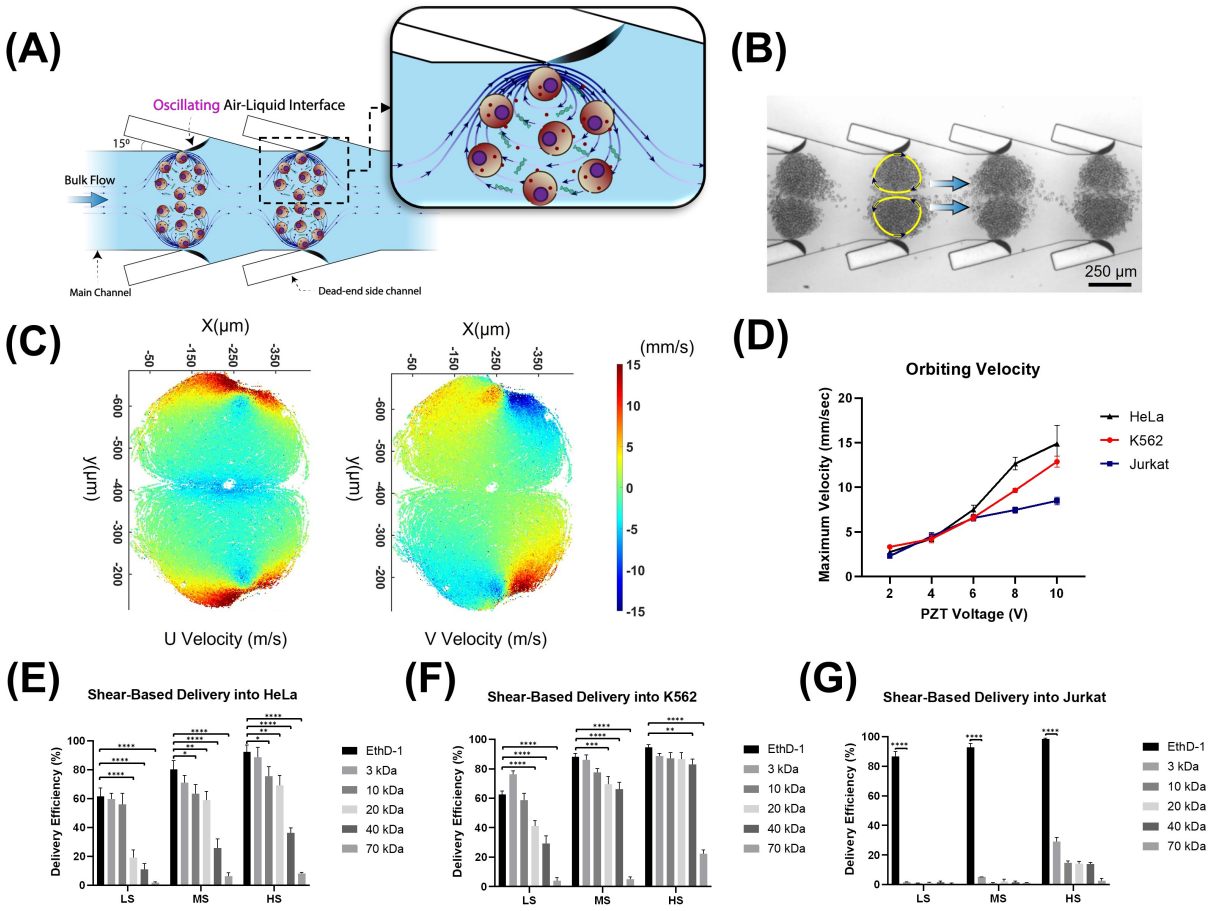

Figure 2.2 Shear-induced initiation of nanopores on cell membrane by acoustic microstreaming vortices

(**A**) Basic design structure of LCAT technology incorporated by AESOP for shear-induced small pore formation; LCATs are arrays of acoustically actuated air-liquid interfaces generated using dead-end side channels, (**B**) Microscope image of K562 cells trapped in acoustic microstreaming vortices generated by LCAT, (**C**) PTV analysis results of K562 cells orbiting in acoustic microstreaming vortices (PZT voltage= 6V), (**D**) Cells' maximum velocity orbiting in micro-vortices; the maximum velocity is reached near the air-liquid interface, and is proportional to the PZT applied voltage, (**E**-**G**) Shear-induced delivery of small molecules into (**E**) HeLa, (**F**) K562, and (**G**) Jurkat cells at three different operational modes: "low shear (LS)" (PZT voltage = 2V), "moderate shear (MS)" (PZT voltage = 6V), and "high shear (HS)" (PZT voltage = 10V). Quantitative data were presented as mean ± standard error (SE). For all experiments, sample size n=3. *P<0.05, **P<0.01, ***P<0.001, and ****P<0.0001 were determined by Tukey's honest significant difference criterion.

In the next step, we tested the hypothesis of using acoustic microstreaming vortices for shear-induced initiation of nanopores on cell membrane. For this purpose, we introduced cells (HeLa, K562, or Jurkat) with different molecules (EthD-1 dye (~857 Da) or fluorescein isothiocyanate–dextran with different sizes, ranging from 3 kDa to 70 kDa) into the chip and

activated the LCAT for 5 minutes (standard operation time of LCAT throughout this study). To evaluate the effect of mechanical shear force on intracellular delivery, we picked three different PZT applied voltages corresponding to "low shear (LS)" (PZT voltage = 2V, S_{LS} = 4.3 Pa), "moderate shear (MS)" (PZT voltage = 6V, S_{MS} = 69.4 Pa), and "high shear (HS)" (PZT voltage = 10V, S_{HS} = 272.9 Pa) (Movie 2.3; Supplementary Note 1, Supporting Information). Based on the results (Fig. 2.2E-G), there are four key findings: 1) Mechanical shear facilitates delivery of small molecules into the cells, indicating formation of nano-sized pores on the cells' membrane, 2) At a given shear rate, the delivery efficiency of larger cargos is lower than smaller cargos, 3) Increasing the shear increases the delivery efficiency of molecules into the cells by creating larger pores, 4) there exists a pore size threshold for shear-induced cell membrane poration; for the three shear modes (low, moderate, and high) tested, shear alone could not deliver >1kDa molecules into Jurkat cells and ≥70kDa molecules into HeLa and K562. Based on these results, the size of generated pores is mainly dependent on PZT applied voltage and cell type. Even though high shear mode provides higher delivery efficiency, for the rest of studies, we chose moderate shear (PZT voltage = 6V) as our optimum operational mode for LCAT. This mode offers effective small pore formation (>80% delivery efficiency for molecules up to 3 kDa in size for K562 and HeLa, and >90% delivery efficiency of ~857 Da EthD-1 dye for Jurkat). Importantly, in high-shear mode, we observed the cell viability to drop below 80% (Fig. 2.3). This is especially important because coupling with electric field pore enlargement modality might further reduce the cell viability.

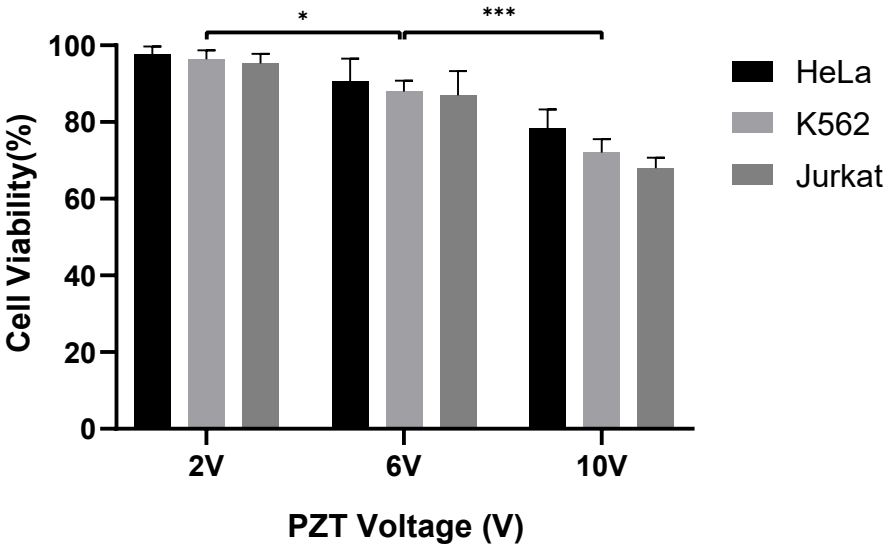

Figure 2.3 Effect of mechanical shear applied by LCATs on cell viability
Measured cell viability for HeLa, K562, and Jurkat cells treated with "low shear (LS)" (PZT voltage = 2V, SLS = 4.3 Pa), "moderate shear (MS)" (PZT voltage = 6V, SMS = 69.4 Pa), and "high shear (HS)" (PZT voltage = 10V, SHS = 272.9 Pa). *P<0.05, **P<0.01, ***P<0.001, and ****P<0.0001 were determined by Tukey's honest significant difference criterion.

Within each acoustic microstreaming vortices, although all trapped cells experience approximately equal maximum mechanical shear near oscillating air-liquid interfaces, the cells that follow larger orbits experience lower time-averaged shear than those following the inner orbits, which results in non-uniform shearing of cells. In addition, if not controlled, some cells can escape from one vortex to another while other cells (especially those with smaller circular paths) will be trapped in one location for the entire duration of treatment. This can also potentially contribute to inhomogeneous shear. To improve the performance of AESOP by enabling more uniform shearing of cells, PZT was turned OFF periodically (every 30 seconds) throughout device operation to mix and redistribute cells into different orbiting streamlines.

Uniform electric field enlargement of shear-induced pores for cargo delivery

Once nanopores on cells' membrane are initiated by acoustic microstreaming vortices, AESOP enlarges the pores by applying a sinusoidal AC electric field via interdigitated array (IDA) electrodes. For each different cell type, electric field voltage, frequency, and applied time were optimized (Supplementary Note 2 and Fig. S7 to S9, Supporting Information). Specifically, we found 12.5 V_{max} ($|E|_{RMS}$=0.4 $kV.cm^{-1}$), 10 kHz, and 10 ms for HeLa cells, 35 V_{max} ($|E|_{RMS}$=0.99 $kV.cm^{-1}$), 30 kHz, and 10 ms for K562 cells, and 25 V_{max} ($|E|_{RMS}$=0.85 $kV.cm^{-1}$), 20 kHz, and 10 ms for Jurkat cells, as the optimum electric field parameters. Numerical modelling was used to calculate the applied field strengths (|E|) corresponding to each different electric field voltages (Supplementary Note 3 and Fig. S10 to S12, Supporting Information). We, then, tested the performance of AESOP in delivery of dextran with molecular sizes ranging from 3 kDa to 2 MDa (Fig. 2.4A). According to the results, for all three different cell lines tested, >90% delivery efficiency was achieved for any given molecular size of dextran.

In the next step, to evaluate the role of shear in AESOP performance, we fixed the optimum applied electric field parameters for each cell type and compared AESOP with: 1) Flow-through: with LCAT off, the cells were flown through the chip and on top of the electrodes using a syringe pump, 2) Static: with LCAT off, the cells were loaded into the chip and settled down on top of the electrodes, and 3) LCAT Only: with LCAT on and electrodes off, the cells were loaded into the chip to be trapped in acoustic microstreaming vortices and experience mechanical shear with no electric field. Based on the results (Fig. 2.4C), compared to AESOP, flow-through and static groups that use only electric field (LCAT off) are inefficient at intracellular delivery of large molecules in the absent of mechanical shearing.

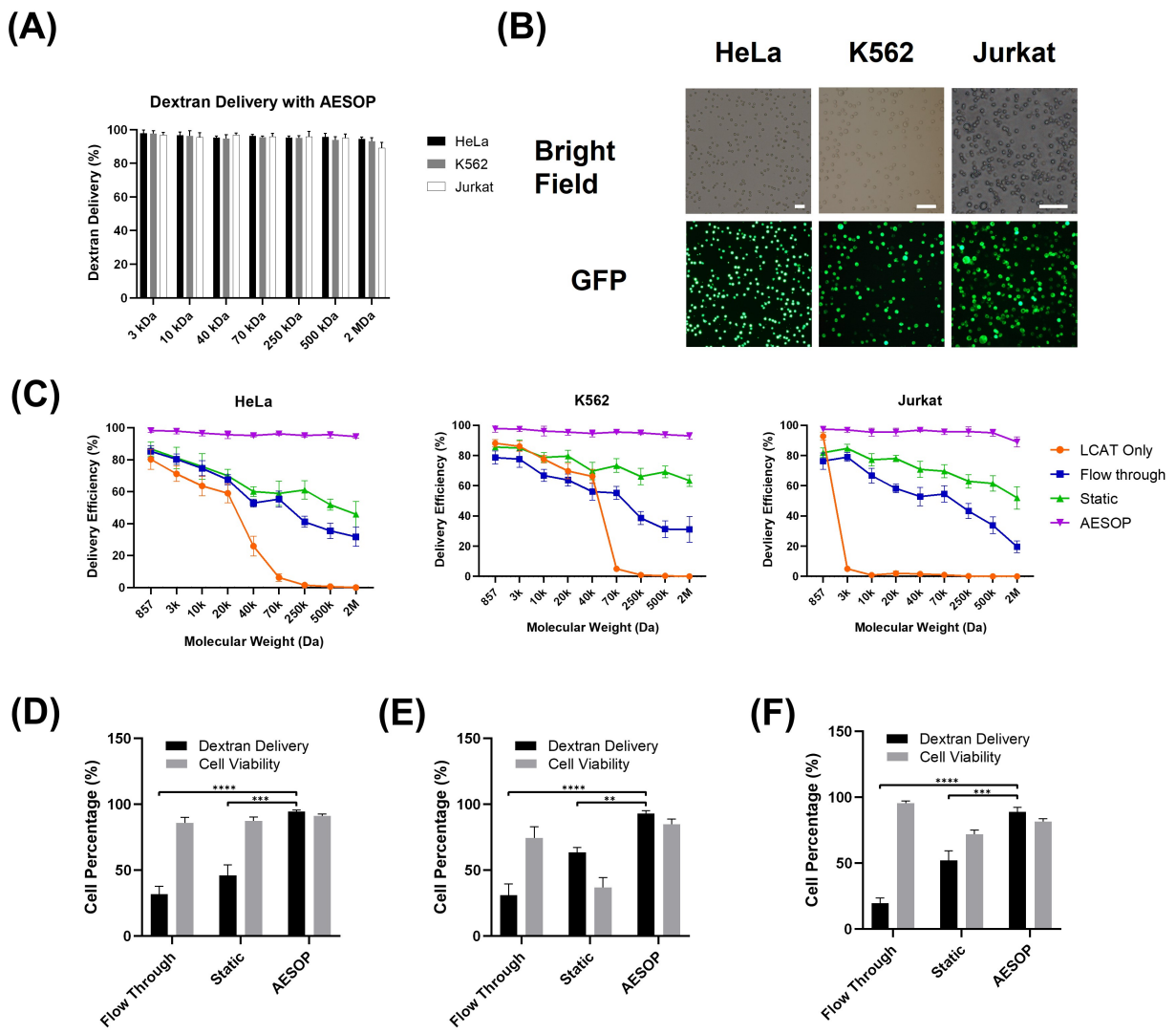

Figure 2.4 AESOP for intracellular delivery of different sizes of cargo
(**A**) Performance of AESOP in delivery of dextran, with wide range of molecular size, into HeLa, K562, and Jurkat cell lines, (**B**) Brightfield and GFP image of HeLa, K562, and Jurkat cells tested for delivery of 2 MDa dextran with AESOP platform, (**C**) Comparison of the performance of the AESOP with "Flow Through", "Static", and "LCAT only" in delivery of wide range of molecular sizes (EthD-1 dye (~857 Da) or fluorescein isothiocyanate–dextran with different sizes, ranging from 3 kDa to 2 MDa), (**D-E**) Comparison of the performance of the AESOP with "Flow Through" and "Static" in delivery of 2 MDa dextran and corresponding cell viability for (**D**) HeLa, (**E**) K562, and (**F**) Jurkat; the results indicate that AESOP offers significantly higher delivery efficiency compared to the "Flow through" and "Static" groups. Quantitative data were presented as mean ± standard error (SE). For all experiments, sample size n=3. *P<0.05, **P<0.01, ***P<0.001, and ****P<0.0001 were determined by Tukey's honest significant difference criterion. The scale bars in **(B)** are 100 μm.

Specifically, the results for delivery of 2 MDa dextran (Fig. 2.4D-F) indicate that AESOP achieves significantly higher delivery efficiency (>90%) compared to flow-through (low,

<30%) and static (moderate, <60%). The moderate delivery efficiency of static approach is because the cells are close to or in contact with the electrodes and, thus, experience high electric field strengths (Supplementary Note 3 and Fig. S12, Supporting Information). Like bulk electroporation, the exposure to high electric field in static approach is particularly unfavorable for applications that long-term cell viability is critical after the delivery process (e.g. plasmid and mRNA delivery).

Dosage-controlled capability and mechanism of intracellular delivery

In AESOP platform, acoustic microstreaming vortices play a key role in efficient and precise intracellular delivery of cargos. The cells in these vortices are not only exposed to uniform mechanical shear and electric field, but also uniformly mixed with exogenous cargos by chaotic mixing. Thus, we hypothesized that the imposed uniformity in membrane disruption and cellular uptake would result in dosage-controlled intracellular delivery across cell population. To test this hypothesis, we delivered YOYO-1 labeled plasmid DNA (6.1 kbp) into K562 cells using AESOP and two other control groups (static and flow through). Since the amount of plasmid DNA delivered to a cell is directly proportional to the measured fluorescent intensity of YOYO-1 dye within the cell, fluorescent intensity distribution among cell population was analyzed by flow cytometry. According to the histogram of fluorescent intensity (Fig. 2.5A), AESOP offers a narrow peak distribution of YOYO-1 labeled DNA, indicating delivery of uniform doses across the cell population. In contrast, for the two control groups, where the effect of vortices was eliminated by turning LCAT off, the intensity peak distribution of delivered DNA is wide and not uniform among population of cells.

To better quantify controllable intracellular delivery, we calculated the percentage coefficient of variation (%CV, defined as the percentage ratio of standard deviation to the

mean) of fluorescent intensity across cell populations processed by the control groups and AESOP with DNA concentrations of 50 ng, 500 ng, 1 μg, and 2.5 μg per million cells (Fig. 2.5B). Unlike the two control groups with %CV>120, all AESOP groups offer %CV around 50%. We also compared the performance of AESOP with a commercial electroporation system (Lonza Nucleofector™). According to the results (Fig. S13, Supporting Information), AESOP reduces the %CV by half compared to the Lonza Nucleofector™. The low %CV achieved by AESOP groups not only confirms delivery of uniform doses across the cell population, but also is an indicator of performance consistency when working with different cargo concentrations.

In addition, for each different DNA concentrations, we calculated the mean fluorescent intensity of YOYO-1 dye delivered to the cells (Fig. 2.5C). Based on the results, the average dose delivered to the cells is linearly proportional to DNA concentration, indicating that AESOP offers controllable intracellular delivery. We also evaluated how cargo size would affect uniformity of intracellular delivery across cell population. For this purpose, we calculated the %CV for intracellular delivery of 3.5 kbp, 6.1 kbp, and 9.3 kbp plasmids. The results (Fig. S14, Supporting Information) show that AESOP offers low and consistent %CV of intracellular delivery regardless of cargo size.

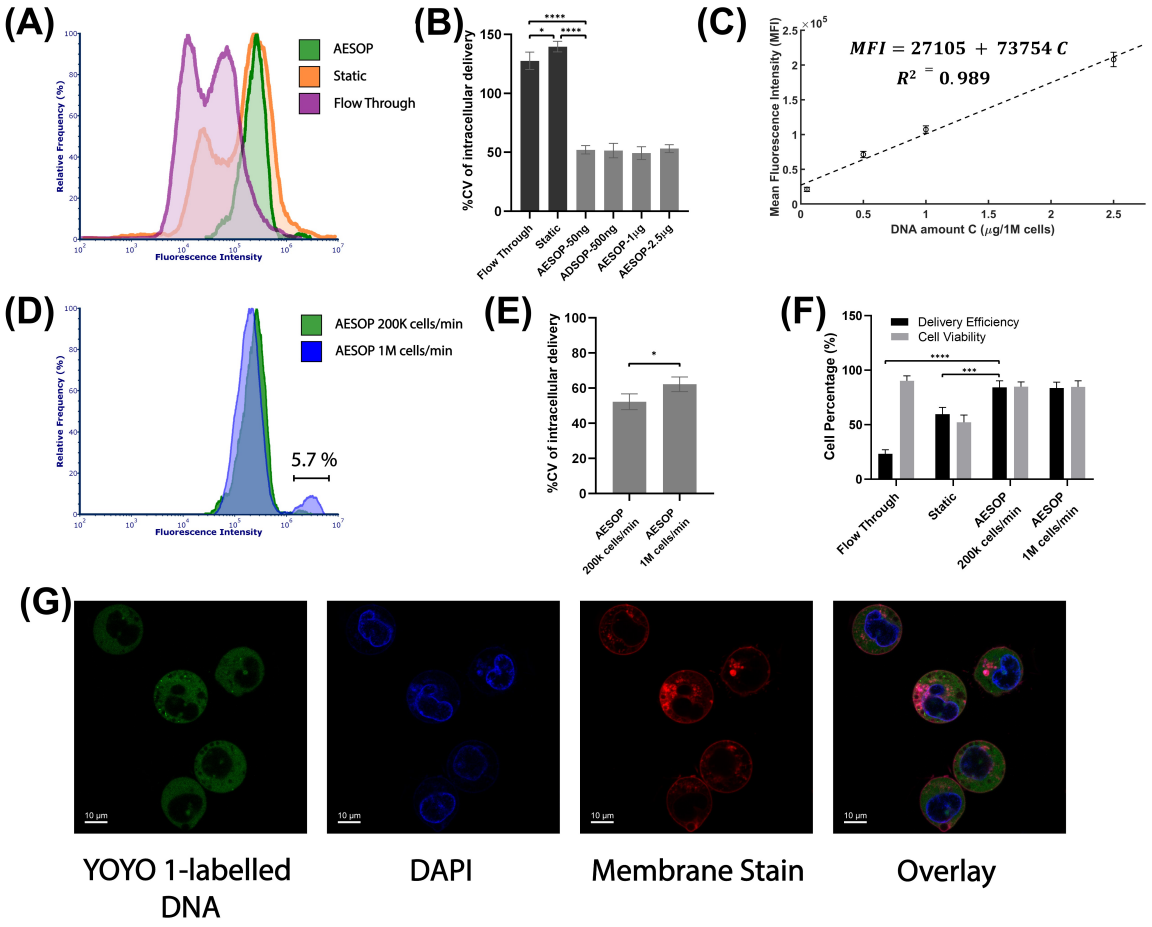

Figure 2.5 Intracellular delivery of fluorescent labeled plasmid DNA
(**A**) Histogram of fluorescent intensity of YOYO-1 labeled plasmid DNA delivered into K562 cells. For better comparison, the histograms were normalized by relative frequency (%). Compared to control groups, AESOP offers a sharp and narrow intensity distribution, indicating AESOP's capability for precise and controlled delivery, (**B**) %CV of intracellular delivery for control groups (flow through and static) and AESOP operated with different DNA concentration, (**C**) Mean fluorescent intensity of YOYO-1 dye delivered to the cells by AESOP operated with different DNA concentrations. A linear model is fitted to the obtained data, indicating controlled delivery by AESOP, (**D**) The histogram of fluorescent intensity of YOYO-1 labeled plasmid DNA delivered into K562 cells using moderate and high throughput AESOP platforms, (**E**) %CV of intracellular delivery for moderate and high-throughput AESOP versions; increasing the throughput resulted in slight increase in delivery distribution across cell population, (**F**) The Delivery efficiency and cell viability for intracellular delivery of labeled DNA into cells; the results show that >80% plasmid DNA delivery efficiency can be achieved using AESOP platform, and (**G**) Confocal microscopy image of cells after intracellular delivery experiment with AESOP; for this experiment, the cells' nucleus and membrane were stained with DAPI and deep red CellMask™ plasma membrane stains. Based on the results, acoustic microstreaming vortices directly deliver the plasmid DNA to the cell cytoplasm. Quantitative data were presented as mean ± standard error (SE). For all experiments, sample size n=3. *P<0.05, **P<0.01, ***P<0.001, and ****P<0.0001 were determined by One-way ANOVA with Tukey's honest significant difference criterion for (B) and (F), and student t-test for (E).

In the next step, we investigated whether high-throughput cell processing affects the performance of AESOP for gene delivery. For this, two different AESOP designs were tested with the same DNA concentration: 1) moderate throughput: capable of processing up to 200K cells/min (Fig. 2.1B, C), and 2) high throughput: capable of processing up to 1M cells/min (Fig. S15 and Movie 2.4, Supporting Information). Based on the results (Fig. 2.5D, E), except overdose delivery into a small percentage (~5%) of cells in the high-throughput version, there is no significant difference in delivery efficiency and uniformity between the two versions. This indicates that scalability of the platform is straightforward and does not significantly affect system performance. Figure 2.5F shows the corresponding efficiency and cell viability for delivery of labeled plasmid into cells. Similar to the trend observed in intracellular delivery of 2 MDa dextran, the results indicate that both moderate and high-throughput AESOP versions achieve high delivery efficiency of plasmid (>80%) while static and flow through result in <60% and <30% efficiency, respectively.

In the next step, we evaluated how AESOP facilitated intracellular delivery of plasmid DNA into cells. The main question was whether LCAT entangles the plasmid DNA to the cell membrane,[91] or it delivers directly to either the cytoplasm or nucleus.[24, 92] For this purpose, cell nuclei and membranes were labeled with DAPI and CellMask™ plasma membrane stains, respectively. After the experiment, confocal microscopy was performed to observe the distribution of labeled plasmid DNA in K562 cells. Based on the results (Fig. 2.5G), the plasmid DNA are mostly delivered into the cells' cytoplasm. Since AESOP utilizes AC electric field with frequencies ≥10kHz, the effect DNA electrophoresis can be neglected. This indicates that the chaotic mixing induced by microstreaming vortices acts as the major active force to guide the plasmid DNA through the cell membrane, and into the cytoplasm. As a

result, LCAT eliminates the need for any other active force, such as electrophoresis, to guide DNA into the cells.

Gene delivery analysis: eGFP plasmid DNA transfection & CRISPR-Cas9 gene editing

We also explored the performance of AESOP for intracellular gene delivery applications in protein expression and targeted gene knockout. First, we transfected HeLa, Jurkat, and K562 cells with a ~3.5 kbp GFP-expressing plasmid (pmaxGFP™). The protein expression levels were analyzed by flow cytometry 48 hours after the gene delivery experiment. Based on the results (Fig. 2.6A; Fig. S16, Supporting Information), high GFP protein expression efficiencies of >90%, >60%, and >70% were obtained for HeLa, Jurkat, and K562 cells, respectively, with cell viability of >80% for all the three cell types tested. In the next step, a relatively large eGFP-expressing plasmid DNA (6.1 kbp) was chosen and delivered into cells using the AESOP platform. For this large eGFP plasmid, we could achieve >80%, >40%, and >50% transfection efficiencies for HeLa, Jurkat, and K562, respectively, while still maintaining cell viability to be >80% (Fig. 2.6B, C). To rule out the possibility that AESOP is only an electroporator coupled with mixing provided by acoustic microstreaming vortices, we performed K562 cell transfection with 6.1 kbp eGFP plasmid using "Static" approach (loading the cells on top of electrodes and applying the same optimized E parameters) followed by immediately turning on acoustic microstreaming vortices to perform mixing. According to the results (Fig. S17), without shear-induced initiation of nanopores before applying electric field, very low transfection efficiency (~5%) was achieved.

We then evaluated AESOP for CRISPR-Cas9 gene editing applications. For this purpose, a 9.3 kbp plasmid DNA encoding Cas9 protein and sgRNA targeting PTEN gene knockout were chosen and delivered into K562 cells. Based on the flow cytometry analysis of cells treated

with AESOP, CRISPR-plasmid intracellular delivery efficiencies of >80% were achieved for K562 cells (Fig. 2.6D). After gene delivery, the cells were cultured for 48 hours, selected with eGFP marker (up to 20% of cell population were eGFP positive with >80% viability), cultured for an additional 7 days, and analyzed by immunofluorescence (IF) staining. Compared to the control group, where PTEN proteins were detected in the cytoplasm, the experimental group showed clear knockout of the gene (Fig. 2.6E). Thus, based on the eGFP marker, we estimate up to 20% gene knockout via AESOP platform, which requires future confirmation by comprehensive DNA sequencing analysis. No significant changes were observed in cell viability for 48 hours and 7 days culture.

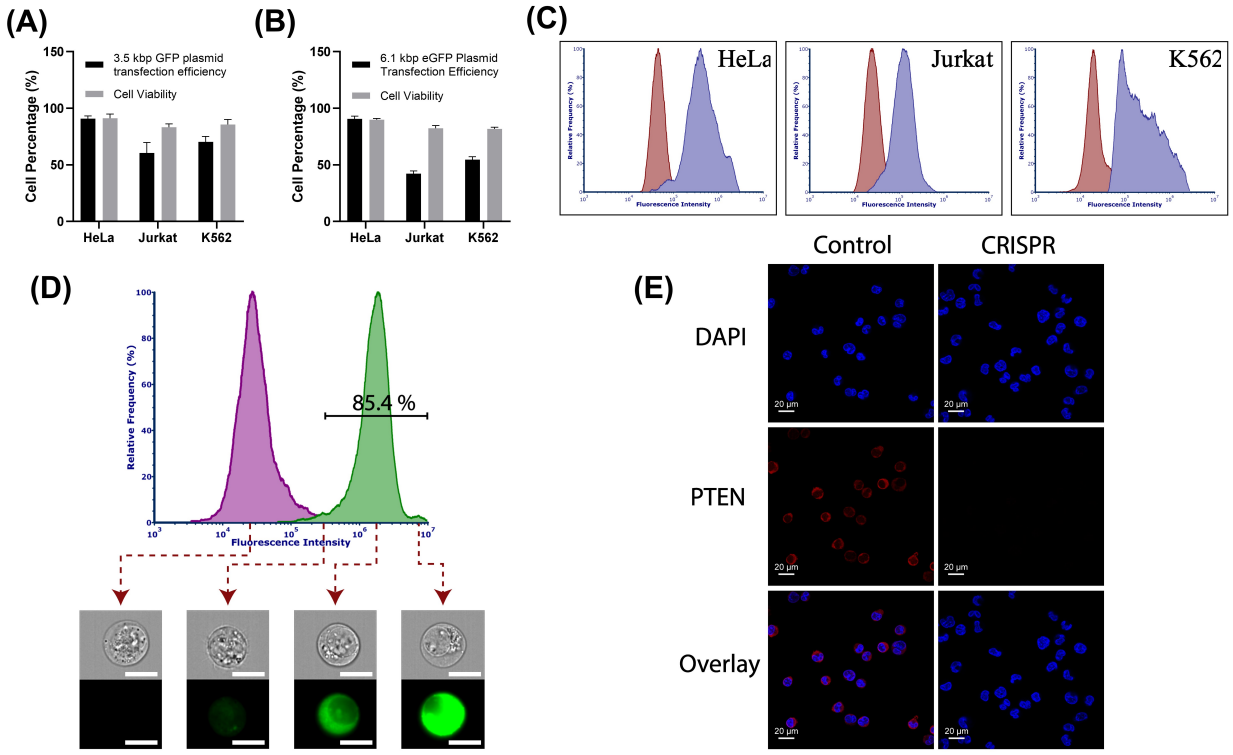

Figure 2.6 Gene delivery analysis
(**A**) Transfection efficiencies and cell viability 48 hrs after delivery of 3.5 kbp GFP-expressing plasmid DNA; AESOP achieved >90%, >60%, and >70% transfection efficiencies with >80% high cell viabilities, (**B**) Transfection efficiencies and cell viability 48 hours after delivery of 6.1 kbp eGFP-expressing plasmid DNA; AESOP achieved >80%, >40%, and >50% transfection efficiencies with >80% high cell viabilities, (**C**) Flow cytometry quantification of eGFP expression for experimental (blue) and control (red) groups. The cells in control group were incubated for 48 hours with plasmid

DNA, (**D**) Flow cytometry quantification of delivery of YOYO-1 labelled plasmid DNA encoding Cas9 protein and PTEN sgRNA into K562 cells for experimental (green) and control (purple) groups. Plasmid DNA was mixed with the cell sample in the control group. For better comparison, the histograms were normalized by relative frequency (%), (**E**) immunofluorescence (IF) staining of K562 cells with PTEN monoclonal antibody recognized by Alexa Fluor 647 secondary antibody. DAPI was used to stain the nucleus. The scale bars in (D) are 10 μm.

As a proof-of-concept, we also tested AESOP for transfection of human primary T cells. Based on our preliminary results, we could achieve up to 30% GFP protein expression efficiency and >80% cell viability (Fig. 2.7, Supporting Information). To further enhance AESOP performance in engineering primary T cells, the next stage of our research involves a more in-depth optimization of mechanical shear and electric field parameters.

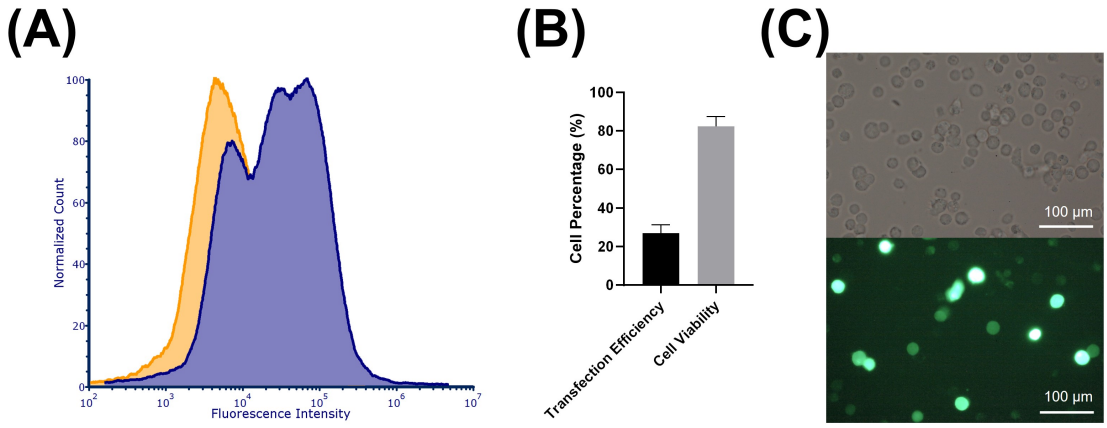

Figure 2.7 AESOP for transfection of human primary T cells
(A) Flow cytometry quantification of eGFP expression in primary T cells for experimental (blue) and control (yellow) groups. In experimental group, the cells were transfected by pmaxGFP™ plasmid, **(B)** T cell transfection efficiency and cell viability 48 hours after delivery, and **(C)** Brightfield and GFP image of T cells transfected using AESOP device

Discussion

AESOP is a multimodal non-viral intracellular delivery platform that addresses some of the challenges facing viral and conventional non-viral techniques (Table 2.1). Furthermore, for adoption in gene/cell-based therapies, biomanufacturing, and basic research, AESOP offers: i) High delivery efficiency while maintaining cell viability, ii) Dosage-controlled delivery of

cargos, iii) High throughput, iv) Compatibility with both adherent and suspension cell types, and v) Simplicity in fabrication and operational protocol. For this, AESOP controls cell membrane permeabilization and cellular uptake in an efficient, precise, and high-throughput manner.

	Viral Transduction	**Electroporation**	**Lipofection**	**AESOP**
Risk of Cytotoxicity	High	Low	High	Low
Risk of Immunogenicity	High	Low	Moderate	Low
Transfection efficiency	High	Depends on cell type	Depends on cell type (low for suspension cells)	Depends on cell type
Cell viability	High	Low	Depends on cell type	High
Cost	High	Moderate	Low	Low
Throughput	High	High	High	Moderate
Cargo size limitation	Yes	No	No	No
Dosage-controlled delivery	N/A	Low	Low	High

Table 2.1 Comparison of AESOP with viral and conventional non-viral intracellular delivery techniques

To permeabilize cell membranes effectively and gently, AESOP adopts a two-step membrane disruption strategy that uniquely combine two robust and well-known cell-membrane

mechanical-disruption approaches: mechanical shear and electroporation.[19, 93, 94] First, it forms nanopores on the cell membrane using mechanical shear. Second, it enlarges these nanopores upon the cells' uniform exposure to gentle electric fields. Stable bubble oscillations have been known to apply local shear force and permeabilize nearby cells by inducing localized deformation on plasma membrane.[95-99] Similar to this principle, AESOP employs LCAT's acoustic microstreaming vortices to apply tuned and moderate mechanical shear on cells near oscillating air-liquid interfaces and, consequently, creates nanopores on their membrane. For this case, as pore resealing occurs in the order of milliseconds to seconds,[96, 100, 101] detection of pores by techniques such as scanning electron microscopy (SEM)[102] or atomic force microscopy (AFM)[103] imaging is challenging due to long preparation time required. Thus, in this study, we relied on intracellular uptake of different sizes of molecules to confirm formation of pores and estimate their sizes. One of our important findings indicates that shear-induced cell membrane poration is cell type dependent. This can be explained by the fact that each cell type has different mechanical properties (e.g., cell membrane stiffness and cytoskeleton arrangement) and, consequently, experiences different shear-induced localized membrane deformation near the oscillating air-liquid interfaces.[98, 104] To open larger pores, AESOP needs only gentle and low-strength, rather than undesirable high-strength, electric fields. We hypothesize that by shear-induced transient formation of nanopores, AESOP does not need to apply a high electric field to overcome large transmembrane threshold potential to create hydrophobic pores (HFBPs). Instead, we speculate that only a low electric field is required to expand the pre-existing HFBPs to lower-energy hydrophilic pores (HFLPs) without creating new pores.[105] This strategy is indeed similar to dual-pulse electroporation strategy where the cells experience

a short, high-strength pulse followed by a long, low-strength pulse. The former creates several nanopores on cell membrane, and the latter expands the pores and electrophoretically guides the charged cargos into the cell.[106, 107] This strategy has shown to improve delivery efficiency and cell viability.[19] AESOP outperforms dual-pulse electroporation technique because it does not rely on high-strength pulse to initiate the creation of nanopores. As a result, it overcomes fundamental challenges of using high-strength electric fields in electroporation such as joule heating, metal contamination, electrolysis, and pH change in buffer. In addition, since cells are tumbling in acoustic microstreaming vortices, they are uniformly exposed to both mechanical shear and electric field, resulting in uniform membrane permeabilization across cell population.

In terms of cellular uptake, AESOP uses chaotic mixing, induced by acoustic microstreaming vortices, to deliver cargos efficiently and uniformly into cells. The majority of intracellular delivery approaches rely on either passive diffusion or electrophoresis to guide the cargos into cells. Compared to passive diffusion, electrophoresis significantly improves intracellular delivery of cargos into permeabilized cells. Recently, micro-vortices have also shown to enhance cellular uptake by mixing cells with the exogenous cargos.[30, 31, 33] In our previous work, we developed a droplet microfluidic platform for lipid-mediated single-cell transfection. We showed that chaotic advection, formed inside droplets moving in a winding channel, can significantly enhance cell transfection efficiency and uniformity.[31] Here, in AESOP, we took a new approach for high-throughput and efficient mixing, and designed hundreds of whirlpool-like microstreaming vortices to simultaneously mix hundreds of thousands of permeabilized cells with exogenous cargos. Our presented results indicate the important role of these vortices to increase cellular uptake efficiency.

As a result of uniform membrane permeabilization and cellular uptake, AESOP offers dosage-controlled delivery capability. This is an important requirement for many cell engineering applications. For example, Mali et al. showed that precise control over Cas9-sgRNA dose is critical for achieving desired targeting specificity in Cas9 gene editing.[108] In this paper, we evaluated dosage-controlled intracellular delivery by flow cytometry analysis of the cells processed by AESOP. We used %CV as an indicator of relative dispersion of the amount of DNA delivered to the cell population and showed that %CV<60 can be achieved by AESOP. In the next step, AESOP performance was evaluated at different DNA concentrations. We found out that: (i) %CV is independent of the cargo concentration and size, showing the performance consistency, and (ii) the average dose delivered to individual cells is linearly proportional to the cargo concentration. Utilizing this precise intracellular delivery approach, we could lower the cargo concentration, down to 1 μg of plasmid per million cells. This is particularly important for reducing the cost and minimizing toxicity associated with plasmids.[109] Overall, several promising micro- and nanotechnology approaches have been developed for dosage-controlled intracellular delivery such as nanostraw-electroporation,[18] nanofountain probe electroporation,[34] nanochannel electroporation,[35] micro/nano-injection,[36, 37] cell-induced acoustic microstreaming,[110] and microscale symmetrical electroporator arrays.[33] Compared to these methods, AESOP is an order of magnitude higher in throughput and compatible with both suspension and adherent cells, as cells are suspended in acoustic microstreaming vortices. Building on this foundation, future research will be focused on further enhancing the uniformity of membrane permeabilization and cellular uptake. In our current AESOP version, it is reasonable to assume that the streaming flow has a 2D profile.[111] As a result, cells orbiting in different orbits will experience different

time-averaged mechanical shear. To circumvent this, here we periodically turned off the LCAT (needs to be further optimized) to redistribute cells into different orbits and achieve uniform time-averaged mechanical shearing. As an alternative strategy, in effective 3-D vortices, not only better mixing can be achieved, but also the cells' shearing is more uniform due to the widening and tightening of the orbits along the height of the microchannel. In future experiments, we will explore the effects of channel dimensions (especially the height), oscillation mode, amplitude, and frequency of air-liquid interface, and cells' size on enhancing the 3-D streaming.[111]

	Throughput	**Compatibility with cell type**
Nanostraw-electroporation[18]	100,000 cells per chip	Requires cell adhesion to the substrate (suitable for adherent cells)
Nanofountain probe electroporation[34]	"Not Reported", Intrinsically Low	Suitable for adherent cells
Nanochannel electroporation[35]	Reported: up to 1000 cells per chip, Scalable to up to 100,000 cells per chip	Compatible with both adherent and suspension cells
Micro/nano-injection[36, 37]	<100 cells per hour	Mostly suitable for adherent cells
Cell-induced acoustic microstreaming[110]	Reported: ~100 per experiment, Scalable to up to tens of thousands of adhered cells per treatment	Requires cell adhesion to the substrate (suitable for adherent cells)
AESOP	1,000,000 cells/min per single chip	Compatible with both adherent and suspension cells

Table 2.2 Comparison of AESOP with state-of-the-art micro- and nanotechnology approaches for dosage-controlled intracellular delivery

In recent years, there has also been growing need for intracellular delivery of large cargos for gene editing. For example, most plasmid-based CRISPR-Cas9 gene editing cargos are >9 kbp. Another powerful recent development is base editing, which uses a cytosine base editor (CBE) or an adenine base editor (ABE) with a guide RNA and, as a result, requires delivery of complexes with an approximate size of 6 kbp.[112] For these applications, the use of viral vectors is challenging due to their limited packaging capacity. For example, AAVs, as popular vectors for gene/cell-based therapies, have a packaging capacity of 4.7 kbp and, thus, dual or triple AAV delivery approaches are required for cargos that exceed such a limit.[112, 113] Recently, methods based on membrane deformation,[21] bubble cavitation,[38, 39] nanochannel electroporation,[25] and high-frequency ultrasound[40] have demonstrated successful delivery of large cargos (>6 kbp). Despite encouraging results, compared to AESOP, these methods are lower in throughput and/or require cell interaction with a substrate that limits their application mostly to adherent cells. Our presented results with 6.1 kbp eGFP plasmid and 9.3 kbp CRISPR-Cas9 plasmid show that AESOP also addresses two other key challenges associated with delivery of large cargos: low delivery efficiency and cell viability. Overall, it is more challenging to deliver larger cargos, as diffusion-limited intracellular delivery becomes extremely inefficient. One solution is to increase the cargo concentration to achieve acceptable transfection efficiency. Thus, for large cargos, not only are larger pores needed, high concentration of cargos greatly reduces the cells' viability, in particular for plasmid-based gene editing applications as there exists specific toxicity associated with large plasmids.[109] The chaotic advection provided by AESOP not only increases transport of larger cargo molecules to overcome their lower diffusion rates, but it also reduces the required concentration of cargos to minimize overdose delivery across cell populations.

	Throughput	Compatibility with cell type
Membrane deformation[21]	"Not reported", Moderate, Prone to clogging at high throughputs	Compatible with both adherent and suspension cells
Bubble cavitation[38, 39]	Up to 100,000 cells/min per single chip	Mostly suitable for adherent cells
Nanochannel electroporation[25]	Reported: Up to 40,000 per cm^2, Scalable to up to million per silicon wafer	Mostly suitable for adherent cells
High-frequency ultrasound[40]	50,000–100,000 per chip	Mostly suitable for adherent cells
AESOP	1,000,000 cells/min per single chip	Compatible with both adherent and suspension cells

Table 2.3 Comparison of AESOP with state-of-the-art micro- and nanotechnology approaches for intracellular delivery of large cargos

For adoption in clinical settings, intracellular delivery platforms should also satisfy the requirement for high-throughput cell processing. As an example, Tisagenlecleucel (Kymriah), the anti-CD19 chimeric antigen receptor (CAR) T-cell therapy for pediatric patients with B-cell precursor acute lymphoblastic leukemia (ALL), requires an average dose of 1×10^8 transduced viable T cells.[114] Our current 2 cm × 5 cm high-throughput AESOP chip can already process up to 1 million cells/min (<1 hour for processing 1×10^8 cells). It should be noted that several promising microfluidic platforms can process cells with the same throughput or higher.[115-117] However, compared to these methods, AESOP's presented capabilities in uniform and dosage-controlled intracellular delivery of cargos at such level of throughputs make it an attractive candidate to be used in clinical settings. In this work, by

comparing moderate (200k cells/min/chip) and high-throughput (1M cells/min/chip) AESOP versions, we demonstrated the scalability of our platform without sacrificing the delivery efficiency and precision across cell populations. This is mainly because AESOP consists of hundreds of microvortices, each holding thousands of cells, that act as independent reactors. With flow control and optimization, our next step will be focused on achieving 10 million cells/min (<10 minutes for processing 1×10^8 cells). This would require optimization of the microfluidic channels and LCATs to maximize cell processing density and speed. Increasing the channel dimensions (length, width, height) is the most direct way to increase throughput. However, this may require an increase in PZT applied voltage or duration of operation. As a result, careful attention should be paid to PZT-induced local heating and bubble stability over duration of operation. In this work, under optimum operational parameters (PZT voltage = 6V, applied time = 5 minutes), we did not observe significant PZT-induced local heating or instability in the air-liquid interfaces (Supplementary Note 4 and Fig. S18 and S19, Supporting Information). As an alternative strategy to increase system throughput, parallelization of multiple chips (stacking) would be also adopted. One of the intrinsic advantages of the AESOP technology is that the whole system is compact with pumping, trapping, shearing, and interdigitated electrodes, all on one common microfluidic chip platform. Consequently, the whole system is simple, easy to operate, test, and characterize.

CHAPTER 3: SHEAR-DEPENDENT MICRO-VORTICES IN LIQUID-LIQUID FLOW FOCUSING GEOMETRY: A THEORETICAL, NUMERICAL, AND EXPERIMENTAL STUDY

Introduction

In 2017, our lab reported a micro-vortex based technique that can trap and release cells/particles into droplets based on their sizes.[118] In this method, an 'expansion' flow focusing design is used for droplet generation.[119] By applying high shear stress on the interface of the continuous/dispersed phases near the narrow orifice, we could demonstrate the formation of two symmetric three-dimensional micro-vortices in the dispersed phase. These micro-vortices were then used for trapping cells, enrich their concentration locally, and then release them one-to-one (1-1) into droplets at >50% encapsulation efficiency, which is at least 10 times greater efficiency than random encapsulations at low sample concentration.

To improve the effectiveness and robustness of this method, here we utilize experimental, theoretical, and computational fluid dynamics to focus our discussion on understanding the physics of such micro-vortices and their key control parameters. Using experimental fluid mechanics, we study the mechanism for generating micro-vortices and quantitatively evaluate the micro-vortices trapping size threshold (d_{gap}) for selective trap & release of particles. In addition, we present a theoretical model to predict parameters affecting the micro-vortices trapping size threshold (d_{gap}) and validate it with experimental results. Since the inherent three-dimensional nature of these complex vortices makes it challenging to only

rely on experimental and theoretical fluid mechanics for such studies, a 3D computational fluid dynamics (CFD) model using volume of fraction (VOF) multiphase algorithm is then developed to capture the three-dimensional nature of such vortex streamlines. Utilizing the developed CFD model, we study the effect of various parameters (e.g., channel geometry, capillary number (Ca), and contact angle) on the micro-vortices. The present theoretical and CFD study supported by experimental results provide detailed understanding of shear dependent micro-vortices in liquid-liquid flow focusing designs, which can be used for developing more efficient 1-1 droplet encapsulation methods.

Theoretical model

Figure 3.1A shows the schematic of the device illustrating the fluidic circuits for both continuous (oil) and dispersed (aqueous) phases, and the micro-vortex streamlines generated in the dispersed phase. The continuous phase enters the junction through the side channels and exit through the narrow orifice, shearing the dispersed phase. The occurrence of the micro-vortices (in the aqueous phase) depends on the combined effect of aqueous-oil interfacial shearing rate (α) and the tip oscillation frequency (TOF), defined as the interfacial oscillation frequency of the droplet generation tip. The protrusion and retraction (from P1 to P2 position) of the droplet generation tip occurs each time a droplet is generated (Fig. 3.1C); therefore, the tip oscillation frequency (TOF) is equal to the number of droplets generated per second (f).

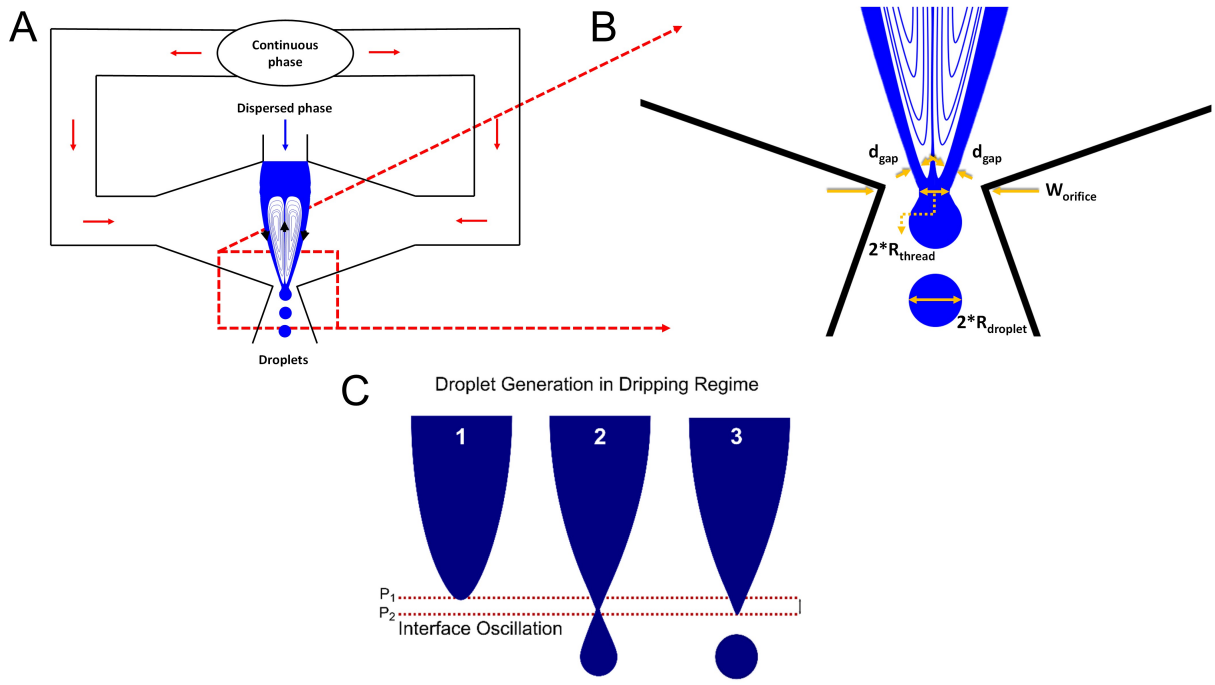

Figure 3.1 Schematic illustration of shear-dependent micro-vortices in the liquid-liquid flow-focusing geometry
(A) Schematic of the fluidic circuit and the flow-focusing junction along with the micro-vortices generated in the dispersed phase; d_{gap} is shaded in blue **(B)** Zoomed in schematic of the droplet generation junction illustrating the relevant parameters **(C)** Schematic illustration of the tip oscillation during the droplet formation. The dispersed phase tip oscillates between P1 and P2 each time when a droplet is generated—an important parameter for the generation of the micro-vortices

Both the parameters α and TOF vary with droplet generation regime and are affected by viscosity and flow rate ratio of dispersed to continuous phase, interfacial tension, and channel geometry (e.g., orifice width, channel height, etc.). Specifically, α and TOF are smallest in the squeezing regime and highest in the jetting regime, which is dictated by the capillary number ($Ca = \frac{\mu_c V_c}{\gamma}$), where μ_c is the viscosity of the continuous phase, V_c is the velocity of the continuous phase and γ is the interfacial tension between the phases.[120] In our previous work, we observed that micro-vortices start to occur at higher values of α and TOF.[118] In the squeezing regime, which occurs at lower Ca, both the interfacial shearing rate (α) and the TOF (<100 Hz) are not large enough to generate the micro-vortices. However, at

a higher Ca (where the regime switches from squeezing to dripping), the micro-vortices are likely to occur because of the increase in α and TOF (>2000 Hz). Dynamics of the vortex streamlines in dripping and jetting is nearly same, therefore we focus our discussion on the squeezing and dripping regimes.

In dripping regime, the micro-vortices can be formed by tuning α and TOF. Once they are formed, the dispersed phase enters the control volume through the center channel inlet, recirculates within the vortex, and exits through the d_{gap} out of the orifice as droplets (Fig. 3.1A), where d_{gap} is the width that separates the closed vortex streamline from the interface (Fig. 3.1B)[121, 122]. The rapid pulsing of aqueous interface during the droplet formation is analogous to the air-aqueous interface vibration in the microstreaming flows. The recirculation vortices are directed such that they are forward-oriented at the interface and reverse-oriented at the center.

The expression for d_{gap} can be derived with the assumption that the d_{gap} is approximately equal to the radius of dispersed phase thread (R_{thread}) at the dripping regime (Fig. 3.1B).

$$d_{gap} \cong R_{thread} \tag{3.1}$$

This is a fair physics assumption since the micro-vortices end near the thread. Based on the theoretical work developed by Tomotika et al.,[123] R_{thread} can be related to the size of generated droplets ($R_{droplet}$) as

$$R_{thread} = \frac{1}{\left(\frac{1.5\pi}{X_m}\right)^{\frac{1}{3}}} R_{droplet} \tag{3.2}$$

where dimensionless parameter X_m is the dominant wave number. X_m can be expressed in terms of dominant wavelength λ_m, at which the maximum instability occurs at the thread

$$X_m = \frac{2\pi R_{thread}}{\lambda_m} \tag{3.3}$$

Based on equation (3.2) and from the tabulated values for X_m by Tomotika et al., for the viscosity ratio ($\frac{\mu_d}{\mu_c}$) of 0.025, used in this study, we have

$$R_{thread} = 0.3\ R_{droplet} \tag{3.4}$$

In flow focusing geometries, there exists a power-law relation between the dimensionless droplet size ($\frac{R_{droplet}}{W_{orifice}}$, where $W_{orifice}$ is the orifice width), and the flow rates of continuous and dispersed phases (Q_c and Q_d, respectively)

$$\frac{R_{droplet}}{W_{orifice}} \propto \left(\frac{Q_d}{Q_c}\right)^{\beta} \tag{3.5}$$

where β usually lies in the range of 0.25-0.35.[119, 124] For our specific microchannel geometry, β is equal to 0.3.[119] Using equations (3.1) and (3.4), this power-law relation can be rewritten as

$$d_{gap} = 0.3C_1.W_{orifice}.\left(\frac{Q_d}{Q_c}\right)^{0.3} \tag{3.6}$$

where the constant C_1 is dependent on microchannel geometry and can be derived empirically or numerically. Based on equation (3.6), if the flow rate of dispersed phase is fixed, d_{gap} has an inverse power-law correlation with the capillary number ($d_{gap} \propto \left(\frac{1}{Ca}\right)^{0.3}$) because the capillary number is directly related to the continuous phase flow velocity.

Numerical model

Transient modelling of droplet generation is performed using commercial CFD package ANSYS Fluent. The device 3D geometry was built in ANSYS Design Modeler and meshed in

ANSYS Meshing. The 3D mesh mainly consisted of hexahedron elements with quadrilateral 2D elements on surfaces. To accurately capture the droplet generation, the mesh is further refined near wall interfaces using the inflation meshing technique. The device geometry, meshing, and boundary conditions are shown in Fig. 3.2.

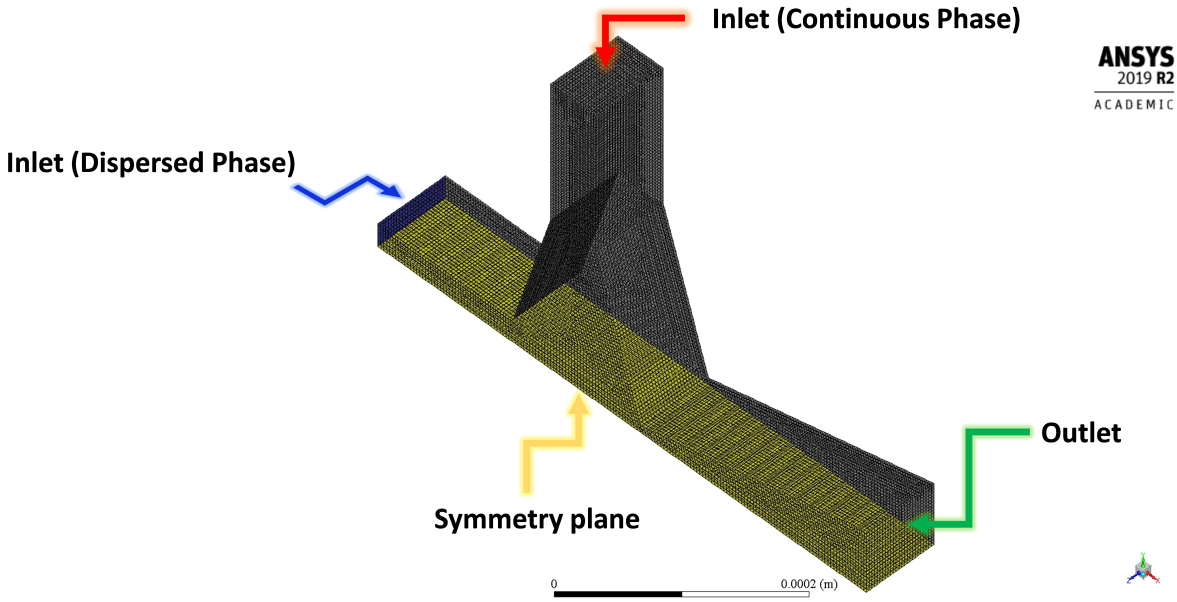

Figure 3.2 3D device geometry with the corresponding meshing performed in ANSYS Meshing and the boundary conditions
For reducing the cost of the calculations, the symmetry boundary condition is chosen. All other boundaries not specified here are walls.

The explicit coupled Level-Set and Volume of Fluid (VOF) model was employed to track the interface between the dispersed and continuous phases.[125, 126] Such a coupled method overcomes the deficiencies of level-set model in preserving volume conservation and VOF in calculation of spatial derivatives. The transient tracking of level-set function (ϕ) is similar to the VOF model and can be written as:

$$\frac{\partial \phi}{\partial t} + \nabla . (\vec{u}\phi) = 0 \qquad (3.7)$$

where $\vec{u}$ is the velocity field and the level set-function can be defined as the signed distance to the interface:

$$\phi(x,t) = \begin{cases} +|d| & if\ x \in the\ primary\ phase \\ 0 & if\ x \in\ \Gamma = \{x \mid \phi(x,t) = 0\} \\ -|d| & if\ x \in the\ secondary\ \ phase \end{cases} \tag{3.8}$$

where d is the distance from the interface. In this work, the primary and secondary phases are the continuous and dispersed phases, respectively. In modelling droplet generation phenomena, there exist significant deformation of interfaces and uneven thickness across them. Thus, large numerical errors can be produced in mass and momentum equations, as distant constraint ($|\nabla\phi| = 1$) cannot be maintained. To circumvent this, a level-set re-initialization process is adopted at each time step based on geometrical interface-front construction method.[127] In reconstruction of the interface, the VOF model provides information on locating interface fronting cells and level-set gradients determine the direction of the interface.

In addition, the momentum equation is also solved throughout the domains:

$$\frac{\partial(\rho\vec{u})}{\partial t} + \nabla.(\rho\vec{u}\vec{u}) = -\nabla p + \nabla.\mu[\nabla\vec{u} + (\nabla\vec{u})^T] - \vec{F}_{sf} + \rho\vec{g} \tag{3.9}$$

The term $\vec{F}_{sf}$ in equation (3.9) is the force due to surface tension. Based on continuum surface force (CSF) model, this term can be written as:

$$\vec{F}_{sf} = \sigma\kappa\delta(\phi)\vec{n} \tag{3.10}$$

where σ is the surface tension coefficient, $\kappa = \nabla.\frac{\nabla\phi}{|\nabla\phi|}\Big|_{\phi=0}$ is the local mean interface curvature, $\vec{n} = \frac{\nabla\phi}{|\nabla\phi|}\Big|_{\phi=0}$ is the local interface normal, and

$$\delta(\phi) = \begin{cases} 0 & |\phi| \geq a \\ \dfrac{1 + \cos\left(\frac{\pi\phi}{a}\right)}{2a} & |\phi| < a \end{cases} \tag{3.11}$$

where a is the thickness of the interface. We also adopted wall adhesion model to include the effect of contact angle. In this model, the surface normal of the cell next to the wall can be calculated as:

$$\vec{n} = \vec{n}_w cos\theta + \vec{t}_w sin\theta \tag{3.12}$$

where $\vec{n}_w$ and $\vec{t}_w$ are unit vectors normal and tangential to the wall and θ is the contact angle.

SIMPLEC pressure-based solver was used for solving the flow problem. For convection term of equations, Least Square Cell Based method was adopted for evaluation of gradients. Furthermore, PRESTO! was used for pressure discretization.

In addition, since Courant number ($C = \frac{\Delta t\, V_{fluid}}{\Delta x}$, where Δt is time step, Δx is the cell size, and V_{fluid} is the fluid velocity) is an important dimensionless parameter that greatly influences the stability of numerical simulation in multiphase flow problems, the adaptive time stepping algorithm was used to hold the maximum C number to 0.25 throughout the simulation.

Results and discussion

Dynamics of shear-dependent micro-vortices

Several factors determine the droplet generation regime, α, TOF, and likelihood of micro-vortices formation. These include viscosity and flow rate ratio of dispersed to continuous phase, interfacial tension, and channel geometry (e.g., orifice width, channel height, etc.). By

fixing the composition of dispersed and continuous phases, we evaluated the effect of flow rate ratio and orifice width on formation of micro-vortices. For this purpose, we picked 3 different device versions with orifice width of 10,15, and 20 μm. In addition, we fixed the flow rate of dispersed phase at 0.35 $\frac{\mu L}{min}$, so that the changes in flow rate ratio could be directly correlated with the changes in capillary number.

Based on the results (Fig. 3.3A), for a given orifice width, the recirculation vortex streamlines are not formed at low capillary numbers. This is due to the combination of the following three conditions observed in the squeezing regime: (i) the oil flow rate is not strong enough to induce the recirculation streamlines in the aqueous phase, therefore the aqueous-oil interfacial shearing rate (α) is insignificant, (ii) mode of droplet generation in the squeezing regime; unlike the dripping regime (where the droplet breakup occurs due to Rayleigh-Plateau instability break up)— in the squeezing regime— droplet break up occurs due to the pressure built up in the continuous flow lines due to the obstruction of the orifice by the dispersed phase,[128] and (iii) Tip Oscillation frequency (TOF) is low (< 100 Hz). By increasing the flow rate of continuous phase and, consequently, the capillary number, the regime gradually shifts from squeezing to dripping, where both the α and the TOF become significant for the recirculation vortex to be observable. While the high aqueous-oil interfacial shearing rate (α) at the orifice creates the micro-vortices inside the aqueous phase, high TOF (lower protrusion and retraction of the dispersed phase thread) helps maintaining the stability of the system. This contrasts with the squeezing regime where the high protrusion and retraction of the aqueous tip disrupts the stability of micro-vortices, if any. These findings indicate that there exists a capillary-number threshold, above which the

micro-vortices are formed in dripping regime. Furthermore, our experimental results also show that this threshold is higher for wider orifice widths.

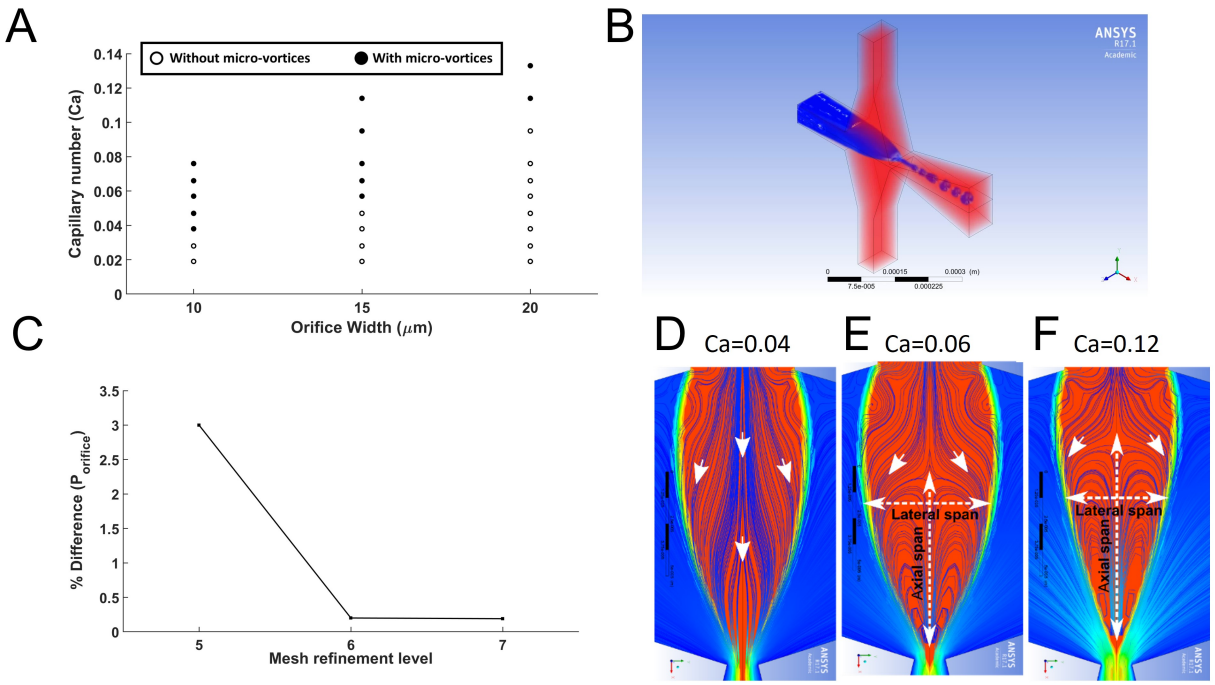

Figure 3.3 Dynamics of shear-dependent micro-vortices
(A) Formation of micro-vortices as a function of orifice width and capillary number, **(B)** 3D modeling of droplet generation. **(C)** grid independent study of numerical modelling with four different mesh refinement levels, **(D-F)** numerical modelling results for different capillary numbers; **(D)** In the squeezing regime, the recirculation vortices are absent, instead the streamlines are directed toward the orifice as a 'through-flow', **(E)** Increasing Ca to 0.06, the droplet generation regime shifts from squeezing to dripping and the recirculation vortices start to establish. **(F)** Further increase in the capillary number ($Ca = 0.12$) increases the axial span and decreases the lateral span of the vortices due to the increase in the shearing rate. d_{gap} also decreases moving from **(E)** to **(F)**.

3-D modelling of droplet generation (Fig. 3.3B; Movie 3.1, Supporting Information) was performed to obtain flow streams in the flow focusing junction at various capillary numbers. First, grid independent study was performed with four different mesh refinement levels, corresponding to 100k (level 4), 500k (level 5), 1M (level 6), and 2M (level 7) mesh elements. The simulation time for these levels were 10, 16, 30, and 42 hours, respectively, which indicates the high computational cost of modelling such complex physics. For each mesh

refinement level, total pressure was measured at the center of the orifice and percentage difference was calculated compared to the previous level. Based on the results (Fig. 3.3C), we picked mesh refinement level 6 for the rest of the study. The droplet generation modelling was then validated with experimental results (Fig. 3.3A) for orifice width of 15 μm and different capillary numbers. According to the results (Fig. 3.3D-F), our developed numerical model accurately predicts the capillary-number threshold at which the micro-vortices occur, as both experimental and numerical results predict the capillary-number threshold to be in the range of 0.04-0.06.

In the next step, we numerically explored how the pattern of such micro-vortices change at different capillary numbers within dripping regime. If Ca is relatively small, the rate of continuous shearing is relatively weak, decreasing the axial span of the vortices (Fig. 3.3E). Also, at this Ca, the dispersed phase extends and forms a curved liquid-liquid interface increasing the lateral span. When the capillary number is further increased, the shear rate imposed by the continuous phase on the dispersed phase is consequently increased, which extends the vortices backward increasing the axial span (Fig. 3.3F, Movie 3.2, Supporting Information). However, the high rate of shear applied by the continuous phase pushes the dispersed phase symmetrically from all directions reducing the curvature of the liquid-liquid interface and thereby decreasing the lateral span. Notably, the greater the lateral span the larger the d_{gap}. We utilize this capability in performing particle trapping and release operations.

Evaluation of micro-vortices trapping size threshold (d_{gap}) for trap & release of particles

Figure 3.4 illustrates the generic model describing the particle dynamics in the micro-vortices. The likelihood of a particle being trapped in micro-vortices depends on whether its center lines up with vortex streamlines or the streamlines exiting through the d_{gap} out of the orifice and into forming the droplets. The former leads to particle trapping while the latter result in particle encapsulation in droplets (Fig. 3.4A). The fundamental principle of such a mechanism is indeed similar to several key hydrodynamic size-based separation techniques such DLD pillar arrays,[129] acoustic streaming,[86, 121] and inertial microfluidics.[130]

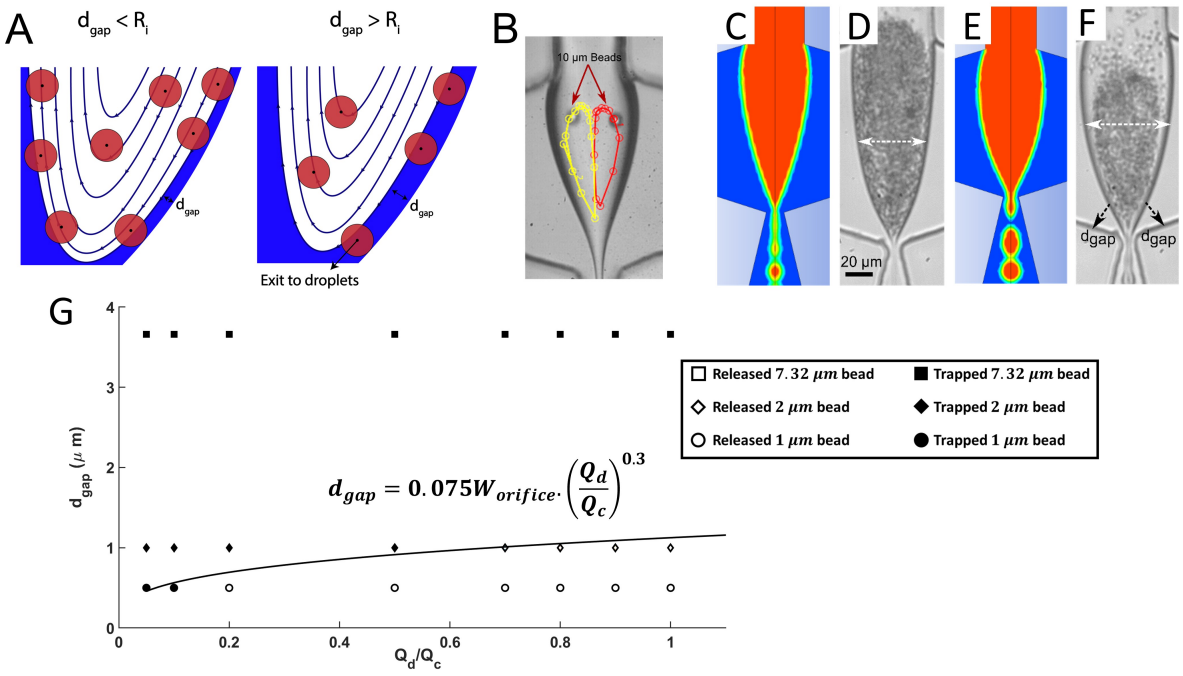

Figure 3.4 Evaluation of micro-vortices trapping size threshold (d_{gap}) for trap & release of particles
(A) Schematic illustrating particle dynamics in the vortex streamlines. If $d_{gap} < R_i$, the center of the particles align within the vortex streamlines and, thus, trapping occurs. When $d_{gap} \geq R_i$, particles start to be released into the droplets. **(B)** Particle tracing using Image J. Two 10 µm particle recirculating in two independent vortices over 3 cycles indicate that no trajectory shifting occurs during the recirculation. **(C & D)** CFD model and corresponding experimental image of trapping mode, where 1 µm particles are trapped in the vortex. **(E & F)** CFD simulation and experimental image of 1 µm particle releasing mode. **(G)** Theoretical d_{gap} with respect to the flow rate ratios for

$W_{orifice} = 15\ \mu m$. The circle, diamond, and square markers (filled: trapped particels, unfilled: released particles) correspond to experimental results for 1 μm, 2 μm, and 7.32 μm polystyrene particles, respectively.

In our design, once shear dependent micro-vortices are formed in dripping regime, by introducing a particle with radius of R_i, particle trapping occurs if $d_{gap} < R_i$, and release occurs when $d_{gap} \geq R_i$, where R_i is the radius of the particle (Fig. 3.4A). Importantly, we can determine the number of particles releasing into a single droplet. If the $d_{gap} \sim R_i$, few droplets contain more than one particle in it. In contrast, as the $d_{gap} >> R_i$, the generated droplets increasingly contain multiple particles.[118] Figure 3.4B (Movie 3.3, Supporting Information) shows the tracked trajectory of two particles of the same size (10 μm), trapped and recirculating in the two independent vortices (Fig. 3.4B; Movie 3.3, Supporting Information). Except for particle collisions, the continuous recirculation of the particles along its respective streamlines is always observed.

To investigate the trap & release capability, particles with 1 μm size were introduced into the system. Figure 3.4C-F illustrates the simulation and corresponding experimental results for the two operational modes. When the trapping mode is ON ($d_{gap} < 0.5$ μm), the 1 μm particles accumulate in the vortices (Fig. 3.4D). However, it is observed that the increase in the particle concentration (i) increases the local viscosity of the recirculation fluid according to Einstein's effective viscosity formula,[131] (ii) causes particle to adhere to each other, and (iii) affect the hydrodynamic stability of droplet generation and results in irregular particle break into the droplets. In this study, we have not investigated the particle-particle interactions and trajectory shift due to collisions. However, by the continuous monitoring of the flow focusing junction and maintaining particle concentration within the limits, trapping mode ensures 100% trapping of all the particles (Fig 3.4D). When $d_{gap} \geq 0.5$ μm, the

trapped particles start to be released into the droplets (Fig. 3.4F). The lateral span in the release mode is greater than that of the trapping mode. This is attributed to the increase in the d_{gap} (or decrease in the Ca) due to the increase in the dispersed to continuous pressure ratio. Experimentally, the capillary number Ca (and d_{gap}) is altered by changing the dispersed phase to continuous phase flow rate ratio. It is also observed that the d_{gap} doesn't change instantly to the change in φ, and there exists a transient period before reaching the stability.

In the next step, we evaluated the accuracy of the developed theoretical model in predicting particle trapping and release. According to equation (3.6), there exists a power-law relation between the d_{gap} and the flow rate ratio of dispersed to the continuous phase. Using numerical modelling, the constant C_1 in equation (3.6) was found to be 0.25. For different flow rate ratios of dispersed to continuous phase, Fig. 3.4G shows the theoretical values of d_{gap} and experimental data for 1 μm, 2 μm, and 7.32 μm particles. According to Fig. 3.4G, there is a relatively good match between experimental and theoretical results. However, equation (3.6) cannot accurately predict the trapping of 1 μm at low flow rate ratios ($\frac{Q_d}{Q_c} <$ 0.1). This may be due the transition of droplet generation regime to jetting (when $\frac{Q_d}{Q_c} < 0.1$) while the theoretical equation is derived based on the assumption that generation mode is in dripping regime. In addition, based on the results, for the orifice width of 15 μm, we observed that the release of 7.32 μm beads cannot be achieved while keeping the micro-vortices stable. Increasing the flow rate ratio to release the 7.32 μm beads increases the likelihood of droplet generetion to switch to squeezing regime, and would result in unwanted instability and, ultimately, disappearance of micro-vortices.

Demonstration of selective trap and release capability

Under the dripping regime, by introducing particles of two different size (particle A and particle B), three cases are observed: Case I: $R_A > d_{gap} < R_B$; Case II: $R_A \leq d_{gap} < R_B$; Case III: $R_A \leq d_{gap} \geq R_B$; where R_A and R_B are the radii of particle A and particle B, respectively. In case I, since the d_{gap} is smaller than R_A and R_B, both particle A and particle B gets trapped in the micro-vortices (Fig. 3.5A). However, the dispersed phase continues to exit through the orifice from the d_{gap} as empty droplets. In case II, since the d_{gap} is greater than R_A, particle A exits through the d_{gap} into the orifice and encapsulates in the droplets. Here, since the d_{gap} is less than R_B, particle B is still unable to go through the d_{gap} or encapsulate in the droplets. Consequently, particle B continues to recirculate within the vortex streamline where its center aligns (Fig. 3.5B). In case III, tuning the d_{gap} to be greater than the radius of both particle A and particle B ensures the release of both particles into the droplets. The size selective release of particles is enabled by gradual switching of flow conditions from case I to case III. Notably, the droplet diameter increases with the transition from case I to case III. This is due to the positive correlation between the d_{gap} and the droplet diameter, as both increase with the dispersed phase to continuous phase velocity ratio (φ).[119]

To enable the separation of both particle A and particle B, initially the d_{gap} is tuned for case I, where both the particles get trapped in the vortices. By switching to case II, particle A is filtered out into the droplets while particle B still recirculates in the vortices. To release particle B into the droplets, the d_{gap} is set to case III. This strategy facilitates the release of particles per the ascending order of their sizes. We have experimentally demostrated such capability using 1 μm and 7.32 μm diameter polystyrene particles. For this, dispersed phase containing a mixture of 1 μm and 7.32 μm particles are initially trapped in the vortices (Fig.

3.5C) (Case I: 0.5 $\mu m > d_{gap} < 3.66\ \mu m$) and are later released such that distinct release zones can be defined for each particle size by the d_{gap} thresholds. If the setting is for case II ($0.5\ \mu m \leq d_{gap} < 3.66\ \mu m$), the 1 μm particles are released into the droplets while the 7.32 μm particles remain trapped (Fig. 3.5D).

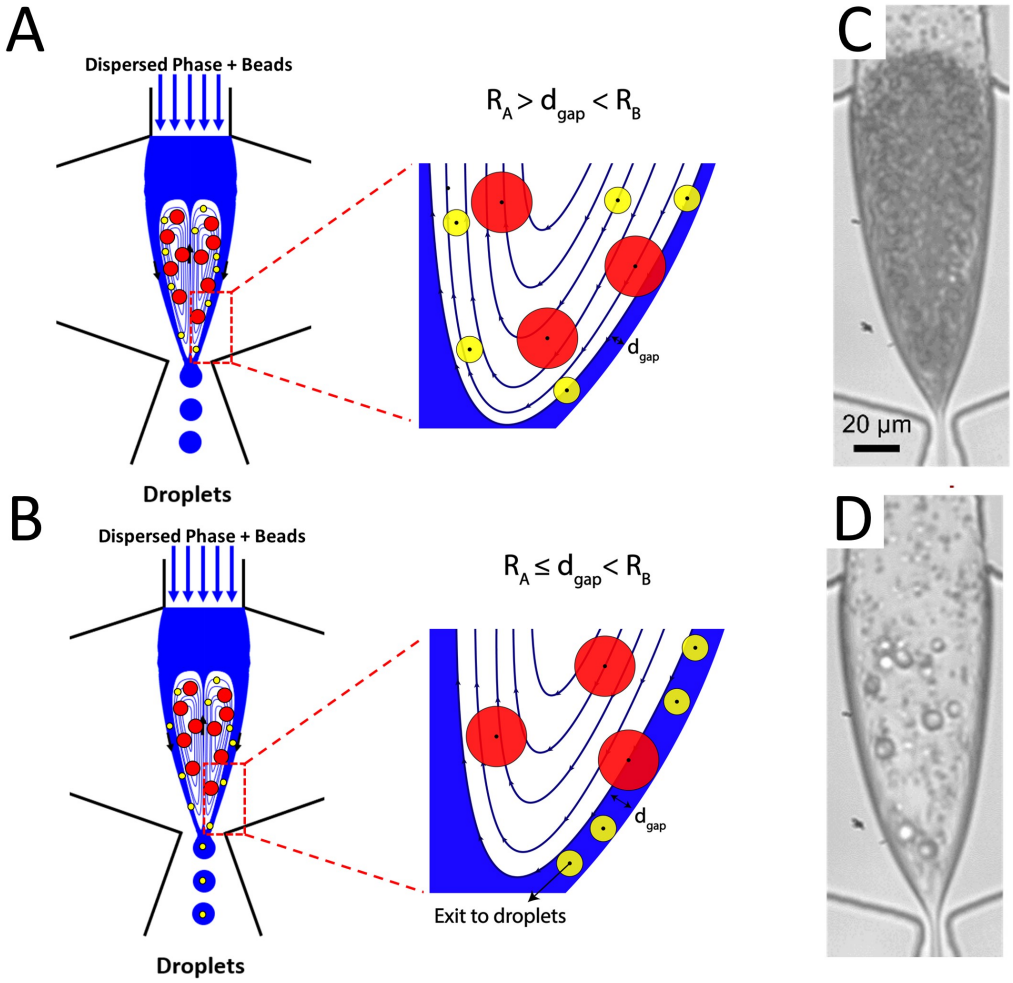

Figure 3.5 Demonstration of selective trap and release capability
(A & B) Schematic illustrating the trap and release capability of the shear dependent micro-vortices. When $R_A > d_{gap} < R_B$, micro-vortices trap both particles. By increasing the d_{gap}, so that $R_A \leq d_{gap} < R_B$, smaller particles, "A", are released into droplets while larger particles, "B", still remain trapped in the micro-vortices. **(C)** Trapping of both 1 µm and 7.32 μm particles in the vortices and **(D)** Release of 1 μm particles leaving the 7.32 μm particles trapped in the inner streamlines

Effect of PDMS surface treatment and channel height on micro-vortices

Using numerical simulation, we investigated the effect of the PDMS surface treatment and microfluidic channel height on the geometry of micro-vortices (Fig. 3.6). The PDMS surface treatment affects the hydrophobicity and, consequently, the contact angle. In this study, we evaluated how micro-vortices are formed for three different contact angles ($\theta = 120°, 140°, and\ 160°$).

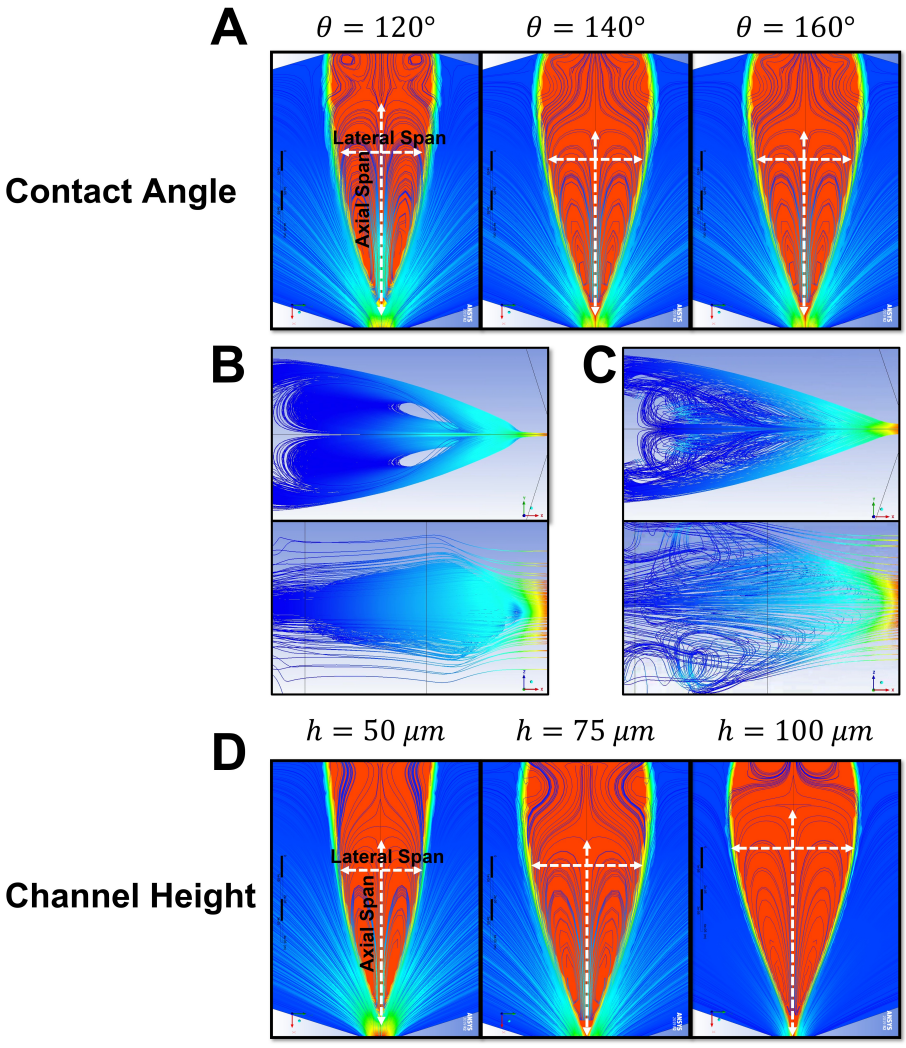

Figure 3.6 Effect of PDMS surface treatment and channel height on micro-vortices
(A) Comparison of micro-vortices geometry for different contact angles (PDMS surface treatments) (contact angle ↑: Lateral Span ↑, Axial Span ↓) with the corrsponding 3D streamlines for **(B)** θ=120° and **(C)** θ=160°. **(D)** Comparison of micro-vortices geometry for different microchannel heights (channel height ↑: Lateral Span ↑, Axial Span ↑).

According to the results (Fig. 3.6A), increasing the hydrophobicity of the microchannels causes the interface between the continuous and dispersed phases to be more convex and, thus, results in increasing the lateral span of the micro-vortices while decreasing the axial span. In addition, 3-D analysis of micro-vortices indicates that, unlike low contact angle cases (e.g. $\theta = 120°$) where there exist only two symmetric three-dimensionally micro-vortices (Fig. 3.6B; Movie 3.4, Supporting Information), at high contact angles (e.g. $\theta = 160°$) two additional micro-vortices will be formed at both sides of the main micro-vortices (Fig. 3.6C; Movie 3.5, Supporting Information). Figure 3.6D shows micro-vortices geometry for different channel heights. According to the results, by increasing the channel height, the interface becomes more convex in all directions. As a result, both the lateral and axial span of micro-vortices increases by increasing the height. These findings indicate that increasing hydrophobicity and channel height both lead to a higher trapping efficiency especially since the micro-vortices become wider and can hold higher number of cells without significant particle-particle interactions and trajectory shift due to the collisions.

CHAPTER 4: A MICROFLUIDIC 3-PART DIFFERENTIAL SORTER

Introduction

WBCs are one of the major components of human blood that are used for a wide range of patient tests and treatments in clinical settings. CAR T-cell therapy is one type of immunotherapy in which patient's T cells are reprogrammed to attack cancer. This method has already achieved success in clinical settings showing tremendous promise for cancer treatment. WBCs are also indicators for immune system and can be used to determine health status and treatment progression for acute infectious diseases and chronic diseases (e.g., cancer, diabetes, cardio-vascular diseases). Therefore, there is a great need for developing efficient methods that provide isolation of different subpopulation of WBCs from whole blood for further downstream analysis, screening, and processing. Especially, for many of these applications, the capability of processing small volume of blood (down to a drop) is highly advantageous as drawing large volume of blood is sometimes not feasible for patients with critical conditions.

Microdevices using a variety of separation techniques have been developed to identify or sort cells without use of labels and have been covered in several reviews.[132] Electrokinetic technologies can detect inherent cell electrophysiological properties without use of labels. A particularly promising electrokinetic technology for analysis and separation of cells is dielectrophoresis (DEP), in which non-toxic inhomogeneous electric fields induce cell movement.[133]

Dielectrophoresis, first introduced by Pohl in the 1950s,[134] is the induced motion of polarizable particles when placed in a non-uniform electric field. The time-averaged DEP force (F_{DEP}) acting on a polarized particle (with spherical shape) can be expressed as:[135, 136]

$$F_{DEP} = 2\pi\varepsilon_{med}R^3 Re[f_{CM}]\nabla\vec{E}_0^2 \quad (4.1)$$

where ε_{med} is the surrounding medium permittivity, R is the particle radius, $Re[f_{CM}]$ is the real part of Clausius-Mossotti factor, and $\vec{E}_0$ is the electric field. The sign of $Re[f_{CM}]$ is a function of the frequency of the applied electric field (ω) as well as the dielectric properties of the cell and medium and determines the behavior of cells in a non-uniform electric field. Figure 4.1A shows the plot of $Re[f_{CM}]$ with respect to the applied electric field frequency for a cell modeled with the single shell model.[136, 137] For negative values of $Re[f_{CM}]$ ($-0.5 < Re[f_{CM}] < 0$), cells experience negative DEP (nDEP) and are repelled from high electric field regions. When $Re[f_{CM}]$ is positive ($0 < Re[f_{CM}] < 1$), cells are attracted toward high electric field regions and thus experience positive DEP (pDEP). However, at two specific applied frequencies, termed the first and second cross-over frequencies (f_{xo1} and f_{xo2}), the cells experience no induced DEP force due to the transition in their polarity.

In high frequency DEP (>10 MHz), cell dielectric properties are mostly affected by the cytoplasm and nucleus. In contrast, at low frequencies (<1 MHz), membrane properties such as membrane capacitance and conductance primarily dictate cell behavior, with capacitance dominating.[138] For viable mammalian cells, specific membrane capacitance (C_{mem}) can be approximated as:[139]

$$C_{mem} = \frac{\sigma_s}{\sqrt{2}\pi R.\, f_{xo1}} \quad (4.2)$$

where σ_s is the electrical conductivity of the medium.

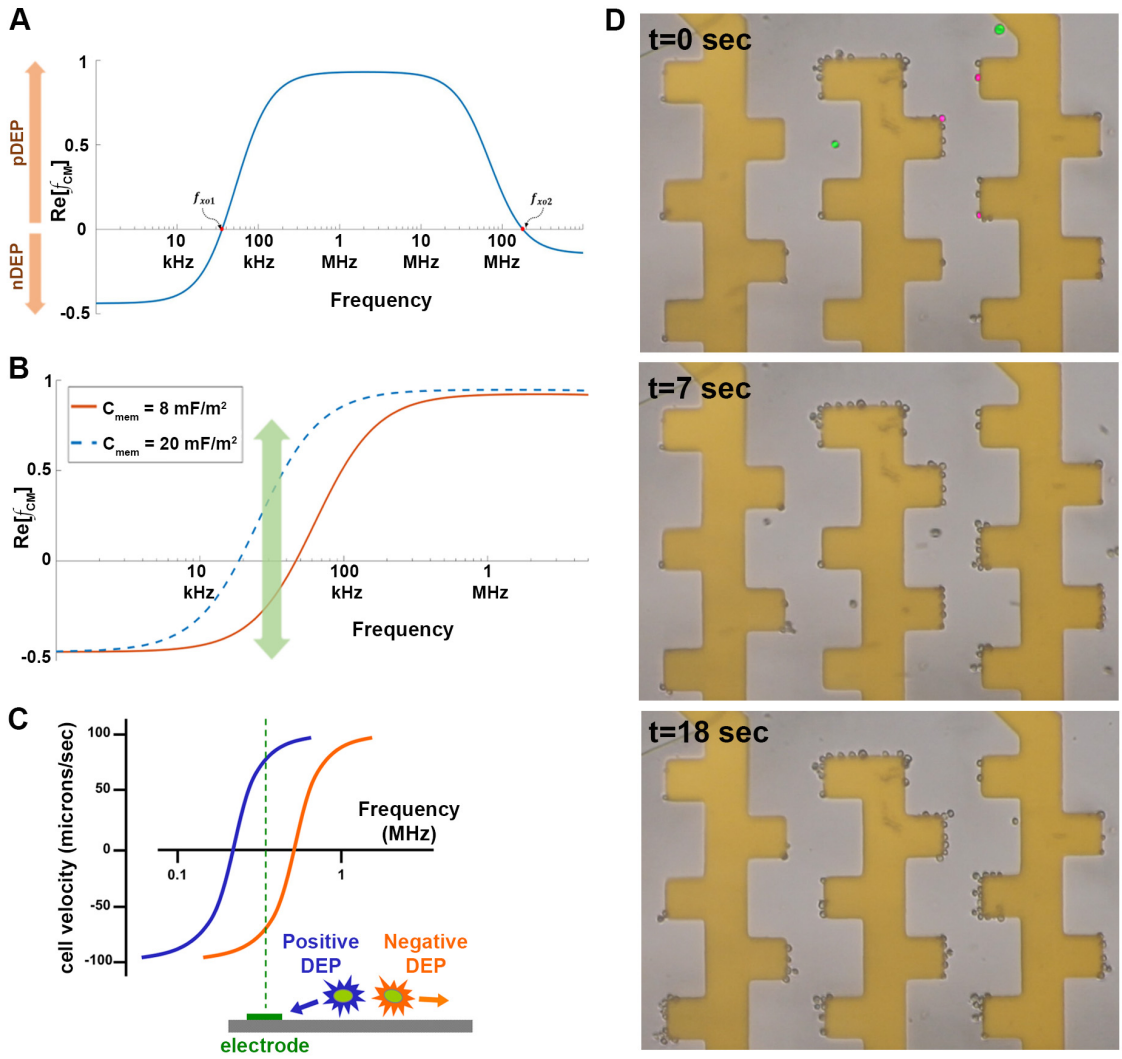

Figure 4.1 Working principles of dielectrophoresis (DEP)
(A) Plot of the real part of the Clausius-Mossotti factor ($Re[f_{CM}]$) with respect to the frequency of the applied electric field for a cell modeled with the single shell model (parameters obtained from ref [140][140]). Based on the sign of $Re[f_{CM}]$, cells will experience different motions (nDEP or pDEP) in a non-uniform electric field. At crossover frequencies f_{xo1} and f_{xo2}, the cells experience no DEP force. **(B)** $Re[f_{CM}]$ for two cells with different membrane capacitance values; the difference in membrane capacitance results in distinct DEP responses at certain frequency ranges. **(C)** Schematic depicts the differential responses of two unique cell types in DEP. Since the cells have different frequency responses and membrane capacitance values, a frequency can be chosen (denoted by dashed green line) at which one cell is in pDEP and the other in nDEP, providing a force for separating the two cell types. Reprinted with permission from Flanagan et al, 2008.[141] **(D)** Still images show E12 mouse neural stem cells in a microfluidic DEP trapping device with frequency set to 100 kHz such that some of the cells experience pDEP and are attracted to electrode edges (electrodes in gold) while others in nDEP pass by (to aid visualization of cells, some cells in pDEP in first panel are colored pink while those in nDEP are green).[142] From ref (143)[143] with permission from John Wiley and Sons.

As the majority of DEP-based techniques utilize frequency ranges lower than 1 MHz, the differences in cells' C_{mem} values have mainly been exploited for cell characterization and sorting.[144, 145] Measurement of C_{mem} can be achieved by different methods such as DEP and impedance sensing ($C_{mem} = -\frac{j}{2\pi\omega(\frac{Z_m}{2})}$), where Z_m is the specific membrane impedance of the cell.[146] Figure 4.1B shows $Re[f_{CM}]$ for two cells having identical dielectric properties except for C_{mem}. Due to the difference in C_{mem}, there exists a frequency range at which one type of cell experiences nDEP while the other experiences pDEP. Most DEP-based methods have taken advantage of such distinct differences in DEP response to sort cells based on C_{mem} (Fig. 4.1C).

DEP exploits inherent cell physical properties to distinguish different types of cells and thus requires no cell labeling (Fig. 4.1D). Since cell behavior in DEP at lower frequencies is dependent on membrane physical properties as well as the total amount of membrane, which is affected by cell size, DEP can distinguish similarly sized cells as long as their membrane properties significantly differ. The beauty of DEP lies in the fact that even subtle cell features, such as cell membrane morphology and integrity, affect overall cell dielectric properties and can lead to distinct behavior in DEP.[133, 144] For example, membrane capacitance and cell behavior in DEP distinguish normal and malaria infected red blood cells,[147] stimulated and unstimulated Jurkat cells,[148] and breast cancer cells expressing different amounts of the neu oncogene.[149] Considering these advantages, there has been growing interest in the use of DEP to characterize, manipulate, and separate different types of cells. This is shown by the over 400% increase in DEP publications since 2000.[133] DEP has been used extensively for characterization and separation of a variety of cell types, including red and white blood cells,[150-153] apoptotic/necrotic cells,[154] circulating tumor cells (CTCs),[155-

[157] and stem cells.[158] A good example is the use of DEP to isolate CTCs. Gascoyne and colleagues showed that the dielectric properties of a wide variety of tumor cells (60 diverse human cancer cell types in the National Cancer Institute NCI-60 panel) significantly differ from those of blood cells, making DEP an ideal choice to discriminate tumor cells from blood cells.[144, 156]

Here, an integrated microfluidic platform is presented that provides 3-part differential sorting of WBCs from whole blood. This platform consists of two modules: (i) On-chip enrichment of WBCs from whole blood sample, and (ii) DEP separator chip for 3-part differential sorting of enriched WBCs. Once the sample is introduced in the system, on-chip lysis of RBCs is first performed using ACK (Ammonium-Chloride-Potassium) lysis buffer. The enriched WBCs are then introduced into a two-step DEP separator chip where distinct electrophysiological properties of monocytes, granulocytes, and lymphocytes are used for sorting. The developed platform is capable of efficient isolation of viable monocytes, granulocytes, and lymphocytes from undiluted whole blood sample with volumes as low as 50 µl. Furthermore, to address the challenge of throughput limitation of existing DEP sorter technologies, a high-throughput DEP sorter chip is also presented that takes advantage of 3D hydrodynamic focusing. Using this design, at least 10 times increase in system throughput could be achieved without significant reduction in system performance.

Results and discussion

On-chip enrichment of WBCs from whole blood

In this goal, a microfluidics system is developed for on-chip lysis of RBCs using ACK lysis buffer. Figure 4.2A shows the design of the microfluidic chip that consists of two individual

inlets for blood sample and lysis buffer. In this module, a serpentine-shaped microchannel design is adopted to ensure effective mixing between whole blood and RBC lysis buffer.[159] As a result, RBCs experience swell and burst inside the microfluidic channel (Fig. 4.2B).

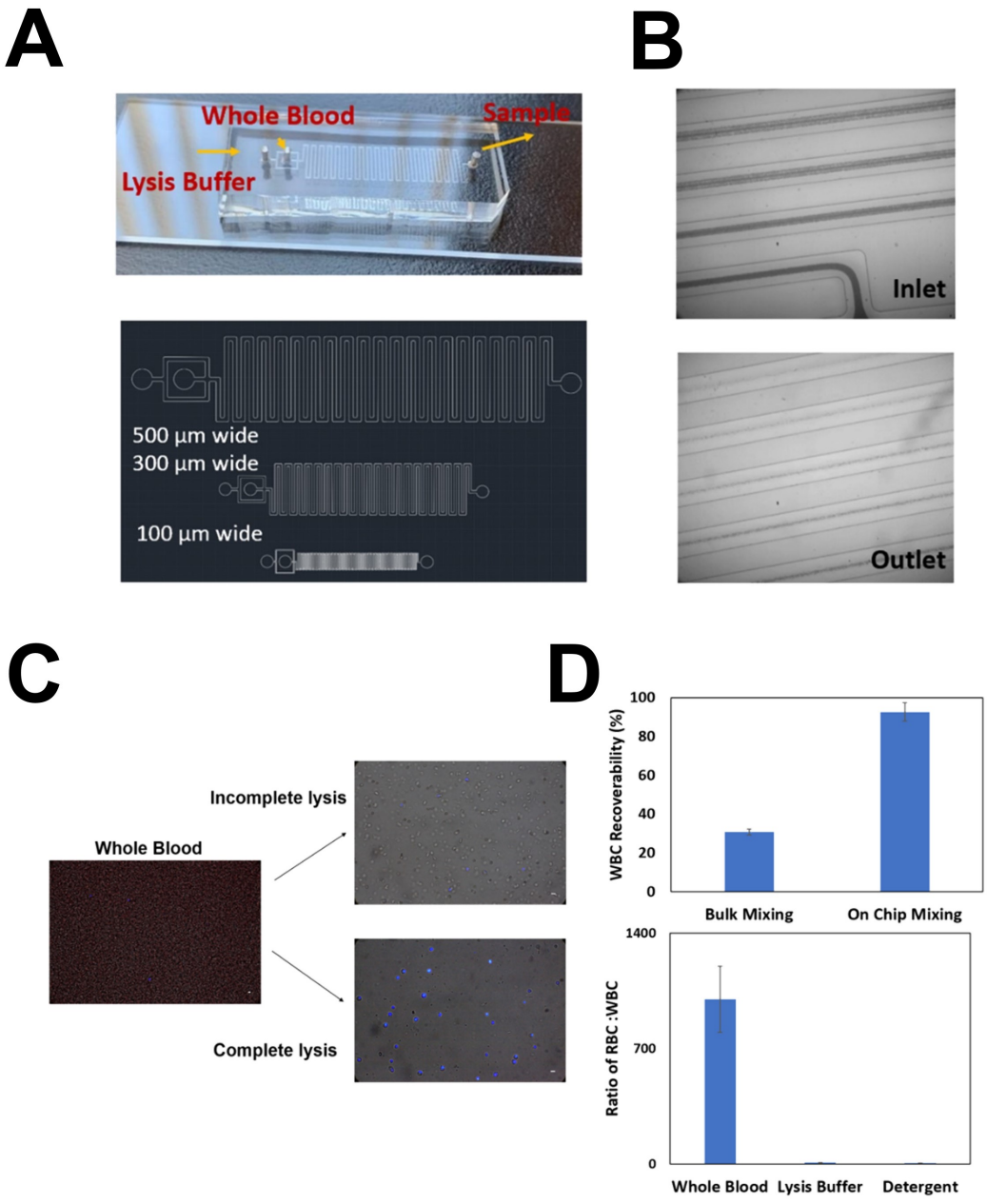

Figure 4.2 On-chip enrichment of WBCs from whole blood
(A) Device design and various geometries. **(B)** High Speed Phantom Image of Inlet and Outlet of the chip when infusing whole blood and ACK lysis buffer. **(C)** Example Image of complete and incomplete RBC lysis. Scale bar: 10µm. **(D)** WBC recoverability and RBC to WBC ratio after RBC lysis (N=3).

As for the two inlets, we optimized the flow rates ratio to be 1:6 (whole blood: lysis buffer) and achieved on-chip mixing within 2 mins at controllable flow rates (0.5 $\frac{\mu L}{min}$ to 40 $\frac{\mu L}{min}$). Short mixing time and incorrect flow rates ratio resulted in incomplete RBC lysis which was improved by longer mixing time by having longer microfluidic channel (Fig. 4.2C). Using the optimized parameters, we obtained enrichment ratio of WBC to RBC of 1:1.8 compared to 1:1000 from whole blood ratio (Fig. 4.2D). In addition, up to 85% WBC recoverability was achieved by on-chip RBC lysis technique compared to <40% obtained by the bulk mixing method (Fig. 4.2D).

Electrophysiological characterization of WBCs

To calculate cells' electrophysiological properties, frequency sweeping was conducted to obtain their crossover frequency (f_{xo1}) based on their movement trajectory in the non-uniform electric field. Such an analysis was performed by particle tracking velocimetry (PTV) method to measure the velocity and trajectories of cells (Fig. 4.3A). Based on the measured values for crossover frequencies and using equation (4.1), membrane capacitance of different subpopulation of WBCs were calculated (Fig. 4.3B). The results indicate that monocytes, granulocytes, and lymphocytes possess distinct electrophysiological properties.

A

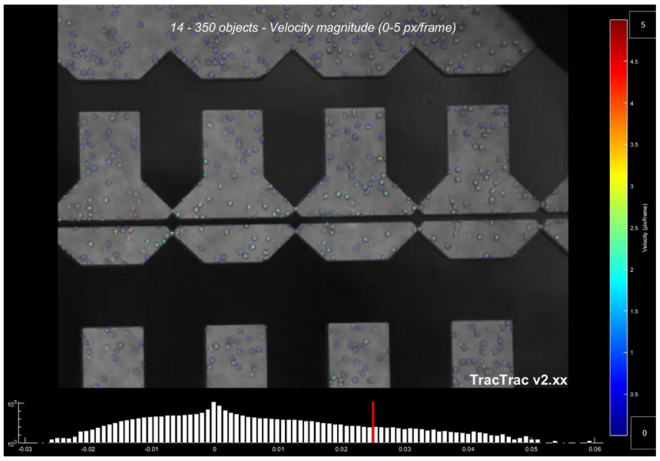

B

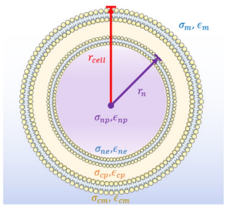

Cell type	f_{ox_1} (kHz)	C_{mem} (mF/m^2)
MON	80-100	6.08
LYM	120-125	5.70
GRA	150	3.17

Figure 4.3 Electrophysiological characterization of WBCs
(A) PTV analysis for measurement of the velocity and trajectories of cells in the DEP characterization chip, **(B)** Measured values of crossover frequency and the corresponding cell membrane capacitance for monocytes, lymphocytes, and granulocytes

Two-Step DEP-based separation of WBCs

Figure 4.4A shows the schematic design of the DEP separator chip. The design consists of two inlets: one for introducing the sample of enriched WBCs and one for introducing the sheath flow. The sheath flow is responsible for focusing the cells before entering the DEP chamber. The DEP separator chamber consists of two sets of interdigitated arrays (IDA) electrodes for two-step sorting of WBCs. Step (1): separation of granulocytes from monocytes and lymphocytes, and Step (2): separation of monocytes from lymphocytes. For each step, electric field voltage and frequency applied to the electrodes was picked based on the results obtained for electrophysiological characterization of WBCs. Specifically, a sinusoidal electric field of $9V_{pp}$ and 1MHz was chosen for separation of granulocytes from monocytes and lymphocytes. Furthermore, a sinusoidal electric field of $7V_{pp}$ and 120kHz was applied to second IDA electrodes for separation of monocytes from lymphocytes.

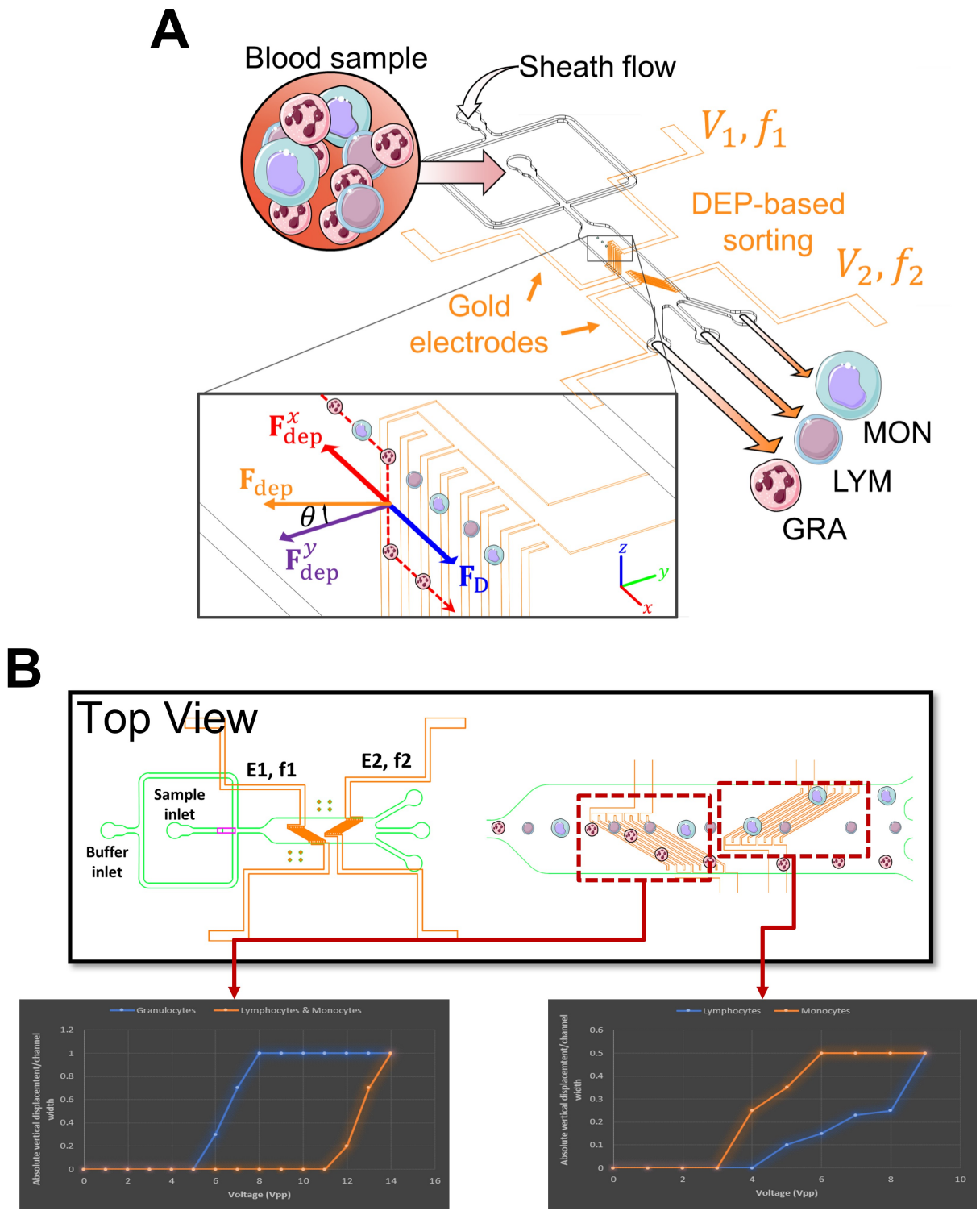

Figure 4.4 Two-Step DEP-based separation of WBCs
(A) Schematic design of the DEP sorter chip, **(B)** The separation results of WBCs in the DEP separator chip consists of two sets of IDA electrodes for two-step sorting of WBCs. Step (1): Separation of granulocytes from monocytes and lymphocytes, Step (2): Separation of monocytes from lymphocytes

The DEP-based sorting performance was further quantified for enrichment of lymphocytes. For this, we performed DEP sorting experiments on both blood from cancer patients and frozen PBMCs from healthy donors. Figure 4.5 reports the separation purity obtained from these experiments. Based on the results, our DEP sorter chip achieved up to 2 times enrichment of lymphocytes for samples from cancer patients and up to 1.5 times enrichment for frozen PBMCs. Compared to cancer sample, the lower enrichment efficiency associated with PBMCs might be due to the thawing and sample preparation steps.

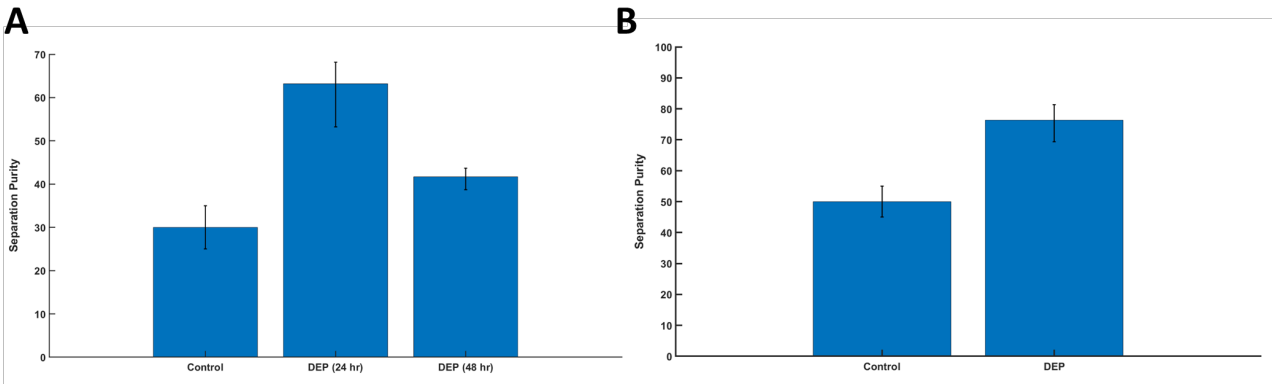

Figure 4.5 DEP sorter chip for enrichment of lymphocytes
(A) The results for blood sample of cancer patients: experiments were conducted within 24 hours and 48 hours of blood withdrawal, **(B)** The results for frozen PBMCs from healthy donors

Integration of 3D hydrodynamic focusing for high-throughput DEP sorting

The fundamental principle of DEP sorting is based on the balance between DEP force (equation (4.1)) and hydrodynamic drag force ($F_{Drag} = 6\pi\mu RV$, where μ is the fluid dynamic viscosity, R is the radius of the cell, and V is the flow velocity relative to the cell).[160] To increase DEP sorting throughput, one approach is to simply operate the system at higher flow rates. However, increasing the flow rate results in an increase in the flow velocity and, consequently, the drag force applied on the cells. Thus, due to dominancy of drag force, DEP force cannot deflect and, consequently, separate the cells of interest. One possible solution is

to change channel dimensions to keep the flow velocity low. In microfluidic channels with rectangular-shaped cross-section (as fabricated in this thesis based on conventional soft lithography technique), the fluid velocity can be expressed as:

$$V = \frac{Q}{\rho W H} \tag{4.3}$$

where Q is the flow rate, ρ is the fluid density, W is the channel width, and H is the channel height. Based on the equation (4.3), increasing channel height, width, or a combination of both keeps the flow velocity low at higher flow rates. Increasing channel width necessitates an increase in the size (length) of the electrode arrays. This can potentially lead to reduction in the impedance of electrodes and, consequently, inefficacy of DEP force by affecting the electric field strength.[161] In addition, the cells need to slide more on top of electrodes which is not preferrable considering the challenge of unwanted cell-to-electrode adhesion. Thus, increasing channel width should be well controlled to avoid such challenges. On the other hand, increasing channel height is an alternative approach to reduce flow velocity at higher flow rates. However, in DEP designs based on planar electrodes, increasing channel height is challenging because electric field decays exponentially along channel height. Consequently, the cells that pass the electrodes closer to the top of microchannel do not experience effective DEP force.

Here, we utilize 3D hydrodynamic focusing to enable use of higher channel heights by keeping cells close to the electrodes. Figure 4.6 shows the schematic design of 3D hydrodynamic focusing integrated upstream of our DEP sorter chamber. This design incorporates a multilayer microchannel design. Once the cells are introduced into the chip, they pass through a narrow constriction. Upon exiting the constriction, the sheath flow

focuses them in Z direction (across channel height). For this study, the narrow constriction has a height of 20µm while the rest of the chip has a height of 150µm.

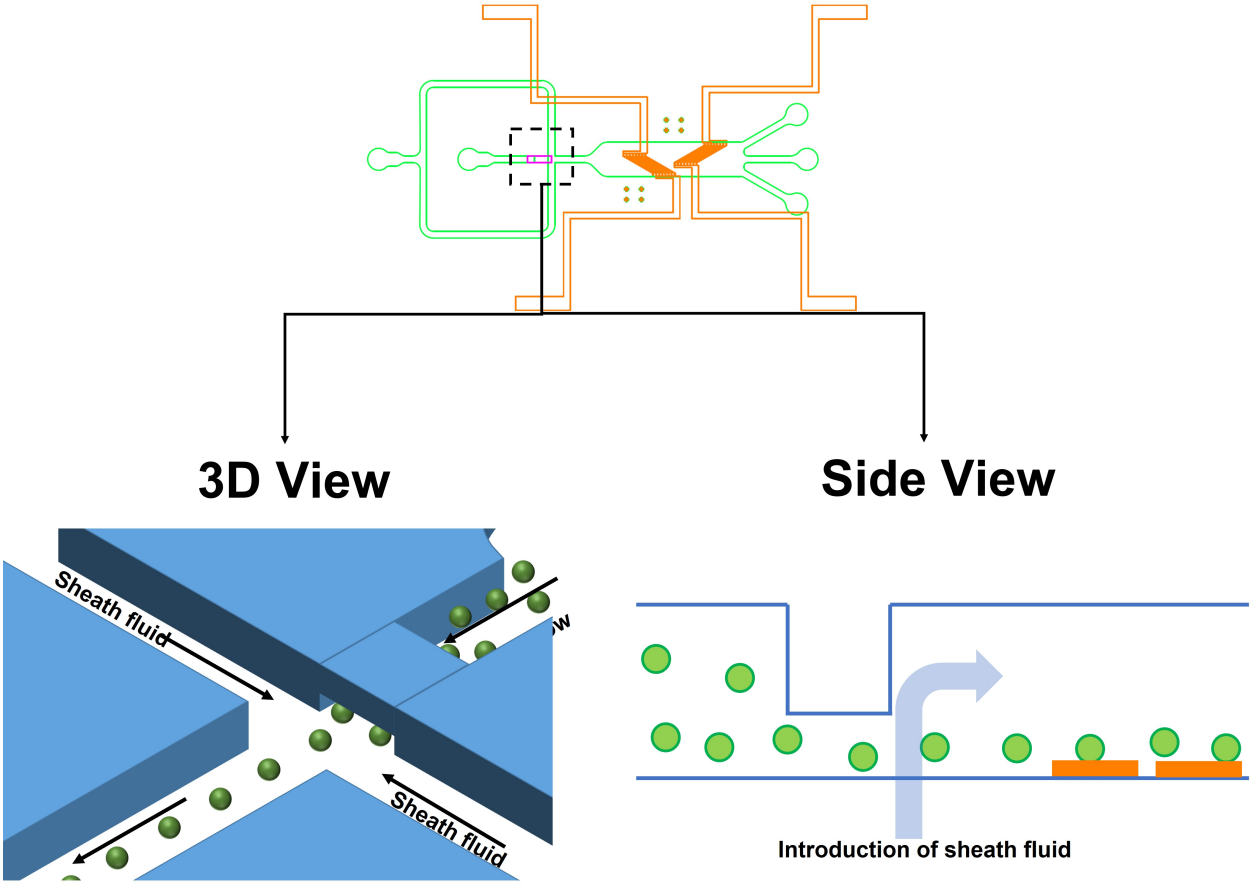

Figure 4.6 Schematic design of 3D hydrodynamic focusing integrated upstream of DEP sorting chamber
This design incorporates a multilayer microchannel design. Once the cells are introduced into the chip, they pass through a narrow constriction. Upon exiting the constriction, the sheath flow focuses them in Z direction (across channel height).

In the first step, numerical modelling (Supplementary Note 5) was performed to find the optimum ratio of sheath flow rate to sample flow rate (Fig. 4.7). According to the results for flow streamlines and particle tracing, we found $\frac{Q_{sheath\ flow}}{Q_{sample}} > 5$ to be the optimum flow rate ratio range that sufficiently focus cells close to the electrodes (average distance of focused cells to the electrodes to be < 50µm).

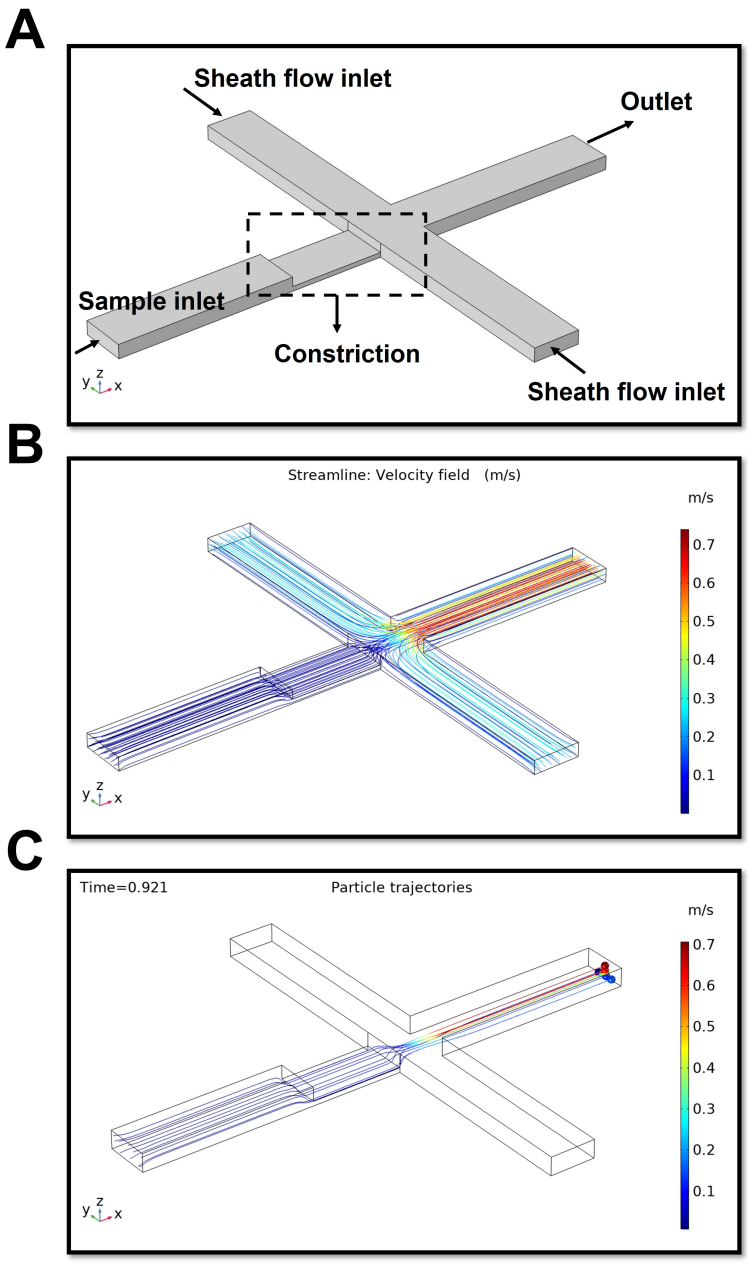

Figure 4.7 Numerical modelling of 3D hydrodynamic focusing
Numerical modelling of 3D hydrodynamic focusing **(A)** The microchannel geometry with the corresponding boundary conditions modelled in this study, **(B)** An example of flow streamlines in the system for $\frac{Q_{sheath\ flow}}{Q_{sample}} = 5$, and **(C)** An example of particle tracing results in the system for $\frac{Q_{sheath\ flow}}{Q_{sample}} = 5$

In the next step, we evaluated the performance of the developed high-throughput DEP system at different sample flow rates. For this purpose, we defined the DEP manipulation efficiency (β) as a metric that quantifies the percentage of cells that are successfully deflected/affected by the electrodes to the designated outlet:

$$\beta = \frac{\#\ of\ deflected/affected\ cells\ by\ electrodes}{total\ \#\ of\ cells\ passinng\ through\ electrodes} \times 100 \qquad (4.4)$$

While β = 100% indicate that all cells are successfully deflected by the DEP force to the designated outlet, β = 0% means that no cells experience strong enough DEP force to be deflected from its trajectory dictated by hydrodynamic drag force. Figure 4.8 shows the results for obtained values of β with respect to the sample flow rate. According to the results, compared to our conventional DEP designs (dashed line), where β decreases rapidly at high flow rates, using the new design we could increase the system throughput up to 50 times while keeping β>70%.

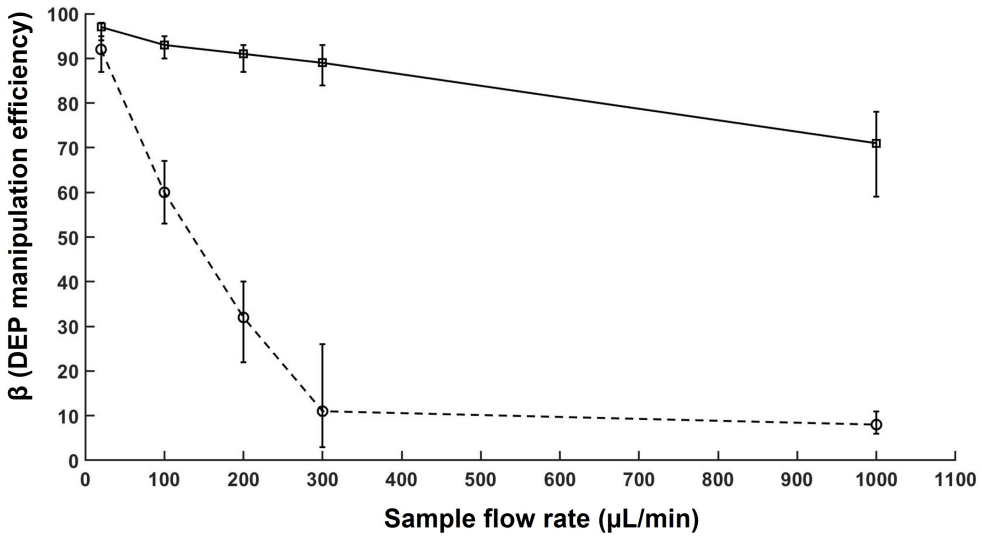

Figure 4.8 DEP manipulation efficiency vs. sample flow rate
The solid line represents the data for the high-throughput DEP sorter chip and the dashed line represents the data for the conventional DEP sorter chip

CHAPTER 5: CONCLUSION AND FUTURE PERSPECTIVE

In this dissertation, we developed microfluidic technologies to address the challenges in cell engineering and analysis which can potentially contribute to the development of more efficient cellular and gene therapies. Specifically, we focused on: (1) Development of an acoustic-electric micro-vortices platform for high-throughput and dosage-controlled intracellular delivery of large cargos; especially for *ex-vivo* cell/gene therapies, this aim addressed the challenges of *in-vitro* delivery of gene-editing cargos into cells, (2) Development of more efficient 1–1 droplet encapsulation methods by theoretical, numerical, and experimental study of shear-dependent microvortices in liquid–liquid flow-focusing geometry; this aim focused on improving the current droplet-based single-cell analysis methods to be used for quality control (QC) of engineered cells, and (3) Development of a dielectrophoresis (DEP)-based microfluidic 3-part differential sorter for isolation of three major subpopulations of white blood cells (WBCs) (lymphocytes, monocytes and granulocytes) from undiluted whole blood; this aim focused on facilitating isolation of target cells for *ex-vivo* cell/gene therapies that require genetic modifications of WBCs.

High-throughput and dosage-controlled intracellular delivery of large cargos by an acoustic-electric micro-vortices platform

Non-viral intracellular delivery of cargos that can rival viral vectors in throughput, viability, and uniformity is an elusive goal for the field of cell engineering. Many promising applications, such as CRISPR-Cas9 gene editing and the biomanufacturing of CAR T cells, rely on effective methods to uniformly deliver large cargos at precise doses across the cell

membranes. However, current non-viral delivery solutions are capable of either precise delivery dosage control or high throughput processing but generally not both. Here, we presented a versatile multimodal acoustic-electric micro-vortices platform capable of precise-dosage delivery of large cargos into both adherent and suspension cells. With this platform, we demonstrated large-plasmid (>9kbp) transfection for CRISPR-Cas9 at 1 million cells/min per single chip. We envision our non-viral intracellular delivery technology to have significant impact on not only the vast and growing field of cellular and gene therapies, but also on the fields of cancer biomarker, vaccine development, cell line generation, stem cell-based medicine, and fundamental biology.

Adoption of the AESOP technology for engineering hard-to-transfect cells

In this dissertation, we demonstrated the capabilities of the AESOP technology mostly with cancer cell lines. Future works will be focused on adoption and development of the AESOP technology for engineering cells that are widely used in cellular and gene therapies such as human primary immune cells and stem cells. These cells are notoriously difficult-to-transfect. To engineer these cells, there are many promising cargo molecules such as plasmid DNA, messenger RNA (mRNA), proteins, small interfering RNA (siRNA), short hairpin RNA (shRNA), etc. We will optimize delivery of different cell reprogramming cargos into the target cells by evaluating the delivery to the membrane, to the cytoplasm, and to the nucleus. First, we will observe interaction between cells and cargos in the micro-vortices but with no electric field. We will explore electric field frequency ranges combined with the acoustic agitation to find the optimum operation parameters to deliver cargos into cells. Especially for such difficult-to-transfect cells, we will evaluate whether it is possible to actively deliver the plasmids to the nuclei.

Investigation on the functionality of cells after gene editing via the AESOP platform

The translational potential of AESOP in engineering cells for therapeutics and fundamental biology not only depends on high cell reprograming efficiency, but also on whether this technology would preserve the functionality of cells after transfection without any severe side effects. Due to the use of gentle electric fields, uniform membrane poration, and dosage-controlled intracellular delivery to minimize delivery of toxic cargos, we hypothesize that AESOP technology preserves the functionality of cells. To test this hypothesis, we plan to: (i) perform an in-depth quantification of the cytotoxicity of AESOP cell-transfection technology; for this purpose, different methods such as the use of viability probes (e.g., propidium iodide, Calcein AM, etc.), Annexin V staining for detecting apoptotic cells, and analyzing non-specific release of cytokines will be used, and (ii) evaluate the downstream functional consequence of gene-edited cells; for this, genome-wide expression profiling techniques will be utilized. The ultimate goal is to optimize mechanical shear and electric field to achieve high transfection efficiency while maintaining cell functionality.

Design prototype of AESOP instrumentation and quantitative benchmark of AESOP with both viral and nonviral transfection techniques

The main reason nonviral transfection methods have not been able to replace viral vectors in clinical applications is primarily due to low transfection efficiency, uniformity, and cell viability at clinical scale throughput. In addition to address the transfection efficiency and cell viability/functionality, future work will also be focused on developing a prototype capable of high throughput cell transfection. With flow control and optimization, the goal is to achieve 10 million cells/min (<10 minutes for processing 1×10^8 cells). This would require optimization of the microfluidic channels and LCATs to maximize cell processing density and

speed. Increasing the channel dimensions (length, width, height) is the most direct way to increase throughput. As an alternative strategy to increase system throughput, parallelization of multiple chips (stacking) would be also adopted. One of the intrinsic advantages of the AESOP technology is that the whole system is compact with pumping, trapping, shearing, and interdigitated electrodes, all on one common microfluidic chip platform. Consequently, the whole system is simple, easy to operate, test, and characterize.

Furthermore, it is important that the platform be benchmarked with current technologies that are widely used for cell transfection. The main nonviral method to benchmark against is electroporation as it is most broadly adopted for high throughput cell transfection. The direct benchmark would be the preserving viability and functionality of the cells at similar transfection efficiency and throughput. An indirect benchmark would be the concentration of cargo molecules required to achieve such transfection performances. Although viral vectors have its intrinsic drawback in safety and cost, the high efficiency and high throughput advantages make it the predominant cell transfection method used in the field. For gene therapy applications, one area that has been a "bottleneck" for viral vector is the cargo size that it can deliver. Compared to majority of viral vectors, that have packaging capacity of 5kbp and higher (e.g., up to 150kbp for HSV-1 vectors or 30kbp for adenovirus), AAVs is the top choice for gene therapy applications, as they are non-integrative, non-inflammatory, and non-pathogenic and offer safe and long-term gene expression. However, the largest size that AAVs can efficiently deliver is about 5Kbp. So far, we could demonstrate delivery of >9Kbp plasmid DNA into cancer cell lines. We will challenge AESOP to deliver higher than 10Kbp plasmids into cells for some of the most advanced cell engineering applications in the field.

Shear-dependent micro-vortices in liquid-liquid flow focusing geometry: A theoretical, numerical, and experimental study

In this dissertation, we performed an in-depth and comprehensive study of shear-dependent micro-vortices in liquid-liquid flow-focusing geometries that has shown promising results for high efficiency 1-1 droplet encapsulation. For this purpose, we utilized theoretical fluid mechanics, CFD modelling, and experimental fluid dynamics to study how these micro-vortices are formed and the factors affecting them. Our results indicate that capillary number is one of the key parameters that determines the generation of such micro-vortices. Specifically, these symmetric three-dimensional micro-vortices mostly occurs at high Ca where the generation is in dripping and jetting regime (not studied here). These micro-vortices enable trapping of particles/cells based on their sizes. In this study, we introduced d_{gap} as the trapping size threshold and, using theoretical fluid mechanics, correlated it to the orifice width and the flow rates of continuous and dispersed phases (power-law relation). The developed mathematical model matches well with the experimental results in predicting size-based particle trapping inside the micro-vortices. We also evaluated how PDMS hydrophobicity and channel heights affect the micro-vortices geometry. Our results indicate that increasing the hydrophobicity of the device results in increasing the lateral span of the micro-vortices while reduces their axial span. In addition, increasing the channel height increases both the axial and lateral span of the micro-vortices. Increasing hydrophobicity and channel height both facilities increasing the capacity of the system to trap larger number of particles/cells and, consequently, improves trapping efficiency.

Building on this foundation, future work involves (i) exploring other key factors affecting the micro-vortices and (ii) improving the developed CFD model. In the present study, the

compositions of the dispersed and continuous phases were fixed, as they result in stable droplet generation and interfacial shearing.[118] However, for widespread adoption of this technique, the effect of different compositions and, consequently, viscosity ratio and interfacial tensions should be explored. The presence of particles in the flow can alter the flow streamlines[162] and increase the chance of particle-particle interaction. In this study, we maintained the particle concentration within limits to minimize these two effects. Future direction of this project will focus on the effect of particle concentration and size on the stability and effectiveness of micro-vortices. As for the CFD model, we used a coupled level-set and VOF method to solve the multiphase flow problem. Such a model has been previously adopted for problems that requires proper resolving of interfacial dynamics, particularly when thin films are present.[127, 163-164] However, this model demands high computational costs because it requires extensive mesh refinement near wall interfaces as well as moving interfaces. For this, we will explore coupling the adaptive-mesh-refinement (AMR) method with our developed model.[165] Although our developed model accurately predicts the formation and dynamics of micro-vortices, it cannot accurately predict the size of droplets generated. This is because of droplet-droplet merging in our coupled level-set and VOF model, which will be further explored in future works.

A microfluidic 3-part differential sorter

This dissertation presented an integrated microfluidic system for isolation of different subpopulation of WBCs (specifically T cells) from small volume of patient's blood (down to a drop). We envision the main application to be for CAR-T cell therapy in improving both cell collection and downstream genetic modification. For that, we were specifically interested in

how the developed platform could enrich lymphocytes. Based on the results, we could achieve >60% lymphocyte isolation purity (up to 2 times increase in enrichment) while maintaining viability. Since one of the main modules of the proposed system is based on DEP technology, we also addressed the cell-processing throughput limitation of existing DEP sorter technologies based on planar IDA electrodes. For this purpose, we integrated a 3D hydrodynamic focusing component upstream of the DEP sorting chamber.

In the current study, we only utilized DEP technology to isolate three major subpopulations of WBCs (granulocytes, lymphocytes, and monocytes) with the main focus on enrichment of lymphocytes. In future studies, we aim to achieve >80% enrichment of lymphocytes. This requires optimization of flow field and electric fields the cells experience. In addition, we will focus on evaluating whether our developed DEP sorter chip can be used for sorting subpopulation of lymphocytes (e.g., B cells and T cells). For this, we plan to perform extensive electrophysiological characterization of these populations and evaluate whether the potential electrophysiological differences can be utilized for sorting.

As for the high-throughput DEP sorter chip based on 3D hydrodynamic focusing, so far, we could increase the throughput by up to 50 times (sample flow rate of 1 ml/min). However, our results showed ~20% decrease in DEP manipulation efficiency compared to our conventional DEP sorter chip. We speculate that at such high flow rates, the current 3D hydrodynamic focusing design is unable to effectively keep the cells close to the electrodes. In future works, we plan to optimize the geometry of the 3D hydrodynamic focusing junction. The main parameters are the height of the constriction and the relative angle of the sheath flow with respect to the sample flow. In addition, we will explore optimization of electrodes' geometry to achieve optimum DEP manipulation of cells at such high flow rates.

BIBLIOGRAPHY

1. K. Bulaklak and C. A. Gersbach, *Nature Communications*, 2020, **11**, 5820.
2. S. Guedan, M. Ruella and C. H. June, *Annual Review of Immunology*, 2019, **37**, 145-171.
3. M. E. Pennesi and C. L. Schlecther, *Ophthalmology*, 2020, **127**, 148-150.
4. S. A. Al-Zaidy and J. R. Mendell, *Pediatric Neurology*, 2019, **100**, 3-11.
5. A. N. Miliotou and L. C. Papadopoulou, *Current pharmaceutical biotechnology*, 2018, **19**, 5-18.
6. M. C. Ramello, E. B. Haura and D. Abate-Daga, *Pharmacological research*, 2018, **129**, 194-203.
7. N. P. Restifo, M. E. Dudley and S. A. Rosenberg, *Nat Rev Immunol*, 2012, **12**, 269-281.
8. A. D. Fesnak, C. H. June and B. L. Levine, *Nat Rev Cancer*, 2016, **16**, 566-581.
9. M. L. Maeder and C. A. Gersbach, *Mol Ther*, 2016, **24**, 430-446.
10. O.-W. Merten, S. Charrier, N. Laroudie, S. Fauchille, C. Dugué, C. Jenny, M. Audit, M.-A. Zanta-Boussif, H. Chautard, M. Radrizzani, G. Vallanti, L. Naldini, P. Noguiez-Hellin and A. Galy, *Human Gene Therapy*, 2010, **22**, 343-356.
11. L. Baldi, D. L. Hacker, M. Adam and F. M. Wurm, *Biotechnology Letters*, 2007, **29**, 677-684.
12. K. Lundstrom, *Diseases*, 2018, **6**, 42.
13. M. A. Mintzer and E. E. Simanek, *Chemical Reviews*, 2009, **109**, 259-302.
14. H. Lv, S. Zhang, B. Wang, S. Cui and J. Yan, *Journal of Controlled Release*, 2006, **114**, 100-109.
15. P. J. Canatella, J. F. Karr, J. A. Petros and M. R. Prausnitz, *Biophysical Journal*, 2001, **80**, 755-764.
16. T. Batista Napotnik, T. Polajžer and D. Miklavčič, *Bioelectrochemistry*, 2021, **141**, 107871.
17. T. Geng and C. Lu, *Lab on a Chip*, 2013, **13**, 3803-3821.
18. Y. Cao, H. Chen, R. Qiu, M. Hanna, E. Ma, M. Hjort, A. Zhang, R. S. Lewis, J. C. Wu and N. A. Melosh, *Science Advances*, 2018, **4**, eaat8131.
19. M. P. Stewart, R. Langer and K. F. Jensen, *Chemical reviews*, 2018, **118**, 7409-7531.
20. A. Sharei, J. Zoldan, A. Adamo, W. Y. Sim, N. Cho, E. Jackson, S. Mao, S. Schneider, M.-J. Han, A. Lytton-Jean, P. A. Basto, S. Jhunjhunwala, J. Lee, D. A. Heller, J. W. Kang, G. C. Hartoularos, K.-S. Kim, D. G. Anderson, R. Langer and K. F. Jensen, *Proceedings of the National Academy of Sciences*, 2013, **110**, 2082-2087.
21. X. Han, Z. Liu, M. c. Jo, K. Zhang, Y. Li, Z. Zeng, N. Li, Y. Zu and L. Qin, *Science Advances*, 2015, **1**, e1500454.
22. J. Yen, M. Fiorino, Y. Liu, S. Paula, S. Clarkson, L. Quinn, W. R. Tschantz, H. Klock, N. Guo, C. Russ, V. W. C. Yu, C. Mickanin, S. C. Stevenson, C. Lee and Y. Yang, *Scientific Reports*, 2018, **8**, 16304.
23. M. T. Saung, A. Sharei, V. A. Adalsteinsson, N. Cho, T. Kamath, C. Ruiz, J. Kirkpatrick, N. Patel, M. Mino-Kenudson, S. P. Thayer, R. Langer, K. F. Jensen, A. S. Liss and J. C. Love, *Small*, 2016, **12**, 5873-5881.
24. Y. Cao, E. Ma, S. Cestellos-Blanco, B. Zhang, R. Qiu, Y. Su, J. A. Doudna and P. Yang, *Proceedings of the National Academy of Sciences*, 2019, **116**, 7899-7904.
25. L. Chang, P. Bertani, D. Gallego-Perez, Z. Yang, F. Chen, C. Chiang, V. Malkoc, T. Kuang, K. Gao, L. J. Lee and W. Lu, *Nanoscale*, 2016, **8**, 243-252.
26. P. Mukherjee, S. S. P. Nathamgari, J. A. Kessler and H. D. Espinosa, *ACS Nano*, 2018, **12**, 12118-12128.
27. H. G. Dixit, R. Starr, M. L. Dundon, P. I. Pairs, X. Yang, Y. Zhang, D. Nampe, C. B. Ballas, H. Tsutsui, S. J. Forman, C. E. Brown and M. P. Rao, *Nano Letters*, 2020, **20**, 860-867.
28. Y. Deng, M. Kizer, M. Rada, J. Sage, X. Wang, D.-J. Cheon and A. J. Chung, *Nano Letters*, 2018, **18**, 2705-2710.
29. J. N. Belling, L. K. Heidenreich, Z. Tian, A. M. Mendoza, T.-T. Chiou, Y. Gong, N. Y. Chen, T. D. Young, N. Wattanatorn, J. H. Park, L. Scarabelli, N. Chiang, J. Takahashi, S. G. Young, A. Z. Stieg, S. De Oliveira, T. J. Huang, P. S. Weiss and S. J. Jonas, *Proceedings of the National Academy of Sciences*, 2020, **117**, 10976-10982.
30. T. Geng, Y. Zhan, J. Wang and C. Lu, *Nature Protocols*, 2011, **6**, 1192-1208.
31. X. Li, M. Aghaamoo, S. Liu, D.-H. Lee and A. P. Lee, *Small*, 2018, **14**, 1802055.
32. B. Joo, J. Hur, G.-B. Kim, S. G. Yun and A. J. Chung, *ACS Nano*, 2021, **15**, 12888-12898.
33. M. Ouyang, W. Hill, J. H. Lee and S. C. Hur, *Scientific Reports*, 2017, **7**, 44757.
34. W. Kang, F. Yavari, M. Minary-Jolandan, J. P. Giraldo-Vela, A. Safi, R. L. McNaughton, V. Parpoil and H. D. Espinosa, *Nano Letters*, 2013, **13**, 2448-2457.

35. P. E. Boukany, A. Morss, W.-c. Liao, B. Henslee, H. Jung, X. Zhang, B. Yu, X. Wang, Y. Wu, L. Li, K. Gao, X. Hu, X. Zhao, O. Hemminger, W. Lu, G. P. Lafyatis and L. J. Lee, *Nature Nanotechnology*, 2011, **6**, 747-754.
36. Y. T. Chow, S. Chen, R. Wang, C. Liu, C.-w. Kong, R. A. Li, S. H. Cheng and D. Sun, *Scientific Reports*, 2016, **6**, 24127.
37. E. Shekaramiz, G. Varadarajalu, P. J. Day and H. K. Wickramasinghe, *Scientific Reports*, 2016, **6**, 29051.
38. Y.-C. Wu, T.-H. Wu, D. L. Clemens, B.-Y. Lee, X. Wen, M. A. Horwitz, M. A. Teitell and P.-Y. Chiou, *Nature Methods*, 2015, **12**, 439-444.
39. J. Cai, S. Huang, Y. Yi and S. Bao, *J Int Med Res*, 2019, **47**, 2199-2206.
40. S. Yoon, P. Wang, Q. Peng, Y. Wang and K. K. Shung, *Scientific Reports*, 2017, **7**, 5275.
41. X. Wang and I. Rivière, *Molecular Therapy - Oncolytics*, 2016, **3**.
42. Y. Li, Y. Huo, L. Yu and J. Wang, *Engineering*, 2019, **5**, 122-131.
43. A. Adan, G. Alizada, Y. Kiraz, Y. Baran and A. Nalbant, *Critical Reviews in Biotechnology*, 2017, **37**, 163-176.
44. M. H. Spitzer and G. P. Nolan, *Cell*, 2016, **165**, 780-791.
45. B. Hwang, J. H. Lee and D. Bang, *Experimental & Molecular Medicine*, 2018, **50**, 1-14.
46. B. Vogelstein and K. W. Kinzler, *Proceedings of the National Academy of Sciences*, 1999, **96**, 9236-9241.
47. A. Adan, Y. Kiraz and Y. Baran, *Current pharmaceutical biotechnology*, 2016, **17**, 1213-1221.
48. S. C. Taylor, G. Laperriere and H. Germain, *Scientific Reports*, 2017, **7**, 2409.
49. A. Lu, H. Liu, R. Shi, Y. Cai, J. Ma, L. Shao, V. Rong, N. Gkitsas, H. Lei, S. L. Highfill, S. Panch, D. F. Stroncek and P. Jin, *Journal of Translational Medicine*, 2020, **18**, 191.
50. Y. Igarashi, T. Uchiyama, T. Minegishi, S. Takahashi, N. Watanabe, T. Kawai, M. Yamada, T. Ariga and M. Onodera, *Molecular Therapy - Methods & Clinical Development*, 2017, **6**, 8-16.
51. *Human Gene Therapy Methods*, 2016, **27**, 197-208.
52. H. N. Joensson and H. Andersson Svahn, *Angewandte Chemie International Edition*, 2012, **51**, 12176-12192.
53. E. Z. Macosko, A. Basu, R. Satija, J. Nemesh, K. Shekhar, M. Goldman, I. Tirosh, A. R. Bialas, N. Kamitaki, E. M. Martersteck, J. J. Trombetta, D. A. Weitz, J. R. Sanes, A. K. Shalek, A. Regev and S. A. McCarroll, *Cell*, 2015, **161**, 1202-1214.
54. A. M. Klein, L. Mazutis, I. Akartuna, N. Tallapragada, A. Veres, V. Li, L. Peshkin, D. A. Weitz and M. W. Kirschner, *Cell*, 2015, **161**, 1187-1201.
55. E. Brouzes, M. Medkova, N. Savenelli, D. Marran, M. Twardowski, J. B. Hutchison, J. M. Rothberg, D. R. Link, N. Perrimon and M. L. Samuels, *Proc Natl Acad Sci U S A*, 2009, **106**, 14195-14200.
56. S. Fiedler, S. G. Shirley, T. Schnelle and G. Fuhr, *Analytical Chemistry*, 1998, **70**, 1909-1915.
57. T. Jiang, Y. Ren, W. Liu, D. Tang, Y. Tao, R. Xue and H. Jiang, *Physics of Fluids*, 2018, **30**, 112003.
58. N. Pamme and A. Manz, *Analytical Chemistry*, 2004, **76**, 7250-7256.
59. S.-C. S. Lin, X. Mao and T. J. Huang, *Lab on a Chip*, 2012, **12**, 2766-2770.
60. P. Li, Z. Ma, Y. Zhou, D. J. Collins, Z. Wang and Y. Ai, *Analytical Chemistry*, 2019, **91**, 9970-9977.
61. S. Duhr and D. Braun, *Proceedings of the National Academy of Sciences*, 2006, **103**, 19678-19682.
62. S. M. Block, *Nature*, 1992, **360**, 493-495.
63. R. H. Cole, S.-Y. Tang, C. A. Siltanen, P. Shahi, J. Q. Zhang, S. Poust, Z. J. Gartner and A. R. Abate, *Proceedings of the National Academy of Sciences*, 2017, **114**, 8728-8733.
64. K. Samlali, F. Ahmadi, A. B. V. Quach, G. Soffer and S. C. C. Shih, *Small*, 2020, **16**, 2070190.
65. M. A. Bijarchi, M. Dizani, M. Honarmand and M. B. Shafii, *Soft Matter*, 2021, DOI: 10.1039/D0SM01764G.
66. D. Di Carlo, *Lab on a Chip*, 2009, **9**, 3038-3046.
67. H.-S. Moon, K. Je, J.-W. Min, D. Park, K.-Y. Han, S.-H. Shin, W.-Y. Park, C. E. Yoo and S.-H. Kim, *Lab on a Chip*, 2018, **18**, 775-784.
68. T. V. Nizkaya, A. S. Gekova, J. Harting, E. S. Asmolov and O. I. Vinogradova, *Physics of Fluids*, 2020, **32**, 112017.
69. A. M. Leshansky, A. Bransky, N. Korin and U. Dinnar, *Physical Review Letters*, 2007, **98**, 234501.
70. M. Yamada, M. Nakashima and M. Seki, *Analytical Chemistry*, 2004, **76**, 5465-5471.
71. G. K. Kurup and A. S. Basu, *Biomicrofluidics*, 2012, **6**, 22008-2200810.
72. H. Liu, M. Li, Y. Wang, J. Piper and L. Jiang, *Micromachines (Basel)*, 2020, **11**, 94.
73. D. J. Collins, A. Neild, A. deMello, A.-Q. Liu and Y. Ai, *Lab on a Chip*, 2015, **15**, 3439-3459.
74. Y.-C. Tan, K. Hettiarachchi, M. Siu, Y.-R. Pan and A. P. Lee, *Journal of the American Chemical Society*, 2006, **128**, 5656-5658.

75. L. Li, P. Wu, Z. Luo, L. Wang, W. Ding, T. Wu, J. Chen, J. He, Y. He, H. Wang, Y. Chen, G. Li, Z. Li and L. He, *ACS Sensors*, 2019, **4**, 1299-1305.
76. M. Chabert and J.-L. Viovy, *Proceedings of the National Academy of Sciences*, 2008, **105**, 3191-3196.
77. T. Jing, R. Ramji, M. E. Warkiani, J. Han, C. T. Lim and C.-H. Chen, *Biosensors and Bioelectronics*, 2015, **66**, 19-23.
78. J. F. Edd, D. Di Carlo, K. J. Humphry, S. Köster, D. Irimia, D. A. Weitz and M. Toner, *Lab on a Chip*, 2008, **8**, 1262-1264.
79. E. W. M. Kemna, R. M. Schoeman, F. Wolbers, I. Vermes, D. A. Weitz and A. van den Berg, *Lab on a Chip*, 2012, **12**, 2881-2887.
80. A. Aiuti, M. G. Roncarolo and L. Naldini, *EMBO Molecular Medicine*, 2017, **9**, 737-740.
81. E. S. Allen, D. F. Stroncek, J. Ren, A. F. Eder, K. A. West, T. J. Fry, D. W. Lee, C. L. Mackall and C. Conry-Cantilena, *Transfusion*, 2017, **57**, 1133-1141.
82. A. Fesnak, C. Lin, D. L. Siegel and M. V. Maus, *Transfus Med Rev*, 2016, **30**, 139-145.
83. A. Künkele, C. Brown, A. Beebe, S. Mgebroff, A. J. Johnson, A. Taraseviciute, L. S. Rolczynski, C. A. Chang, O. C. Finney, J. R. Park and M. C. Jensen, *Biology of blood and marrow transplantation : journal of the American Society for Blood and Marrow Transplantation*, 2019, **25**, 223-232.
84. D. Wang, P. W. L. Tai and G. Gao, *Nature Reviews Drug Discovery*, 2019, **18**, 358-378.
85. A. R. Tovar and A. P. Lee, *Lab on a Chip*, 2009, **9**, 41-43.
86. N. Garg, T. M. Westerhof, V. Liu, R. Liu, E. L. Nelson and A. P. Lee, *Microsystems & Nanoengineering*, 2018, **4**, 17085.
87. W. L. M. Nyborg, in *Physical Acoustics*, ed. W. P. Mason, Academic Press, 1965, vol. 2, pp. 265-331.
88. J. A. Rooney, *Science*, 1970, **169**, 869-871.
89. J. A. Rooney, *The Journal of the Acoustical Society of America*, 1972, **52**, 1718-1724.
90. J. Wu, J. P. Ross and J.-F. Chiu, *The Journal of the Acoustical Society of America*, 2002, **111**, 1460-1464.
91. T. Y. Tsong, *Biophysical journal*, 1991, **60**, 297-306.
92. X. Ding, M. P. Stewart, A. Sharei, J. C. Weaver, R. S. Langer and K. F. Jensen, *Nature Biomedical Engineering*, 2017, **1**, 0039.
93. M. B. Fox, D. C. Esveld, A. Valero, R. Luttge, H. C. Mastwijk, P. V. Bartels, A. van den Berg and R. M. Boom, *Analytical and Bioanalytical Chemistry*, 2006, **385**, 474.
94. J. Olofsson, K. Nolkrantz, F. Ryttsén, B. A. Lambie, S. G. Weber and O. Orwar, *Current Opinion in Biotechnology*, 2003, **14**, 29-34.
95. P. Marmottant and S. Hilgenfeldt, *Nature*, 2003, **423**, 153-156.
96. A. van Wamel, K. Kooiman, M. Harteveld, M. Emmer, F. J. ten Cate, M. Versluis and N. de Jong, *Journal of Controlled Release*, 2006, **112**, 149-155.
97. L. Meng, X. Liu, Y. Wang, W. Zhang, W. Zhou, F. Cai, F. Li, J. Wu, L. Xu, L. Niu and H. Zheng, *Advanced Science*, 2019, **6**, 1900557.
98. I. Lentacker, I. De Cock, R. Deckers, S. C. De Smedt and C. T. W. Moonen, *Advanced Drug Delivery Reviews*, 2014, **72**, 49-64.
99. B. D. M. Meijering, L. J. M. Juffermans, A. v. Wamel, R. H. Henning, I. S. Zuhorn, M. Emmer, A. M. G. Versteilen, W. J. Paulus, W. H. v. Gilst, K. Kooiman, N. d. Jong, R. J. P. Musters, L. E. Deelman and O. Kamp, *Circulation Research*, 2009, **104**, 679-687.
100. Y. Zhou, J. Cui and C. X. Deng, *Biophysical Journal*, 2008, **94**, L51-L53.
101. C. X. Deng, F. Sieling, H. Pan and J. Cui, *Ultrasound in Medicine & Biology*, 2004, **30**, 519-526.
102. F. Yang, N. Gu, D. Chen, X. Xi, D. Zhang, Y. Li and J. Wu, *Journal of Controlled Release*, 2008, **131**, 205-210.
103. Y.-Z. Zhao, Y.-K. Luo, C.-T. Lu, J.-F. Xu, J. Tang, M. Zhang, Y. Zhang and H.-D. Liang, *Journal of Drug Targeting*, 2008, **16**, 18-25.
104. E. M. Darling and D. Di Carlo, *Annu Rev Biomed Eng*, 2015, **17**, 35-62.
105. T. Kotnik, L. Rems, M. Tarek and D. Miklavčič, *Annual Review of Biophysics*, 2019, **48**, 63-91.
106. S. I. Sukharev, V. A. Klenchin, S. M. Serov, L. V. Chernomordik and A. Chizmadzhev Yu, *Biophysical journal*, 1992, **63**, 1320-1327.
107. Y. Demiryurek, M. Nickaeen, M. Zheng, M. Yu, J. D. Zahn, D. I. Shreiber, H. Lin and J. W. Shan, *Biochimica et Biophysica Acta (BBA) - Biomembranes*, 2015, **1848**, 1706-1714.
108. P. Mali, K. M. Esvelt and G. M. Church, *Nature Methods*, 2013, **10**, 957-963.
109. L. L. Lesueur, L. M. Mir and F. M. André, *Mol Ther Nucleic Acids*, 2016, **5**, e291-e291.

110. A. Salari, S. Appak-Baskoy, I. R. Coe, J. Abousawan, C. N. Antonescu, S. S. H. Tsai and M. C. Kolios, *Lab on a Chip*, 2021, **21**, 1788-1797.
111. A. Marin, M. Rossi, B. Rallabandi, C. Wang, S. Hilgenfeldt and C. J. Kähler, *Physical Review Applied*, 2015, **3**, 041001.
112. H. A. Rees and D. R. Liu, *Nat Rev Genet*, 2018, **19**, 770-788.
113. C. L. Xu, M. Z. C. Ruan, V. B. Mahajan and S. H. Tsang, *Viruses*, 2019, **11**, 28.
114. S. L. Maude, T. W. Laetsch, J. Buechner, S. Rives, M. Boyer, H. Bittencourt, P. Bader, M. R. Verneris, H. E. Stefanski, G. D. Myers, M. Qayed, B. De Moerloose, H. Hiramatsu, K. Schlis, K. L. Davis, P. L. Martin, E. R. Nemecek, G. A. Yanik, C. Peters, A. Baruchel, N. Boissel, F. Mechinaud, A. Balduzzi, J. Krueger, C. H. June, B. L. Levine, P. Wood, T. Taran, M. Leung, K. T. Mueller, Y. Zhang, K. Sen, D. Lebwohl, M. A. Pulsipher and S. A. Grupp, *N Engl J Med*, 2018, **378**, 439-448.
115. J. Brooks, G. Minnick, P. Mukherjee, A. Jaberi, L. Chang, H. D. Espinosa and R. Yang, *Small*, 2020, **16**, 2004917.
116. C. A. Lissandrello, J. A. Santos, P. Hsi, M. Welch, V. L. Mott, E. S. Kim, J. Chesin, N. J. Haroutunian, A. G. Stoddard, A. Czarnecki, J. R. Coppeta, D. K. Freeman, D. A. Flusberg, J. L. Balestrini and V. Tandon, *Scientific Reports*, 2020, **10**, 18045.
117. M. E. Kizer, Y. Deng, G. Kang, P. E. Mikael, X. Wang and A. J. Chung, *Lab on a Chip*, 2019, **19**, 1747-1754.
118. G. Kamalakshakurup and A. P. Lee, *Lab on a Chip*, 2017, **17**, 4324-4333.
119. Y.-C. Tan, V. Cristini and A. P. Lee, *Sensors and Actuators B: Chemical*, 2006, **114**, 350-356.
120. G. F. Christopher and S. L. Anna, *Journal of Physics D: Applied Physics*, 2007, **40**, R319-R336.
121. C. Wang, S. V. Jalikop and S. Hilgenfeldt, *Applied Physics Letters*, 2011, **99**, 034101.
122. M. V. Patel, I. A. Nanayakkara, M. G. Simon and A. P. Lee, *Lab on a Chip*, 2014, **14**, 3860-3872.
123. S. Tomotika and G. I. Taylor, *Proceedings of the Royal Society of London. Series A - Mathematical and Physical Sciences*, 1935, **150**, 322-337.
124. T. Ward, M. Faivre, M. Abkarian and H. A. Stone, *ELECTROPHORESIS*, 2005, **26**, 3716-3724.
125. Y.-Y. Tsui, C.-Y. Liu and S.-W. Lin, *Numerical Heat Transfer, Part B: Fundamentals*, 2017, **71**, 173-185.
126. M. Dianat, M. Skarysz and A. Garmory, *International Journal of Multiphase Flow*, 2017, **91**, 19-38.
127. M. Aghaamoo, Z. Zhang, X. Chen and J. Xu, *Biomicrofluidics*, 2015, **9**, 034106.
128. P. Garstecki, M. J. Fuerstman, H. A. Stone and G. M. Whitesides, *Lab on a Chip*, 2006, **6**, 437-446.
129. A. Hochstetter, R. Vernekar, R. H. Austin, H. Becker, J. P. Beech, D. A. Fedosov, G. Gompper, S.-C. Kim, J. T. Smith, G. Stolovitzky, J. O. Tegenfeldt, B. H. Wunsch, K. K. Zeming, T. Krüger and D. W. Inglis, *ACS Nano*, 2020, **14**, 10784-10795.
130. E. Sollier, D. E. Go, J. Che, D. R. Gossett, S. O'Byrne, W. M. Weaver, N. Kummer, M. Rettig, J. Goldman, N. Nickols, S. McCloskey, R. P. Kulkarni and D. Di Carlo, *Lab on a Chip*, 2014, **14**, 63-77.
131. B. M. Haines and A. L. Mazzucato, *SIAM Journal on Mathematical Analysis*, 2012, **44**, 2120-2145.
132. K. A. Hyun and H. I. Jung, *Electrophoresis*, 2013, **34**, 1028-1041.
133. R. Pethig, *J Electrochem Soc*, 2017, **164**, B3049-B3055.
134. H. A. Pohl, *Journal of Applied Physics*, 1951, **22**, 869-871.
135. T. B. Jones, *Electromechanics of Particles*, Cambridge University Press, Cambridge, 1995.
136. T. B. Jones and G. A. Kallio, *Journal of Electrostatics*, 1979, **6**, 207-224.
137. A. Irimajiri, T. Hanai and A. Inouye, *Journal of Theoretical Biology*, 1979, **78**, 251-269.
138. A. Salmanzadeh and R. V. Davalos, in *Microfluidics in Detection Science: Lab-on-a-chip Technologies*, The Royal Society of Chemistry, 2015, DOI: 10.1039/9781849737609-00061, pp. 61-83.
139. K. L. Chan, P. R. C. Gascoyne, F. F. Becker and R. Pethig, *Biochimica et biophysica acta*, 1997, **1349**, 182-196.
140. Y. Polevaya, I. Ermolina, M. Schlesinger, B.-Z. Ginzburg and Y. Feldman, *Biochimica et Biophysica Acta (BBA) - Biomembranes*, 1999, **1419**, 257-271.
141. L. A. Flanagan, J. Lu, L. Wang, S. A. Marchenko, N. L. Jeon, A. P. Lee and E. S. Monuki, *Stem cells (Dayton, Ohio)*, 2008, **26**, 656-665.
142. J. L. Nourse, J. L. Prieto, A. R. Dickson, J. Lu, M. M. Pathak, F. Tombola, M. Demetriou, A. P. Lee and L. A. Flanagan, *Stem cells (Dayton, Ohio)*, 2014, **32**, 706-716.
143. J. L. Nourse, J. L. Prieto, A. R. Dickson, J. Lu, M. M. Pathak, F. Tombola, M. Demetriou, A. P. Lee and L. A. Flanagan, *STEM CELLS*, 2014, **32**, 706-716.
144. P. R. C. Gascoyne, S. Shim, J. Noshari, F. F. Becker and K. Stemke-Hale, *Electrophoresis*, 2013, **34**, 1042-1050.

145. T. N. G. Adams, A. Y. L. Jiang, P. D. Vyas and L. A. Flanagan, *Methods*, 2017, DOI: https://doi.org/10.1016/j.ymeth.2017.08.016.
146. I. Giaever and C. R. Keese, *Proceedings of the National Academy of Sciences*, 1991, **88**, 7896-7900.
147. P. Gascoyne, R. Pethig, J. Satayavivad, F. F. Becker and M. Ruchirawat, *Biochimica et biophysica acta*, 1997, **1323**, 240-252.
148. R. Pethig, V. Bressler, C. Carswell-Crumpton, Y. Chen, L. Foster-Haje, M. E. Garcia-Ojeda, R. S. Lee, G. M. Lock, M. S. Talary and K. M. Tate, *Electrophoresis*, 2002, **23**, 2057-2063.
149. M. Cristofanilli, G. De Gasperis, L. Zhang, M. C. Hung, P. R. Gascoyne and G. N. Hortobagyi, *Clin Cancer Res*, 2002, **8**, 615-619.
150. E. M. Nascimento, N. Nogueira, T. Silva, T. Braschler, N. Demierre, P. Renaud and A. G. Oliva, *Bioelectrochemistry*, 2008, **73**, 123-128.
151. Y. Huang, X.-B. Wang, P. R. C. Gascoyne and F. F. Becker, *Biochimica et Biophysica Acta (BBA) - Biomembranes*, 1999, **1417**, 51-62.
152. M. Hashimoto, H. Kaji and M. Nishizawa, *Biosensors and Bioelectronics*, 2009, **24**, 2892-2897.
153. J. Yang, Y. Huang, X.-B. Wang, F. F. Becker and P. R. C. Gascoyne, *Biophysical Journal*, 2000, **78**, 2680-2689.
154. X. Wang, F. F. Becker and P. R. C. Gascoyne, *Biochimica et Biophysica Acta (BBA) - Biomembranes*, 2002, **1564**, 412-420.
155. S. Shim, K. Stemke-Hale, A. M. Tsimberidou, J. Noshari, T. E. Anderson and P. R. C. Gascoyne, *Biomicrofluidics*, 2013, **7**, 011807.
156. S. Shim, K. Stemke-Hale, J. Noshari, F. F. Becker and P. R. C. Gascoyne, *Biomicrofluidics*, 2013, **7**, 011808.
157. S.-B. Huang, M.-H. Wu, Y.-H. Lin, C.-H. Hsieh, C.-L. Yang, H.-C. Lin, C.-P. Tseng and G.-B. Lee, *Lab on a chip*, 2013, **13**, 1371-1383.
158. A. P. Lee, M. Aghaamoo, T. N. G. Adams and L. A. Flanagan, *Current Stem Cell Reports*, 2018, **4**, 116-126.
159. R. H. Liu, M. A. Stremler, K. V. Sharp, M. G. Olsen, J. G. Santiago, R. J. Adrian, H. Aref and D. J. Beebe, *Journal of Microelectromechanical Systems*, 2000, **9**, 190-197.
160. A. Y. L. Jiang, A. R. Yale, M. Aghaamoo, D.-H. Lee, A. P. Lee, T. N. G. Adams and L. A. Flanagan, *Biomicrofluidics*, 2019, **13**, 064111.
161. M. G. Simon, Y. Li, J. Arulmoli, L. P. McDonnell, A. Akil, J. L. Nourse, A. P. Lee and L. A. Flanagan, *Biomicrofluidics*, 2014, **8**, 064106-064106.
162. Q.-V. Do, D.-A. Van, V.-B. Nguyen and V.-S. Pham, *AIP Advances*, 2020, **10**, 075017.
163. Z. Zhang, J. Xu, B. Hong and X. Chen, *Lab on a Chip*, 2014, **14**, 2576-2584.
164. M. Besanjideh, A. Shamloo and S. K. Hannani, *Physics of Fluids*, 2021, **33**, 012007.
165. M. A. Hashem, A. Aghilinejad, X. Chen and H. Tan, *Journal of Fluids Engineering*, 2020, **142**.
166. J. Heyman, *Computers & Geosciences*, 2019, **128**, 11-18.
167. M. Bauer, M. Ataei, M. Caicedo, K. Jackson, M. Madou and L. Bousse, *Microfluidics and Nanofluidics*, 2019, **23**, 86.
168. R. Lin, J. S. Fisher, M. G. Simon and A. P. Lee, *Biomicrofluidics*, 2012, **6**, 024103.
169. J. C. Weaver, K. C. Smith, A. T. Esser, R. S. Son and T. R. Gowrishankar, *Bioelectrochemistry*, 2012, **87**, 236-243.
170. M. Punjiya, H. R. Nejad, J. Mathews, M. Levin and S. Sonkusale, *Scientific Reports*, 2019, **9**, 11988.

SUPPORTING INFORMATION

Materials and Methods

Chapter 2: High-throughput and dosage-controlled intracellular delivery of large cargos by an acoustic-electric micro-vortices platform

Materials and reagents

Dulbecco's modified Eagle's medium (DMEM), fetal bovine serum (FBS), Iscove's modified Dulbecco's medium (IMDM), Roswell Park Memorial Institute (RPMI) 1640, Dynabeads CD3/CD28, and Human IL-2 Recombinant Protein (Invitrogen) were purchased from Thermo Fisher Scientific. HeLa, K562, and Jurkat (human acute T cell leukemia cell line) cells were purchased from American Tissue Culture Collection (ATCC; Manassas, VA). ImmunoCult™-XF T Cell Expansion Medium was purchased from STEMCELL Technologies. Fluorescein isothiocyanate–dextran molecules were purchased from MilliporeSigma. pcDNA3.1+C-eGFP plasmid and plasmid encoding Cas9 and sgRNA were purchased from GenScript®. For PTEN targeted gene knockout experiment, the 20bp sgRNA sequence of TTATCCAAACATTATTGCTA was used. YOYO-1 dye (1 mM solution in DMSO; Invitrogen, cat. no. Y3601), DAPI (4',6-diamidino-2-phenylindole) stain, CellMask™ Deep Red Plasma membrane Stain, PTEN Monoclonal Antibody, and Goat anti-Mouse IgG (H+L) Highly Cross-Adsorbed Secondary Antibody, Alexa Fluor Plus 647 were purchased from Thermo Fisher Scientific.

Device Fabrication

AESOP integrates interdigitated array (IDA) electrodes with LCAT chip (Fig. S20, Supporting Information). Lift-off technique was adopted for batch electrode fabrication. For this, the

glass slides were, first, cleaned with acetone, isopropyl alcohol, and methanol, and dried overnight at 120°C. Standard photolithography, using MICROPOSIT™ S1813 positive photoresist, was performed to fabricate patterns on the glass slides. Using e-beam evaporation, 300°A chromium (Cr) followed by 1000°A gold (Au) was deposited on the slides. The Cr layer was chosen to improve the adhesion of Au layer to the substrate. After thin film deposition, the glass slides were sonicated in a bath of acetone to remove the photoresist and, subsequently, stripping away unwanted metal layers. Soft lithography technique was employed for fabrication of the LCAT chip. For this, negative photoresist SU-8 2050 (Kayaku Advanced Materials, Inc.) was used for pattern fabrication on silicon wafer. The silicon wafer was then silanized overnight by (TRIDECAFLUORO-1,1,2,2-TETRAHYDROOCTYL)TRICHLOROSILANE (Gelest, Inc.) to avoid PDMS-mold adherence. Poly (dimethylsiloxane), PDMS (Sylgard 184, Dow Corning) base and curing agent were mixed at the ratio of 10:1, poured on the mold, degassed for 1 hour in a desiccator, and cured at 65°C overnight. The cured PDMS was peeled from the wafer, cut to size, and cleaned. Both the LCAT chip and glass slide, with patterned electrodes, were aligned and bonded by oxygen plasma treatment. Finally, to make the AESOP device hydrophobic, it was baked overnight at 65°C.

Standard AESOP operation and intracellular delivery protocol

For efficient transport of acoustic wave from PZT to the device, an ultrasound gel (Aquasonic) was first smeared between the AESOP chip and the PZT (STEMiNC, STEINER & MARTINS, Inc., Resonant frequency = 50.2 kHz). The PZT and AESOP chip were separately connected to a signal generator (Agilent 33220A) and a power amplifier (JUNTEK®). The cell solution was suspended in electroporation buffer (Bio-Rad Laboratories, Inc.), mixed

with the desired concentration of exogenous cargos (e.g., dextran, eGFP plasmid, CRISPR plasmid, etc.), and pipetted into the device inlet in 30 μL sample batches. For pumping the sample into the chip and applying tunable mechanical shear to the cells, the PZT was then excited by a square wave at fixed frequency of 50.2 kHz and the desired amplitude. For electrical expansion of shear-induced pores on cells' membrane, while cells orbiting in acoustic microstreaming vortices, a sinusoidal wave was applied three times (with 30 seconds intervals) to the interdigitated array (IDA) electrodes with the desired frequency, amplitude, and duration. It should be mentioned that throughout 5 minutes device operation, LCATs were turned OFF periodically (every 30 seconds) for uniform mechanical shearing of cells and better mixing of cells with cargos. After delivery, the cells were collected from the device and recovered in cell culture medium without fetal bovine serum (FBS) for 20 minutes. After recovery, the cells were dispersed in their respective culture media supplemented with 10% FBS and incubated in a humidified atmosphere of 5% CO2/95% air at 37°C.

Cell culture

HeLa cells were grown in DMEM supplemented with 10% FBS. K562 cells were grown in IMDM supplemented with 10% FBS. Jurkat cells were grown in RPMI 1640 medium supplemented with 10% FBS. All cells were cultured in a humidified atmosphere of 5% CO_2/95% air at 37°C.

Primary T cell isolation and culture protocols

Whole blood samples from healthy donors were obtained from Institute for Clinical & Translational Science (ICTS) at University of California Irvine. Within 12 hours following blood collection, primary T cells were isolated using immunomagnetic negative selection kits

(STEMCELL Technologies). After isolation, they were suspended with PBS-washed Dynabeads CD3/CD28 at a cell-to-bead ratio of 1:1. Isolated T cells and Dynabeads were cultured in ImmunoCult™-XF T Cell Expansion Medium with 30 U/mL Human IL-2 Recombinant Protein at 37°C in a humidified 5% CO_2 incubator for 3 days. The seeding density of T cells was 1×10^6 cells/mL.

Labeling plasmid DNA, immunofluorescence (IF) staining, flow cytometry, and confocal laser scanning microscopy

For studying mechanism, efficiency, and uniformity of intracellular delivery, plasmid DNA was labeled with YOYO-1 dye at a ratio of 1 dye molecule per 5 bp of the DNA.[30] For this, the desired concentration of plasmid DNA was mixed with the YOYO-1 dye and incubated for 1 hour at room temperature in the dark. The fluorescently labeled DNA was then mixed with the cell sample and intracellular delivery was performed. After sample collection, the cells were washed three times in 1X PBS to remove background and any nonspecifically adsorbed plasmid DNA from the cell surface. The cells were then resuspended in 1X PBS for flow cytometry and confocal laser scanning microscopy.

IF analysis was adopted to evaluate the CRISPR-Cas9–mediated targeted gene knockout efficiency. For this, the cells were first fixed using 4% formaldehyde (pH 7.4) (Polysciences, Inc.) for 10 minutes at room temperature. Then, they were permeabilized by 0.1% Triton X-100 (ICN Biomedicals, Inc.) in 1X PBS for 15 minutes at room temperature and blocked with 3% BSA in PBST (PBS+ 0.1% Tween 20) for 30 minutes at room temperature. Cells were then probed with the diluted primary PTEN antibody in 1% BSA in PBST (1:10 dilution ratio) overnight at 4°C. They were then incubated with the secondary antibody (5 μg/ml) in 1% BSA for 1 hour at room temperature in the dark. The cells were then resuspended in 1X PBS

and plated on a microscope slide for confocal laser scanning microscopy. In between all the IF steps, the cells were washed in 1X PBS three times.

Flow cytometry was performed by a ImageStream Mark II Imaging Flow Cytometer (Amnis Corporation) at 60× magnification under the laser excitation of 488 nm. Confocal laser scanning microscopy was performed by a ZEISS LSM 700 laser scanning confocal microscope (Carl Zeiss) with a 63x oil objective and three laser lines: 405nm for DAPI, 488nm for YOYO-1 labelled plasmid, and 639nm for detecting Alexa Fluor Plus 647 secondary antibodies.

Particle Tracking Velocimetry (PTV) analysis

Cells' motion in acoustic microstreaming vortices was captured using a high-speed camera (Phantom, vision research) connected to a L150 Nikon Eclipse upright microscope. For improved particle detection, high pass filter was used for edge detection. The video was then analysis by an open-source MATLAB code to track the cells and obtain their velocity components in microstreaming vortices.[166]

Cell viability test

The Calcein Red AM (AAT Bioquest) was used to determine the cell viability. For analysis, the cells were resuspended in 1x PBS buffer (ThermoFisher Scientific) and stock solution of Calcein Red AM was added to the cell's solution with 1:100 volume ratio. The flow cytometry was used to evaluate the viability.

Statistical analysis

Quantitative data were presented as mean ± standard error (SE). For all experiments, unless otherwise stated, n=3. The error bars were obtained by technical replicates. Statistical analyses were performed using MATLAB. Student t-test, One-way ANOVA and multiple

comparison with Tukey's honest significant difference criterion were performed to evaluate the statistical significance of differences. P < 0.05 was considered as statistically significant (*P<0.05, **P<0.01, ***P<0.001, and ****P<0.0001) and P > 0.05 as nonsignificant (ns).

The percentage coefficient of variation (%CV) of fluorescent intensity of YOYO-1 dye delivered to the cell population were calculated on at least 95% of YOYO-1 dye positive (gated) cell population as:

$$\%CV = \frac{SD}{\mu} \times 100$$

where SD and μ are standard deviation and mean of fluorescent intensity, respectively.

Chapter 3: Shear-dependent micro-vortices in liquid-liquid flow focusing geometry: A theoretical, numerical, and experimental study

Device fabrication

The microfluidic device is fabricated in polydimethylsiloxane (PDMS) using soft lithography. The device was sealed by placing PDMS in contact with glass cover slides after oxygen plasma treatment. The assembled device was left in an oven at 120 °C long enough to restore PDMS hydrophobicity. The contact angle of aqueous solution used in our study on PDMS was measured to be 140°.[167] An illustration of the setup is shown in Figure 3. For the device used in the experiments, the channel height is 75 μm, as measured by a profilometer.

Solution preparation

Ethyl oleate and 2% ABIL EM 90 form the continuous phase ($\rho_c = 838 \frac{kg}{m^3}$, $\mu_c = 0.04\ Pa.s$), and mixture of water, lipid, glycerol and surfactant form the dispersed phase ($\rho_d = 1000 \frac{kg}{m^3}$, $\mu_d = 0.001\ Pa.s$). Briefly, 5 mg DSPC (1,2-distearoyl-sn-glycero-3-phosphocholine, Avanti Polar Lipids) and 1.96 mg DSPE-PEG2000(1,2-distearoyl-sn-glycero-3-

phosphoethanolamine-N-[methoxy-(polyethylene glycol)-2000], Avanti Polar Lipids) were combined in a glass vial and dissolved in chloroform (CHCl3, Sigma) to form a homogeneous mixture. The solvent was evaporated with a nitrogen stream. 4 mL of ultra-pure water was added to the dry lipid mixture and sonicated at 50℃ for 20 minutes. The solution was combined with an additional 4 mL of glycerol (Sigma), and 2 mL of nonionic surfactant (Pluronic F-68, Sigma), sonicated at 50℃ for 20 minutes. The lipid solution was sonicated again for 15 minutes immediately prior to use to minimize unwanted liposome formation. The surface tension between the two phases was measured to be 35 $\frac{mN}{m}$.

Fluid handling

The fluids are driven using syringe pumps or static pressure pumping approach via house made pressure pumps. As for pressure pumping approach, the fluids are placed in plastic vials and the air pressure above the fluid is regulated by high speed solenoid valves controlled by a custom-built Lab View™ program.[168] The pressure is measured using a pressure gauge (Swagelok) and is reported relative to atmosphere.

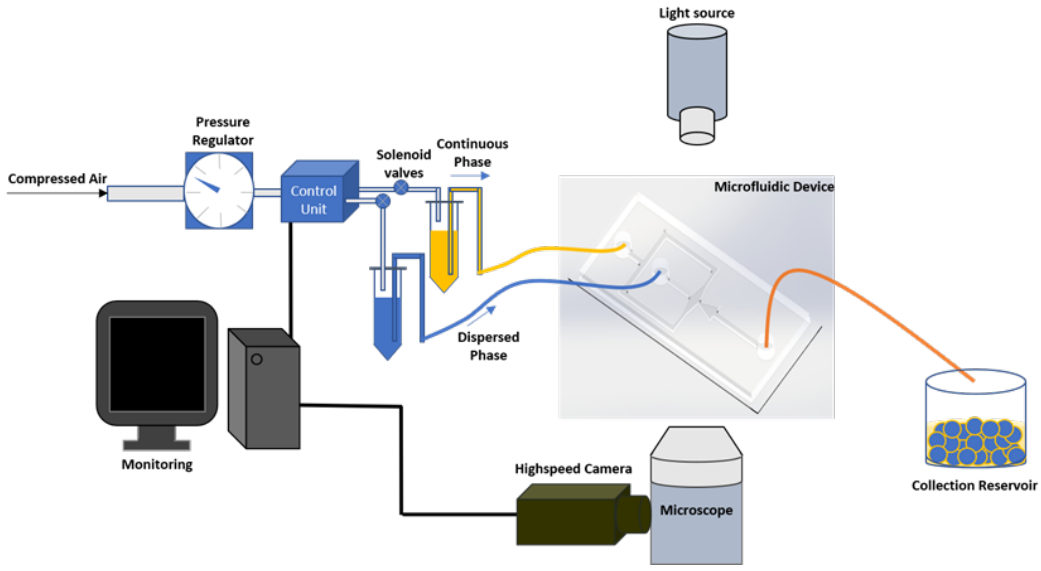

Figure S1 Experimental set up demonstration

Chapter 4: A microfluidic 3-part differential sorter

Device fabrication

The fabrication of the DEP sorter chips consists of two main steps: (1) fabrication of IDA electrodes on glass slides, and (2) fabrication of PDMS-based microchannels. For electrode fabrication, lift-off technique was adopted. For this purpose, the glass slides were first cleaned with Acetone, Isopropyl Alcohol, and Methanol. They were then placed in a 120°C oven overnight to be completely dried. Using photolithography, MICROPOSITTM S1813 positive photoresist was patterned on the glass slides. In the next step, e-beam evaporation was used to deposit 300°A Chromium followed 1000°A Gold layer on the glass slides. The glass slides were then sonicated in the bath of Acetone to remove the photoresist and, consequently, remove unwanted metal layers. As for PDMS-based microchannels, soft-lithography technique was used to fabricate SU-8 molds on silicon wafer substrates. The silicon wafer was then silanized overnight by (TRIDECAFLUORO-1,1,2,2-TETRAHYDROOCTYL)TRICHLOROSILANE (Gelest, Inc.) to avoid PDMS-mold adherence. Poly (dimethylsiloxane), PDMS (Sylgard 184, Dow Corning) base and curing agent were mixed at the ratio of 10:1, poured on the mold, degassed for 1 hour in a desiccator, and cured at 65°C overnight. The cured PDMS was peeled from the wafer, cut to size, and cleaned. Both the PDMS-based chip and glass slide, with patterned electrodes, were aligned and bonded by oxygen plasma treatment.

Cell culture and isolation protocol

Whole blood samples from healthy donors and cancer patients were obtained and processed under UCI IRB-approved clinical protocol. Human Frozen Peripheral Blood Mononuclear Cells (PBMCs) were purchased from STEMCELL Technologies. For some experiments,

lymphocytes, monocytes, and granulocytes were isolated from whole blood or PBMCs using immunomagnetic negative selection kits (STEMCELL Technologies). Jurkat (human acute T cell leukemia cell line) cells were purchased from American Tissue Culture Collection (ATCC; Manassas, VA). Jurkat cells were grown in RPMI 1640 medium supplemented with 10% FBS. The cells were cultured in a humidified atmosphere of 5% CO2/95% air at 37°C.

Particle Tracking Velocimetry (PTV) analysis

As for electrophysiological characterization of WBCs, Cells' motion in DEP characterization chip was captured using a camera with 30fps. For improved particle detection, high pass filter was used for edge detection. The video was then analysis by an open-source MATLAB code to track the cells and obtain their velocity components in the DEP characterization chip.[166]

Supplementary Note 1: Calculation of viscous shear stress near an oscillating bubble at different PZT applied voltages

According to Rooney,[88, 89] the viscous shear stress S as a result of sharp velocity drop across the boundary layer thickness δ in the vicinity of an oscillating bubble is given by

$$S = \frac{2\pi f \epsilon_0^2}{R_0 \delta} = \frac{2\pi^{\frac{3}{2}} \epsilon_0^2 (\rho f^3 \eta)^{\frac{1}{2}}}{R_0} \quad \text{(S1)}$$

$$\delta = \sqrt{\eta/(\pi f \rho)} \quad \text{(S2)}$$

where ρ=1000 kg.m^{-3} is the fluid density, η=0.001 Pa.s is the fluid shear viscosity, f=50.2 kHz is the oscillation frequency, R_0=65 μm is the bubble radius (for specific geometry of LCAT design used in this study), and ϵ_0 is the displacement amplitude of the vibrating bubble. For three different PZT applied voltages corresponding to "low shear (LS)" (PZT voltage = 2V), "moderate shear (MS)" (PZT voltage = 6V), and "high shear (HS)" (PZT voltage = 10V), oscillation of air-liquid interfaces was captured using a high-speed camera (Phantom, vision research) connected to a L150 Nikon Eclipse upright microscope (Video S2). Image analysis was then performed by Phantom Camera Control (PCC) software to obtain ϵ_0 corresponding to each three different PZT applied voltages. According to the results, the displacement amplitudes of 1.5 μm, 6 μm, and 11.9 μm were measured for PZT applied voltages of 2V, 6V, and 10V, respectively. As a result, using equation (S1), viscous shear stress values of 4.3 Pa, 69.4 Pa, and 272.9 Pa were calculated for PZT applied voltages of 2V, 6V, and 10V, respectively.

Supplementary Note 2: Optimization of electric field parameters for cargo delivery

AESOP utilizes interdigitated array (IDA) electrodes to enlarge the small pores initiated by acoustic microstreaming vortices. For each different cell type, electric field voltage (V_{max}), frequency (f), and applied time (T) were optimized. In terms of starting values, we chose V_{max}=7.5V, f=10kHz, and T=10ms for all the cell types. To reduce the complexity associated with such optimization, we fixed T for the rest of study. Such a fixed value for T was chosen to be in the typical range of traditional gene delivery (100μs-1s).[169] In order to avoid unwanted phenomena such as electrolysis on the surface of electrodes and electrothermal flow, we picked 10 kHz as the lower limit of frequencies to be tested.[170] The optimization process was based on two steps: (1) Optimizing 2 MDa dextran delivery, and (2) Optimizing eGFP-expressing plasmid DNA (6.1 kbp) transfection efficiency. The role of step 1 was to save time in narrowing down the feasible domains for V_{max} and f. This is mainly because dextran delivery efficiency can be evaluated in a matter of hours while it takes ~48 hours to determine eGFP transfection efficiency. For both steps, cell viability was also considered as an optimization constraint to be >80%.

For HeLa cells, at f=10kHz, we found out that V_{max}≥12.5V results in >90% dextran delivery efficiency and acceptable cell viability for V_{max}≤17.5V (Fig. S7A). Thus, we narrowed down the applied voltage domain to 7.5V≤V_{max}≤17.5V and performed eGFP transfection

experiments. Based on the results (Fig. S7B), we obtained V_{max}=12.5V as the optimum applied voltage, at which >80% transfection efficiency and cell viability were achieved.

Following the same optimization protocol for Jurkat cells, we could not achieve any desirable transfection efficiency without sacrificing cell viability. As a result, we increased the applied frequency to f=20kHz, where the AC electric field is gentler to the cells. This enabled us to increase the applied voltage to increase transmembrane potential while maintaining viability. Based on the dextran results (Fig. S8A), we narrowed down the applied voltage domain to $10V \leq V_{max} \leq 30V$ for eGFP transfection optimization. According to the results (Fig. S8B), we found V_{max}=25V as optimum applied voltage that resulted in >40% transfection efficiency and >80% cell viability.

For K562 cells, applied frequencies of 10kHz and 20kHz did not result in high transfection efficiency while maintaining viability >80%. Thus, we increased the applied frequency to 30kHz which, consequently, enabled us to explore higher applied voltages without harming the cells. By dextran experiments, we could narrow down the applied voltage domain to $20V \leq V_{max} \leq 40V$ (Fig. S9A). Exploring this domain (Fig. S9B), we optimized the transfection efficiency with respect to electric field voltage and obtained V_{max}=35V as the optimum parameter that gave >50% transfection efficiency and >80% cell viability.

It should be noted that we did not observe any dielectrophoresis (DEP) effect on cells at any of tested electric field parameters.

Supplementary Note 3: Numerical modeling for calculation of the electric field distribution in AESOP platform

COMSOL Multiphysics was used to solve for electric field distribution in the system at [12.5 V_{max}, 10 kHz] (optimum parameters for HeLa), [25 V_{max}, 20 kHz] (optimum parameters for Jurkat), and [35 V_{max}, 30 kHz] (optimum parameters for K562). To reduce the complexity of numerical modeling, a simplified 3D version of microfluidic channel was built and meshed (Fig. S10). In this version, 5 interdigitated array (IDA) electrodes were placed on the bottom of the microfluidic channel. The 3D mesh mainly consisted of tetrahedra elements with triangular 2D elements on boundaries and surfaces.

To solve for electric field distribution, both Gauss's law and charge conservation need to be satisfied. Thus, the electric field E is governed by

$$\nabla \cdot (\mu_m \boldsymbol{E}) = \rho_f \tag{S2}$$

$$\nabla \cdot (\sigma \boldsymbol{E}) + \frac{\partial \rho_f}{\partial t} = 0 \tag{S3}$$

$$\boldsymbol{E} = -\nabla \phi \tag{S4}$$

where μ_m is the medium permittivity, ρ_f is the free charge density, σ is the medium conductivity, t is the time, and ϕ is the electric potential.

Figure S10 shows the distribution of electric field strength/norm corresponding to the optimum parameters obtained for HeLa, Jurkat, and K562 cells. Considering the 2D planar nature of lithography-based microfabrication, semicylindrical bubble shape, frequency of bubble oscillation (kHz range), channel height (60 μm), size of cells (10-20 μm), it is reasonable to assume that the streaming flow in AESOP has a 2D profile and cells are rotating in the middle of the channel height ($h_{microstreaming}$=30 μm).[111] Figure S11 (blue lines) shows

the electric field strength variation at the height 30 μm above the bottom of microchannel for the three optimum parameters obtained for HeLa, Jurkat, and K562 cells, respectively. Based on the results, we calculated the root mean square of the average electric field strength ($|E|_{RMS}$) to be 0.4 kV.cm^{-1} for [12.5 V_{max}, 10 kHz] (optimum parameters for HeLa), 0.85 kV.cm^{-1} for [25 V_{max}, 20 kHz] (optimum parameters for Jurkat), and 0.99 kV.cm^{-1} for [35 V_{max}, 30 kHz] (optimum parameters for K562).

We also evaluated how the electric field is distributed for the "Static" control group where, with having LCAT off, the cells were loaded into the chip and settled down on top of the electrodes. For this purpose, we calculated the electric field strength at the height of 5 μm above the electrodes and compared it with AESOP. According to the results (Fig. S12, green dotted lines), the cells in static group experience stronger average electric field strength compared to AESOP which could potentially result in reduced viability.

Supplementary Note 4: Investigation of PZT-induced local heating and stability of air-liquid interfaces

To achieve the maximum level of performance, AESOP is dependent on stable air-liquid interfaces and minimum PZT-induced local heating. As for air-liquid interfaces, instability (usually in the form of change in size and configuration of bubbles) disrupts the acoustic microstreaming vortices. This issue is especially more prominent in PDMS-based platforms as PDMS is a gas-permeable material. On the other hand, vibration of PZT at high frequencies and amplitudes generates local heating. Local heating does not only contribute to the instability of air-liquid interfaces (bubbles grow with increase in temperature) but also might negatively affect cell viability and transfection efficiency.

Here, we performed a comprehensive analysis on PZT-induced local heating and stability of air-liquid interfaces at different device operational parameters. First, we measured PZT-induced local heating at different PZT applied voltages (2V, 6V, 10V, 20V, and 30V) and duration of operation (0-10 minutes). For this, we put a glass substrate on top of PZT, with an ultrasound gel smeared between them, and measured the temperature of glass every 1 minute. Based on the results (Fig. S18), for PZT voltages of 2V, 6V, and 10V there is no significant increase in the substrate temperature throughout 10 minutes operation of PZT. Especially, under optimum operational parameters used in this study (PZT voltage = 6V, applied time = 5 minutes), the temperature rise is <1ºC. However, for very high applied voltages of 20V and 30V, we recorded ~2ºC and ~3ºC unfavorable temperature rise, respectively.

In the next step, we studied stability of air-liquid interfaces at different PZT applied voltages (6V, 10V, and 20V) and duration of operation (0-20 minutes). Based on the results (Fig. S19),

we did not observe any negative change in size and configuration of air-liquid interfaces throughout 20 minutes investigation of system at PZT applied voltages of 6V and 10V. It should be noted that the optimum operational protocol of AESOP only requires 5 minutes of PZT operation. However, for the case of PZT applied voltage of 20V, we observed significant instability in the air-liquid interfaces as well as generation of bubbles in the system. We speculate that the rise in the substrate temperature (Fig. S18) to be one of major contributing factors to this phenomenon. In addition, high oscillation amplitude of air-liquid interfaces at 20V might also negatively affect the stability of interfaces.

Supplementary Note 5: Numerical modeling for calculation of the flow field distribution and particle tracing in the 3D hydrodynamic focusing system

COMSOL Multiphysics was used to solve for the flow field and trace the particles in the microfluidic device. To reduce the complexity of numerical modeling, a simplified 3D version of microfluidic channel was built and meshed (Fig. 4.7A). The 3D mesh mainly consisted of tetrahedra elements with triangular 2D elements on boundaries and surfaces.

The Navier-Stokes and continuity equations were solved to obtain the flow field in the system:

$$\rho\left[\frac{\partial \boldsymbol{v}}{\partial t} + \boldsymbol{v}.\nabla\boldsymbol{v}\right] = -\nabla p + \eta\nabla^2\boldsymbol{v} \tag{S5}$$

$$\nabla.\boldsymbol{v} = 0, \tag{S6}$$

where ρ, $\boldsymbol{v}$, p and η are the fluid density, velocity, pressure, and viscosity, respectively.

After solving for the flow field, Newton's second law was used to predict the particle trajectory in the flow:

$$\frac{d}{dt}(m_{cell}\boldsymbol{v_{cell}}) = \boldsymbol{F_{Drag}} \tag{S7}$$

where m_{cell} is the mass of the cell, $\boldsymbol{v_{cell}}$ is the cell velocity, and $\boldsymbol{F_{Drag}}$ is the drag force applied on the cell. For a spherical particle in a creeping flow, the drag force can be calculated using Stokes' drag law:

$$\boldsymbol{F_{Drag}} = 6\mu r_{cell}\pi(\boldsymbol{v} - \boldsymbol{v_{cell}}) \quad \text{(S8)}$$

where μ is the fluid viscosity, r_{cell} is the cell radius, $\boldsymbol{v}$ and $\boldsymbol{v_{cell}}$ are the velocities of the fluid and the cell, respectively.

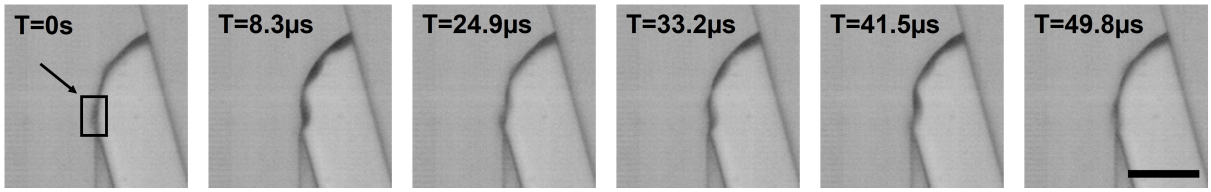

Figure S2 Snapshot images of oscillating air-liquid interface at PZT frequency of 50.2 kHz and applied voltage of 10Vpp. The corresponding high-speed video were captured at 120000 fps. The arrow at timeframe image of T=0s shows the region where the average displacement amplitude of the vibrating bubble was measured. The scale bar is 100 μm.

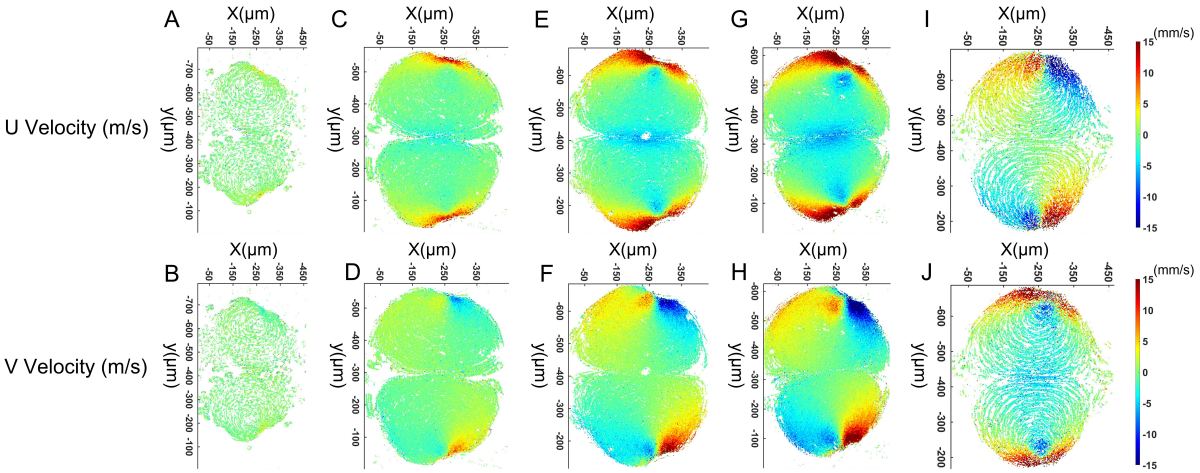

Figure S3 PTV analysis results of K562 cells orbiting in acoustic microstreaming vortices at (A&B) PZT voltage=2V, (C&D) PZT voltage=4V, (E&F) PZT voltage=6V, (G&H) PZT voltage=8V, (I&J) PZT voltage=10V

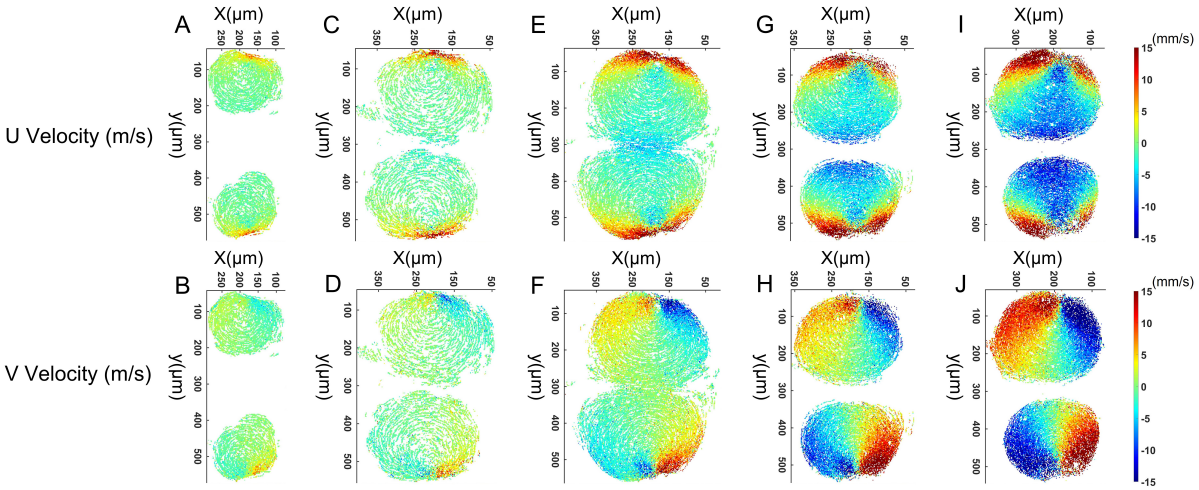

Figure S4 PTV analysis results of HeLa cells orbiting in acoustic microstreaming vortices at (A&B) PZT voltage=2V, (C&D) PZT voltage=4V, (E&F) PZT voltage=6V, (G&H) PZT voltage=8V, (I&J) PZT voltage=10V

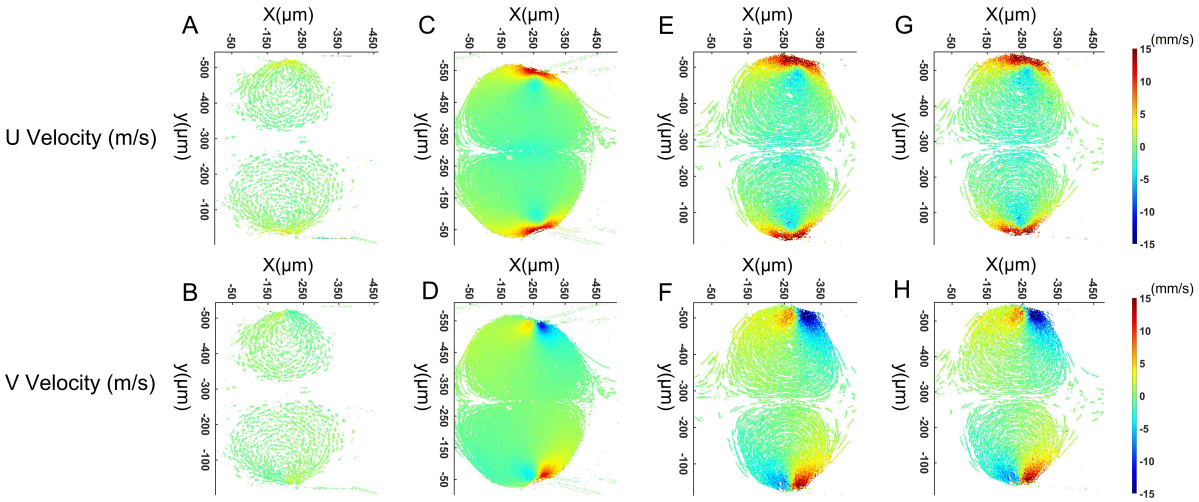

Figure S5 PTV analysis results of Jurkat cells orbiting in acoustic microstreaming vortices at (A&B) PZT voltage=2V, (C&D) PZT voltage=4V, (E&F) PZT voltage=6V, (G&H) PZT voltage=10V

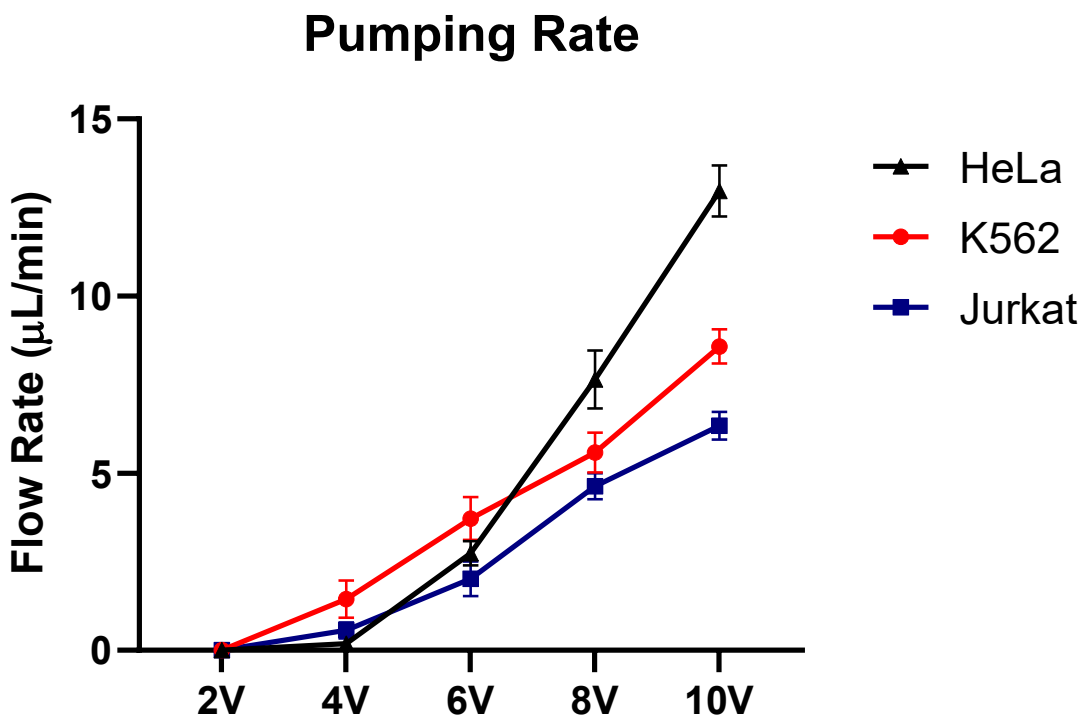

Figure S6 Device pumping rate at different PZT applied voltages for HeLa, K562, and Jurkat cells. The unique design of LCATs generates a bulk flow that eliminates the need and complexity of external pumping.

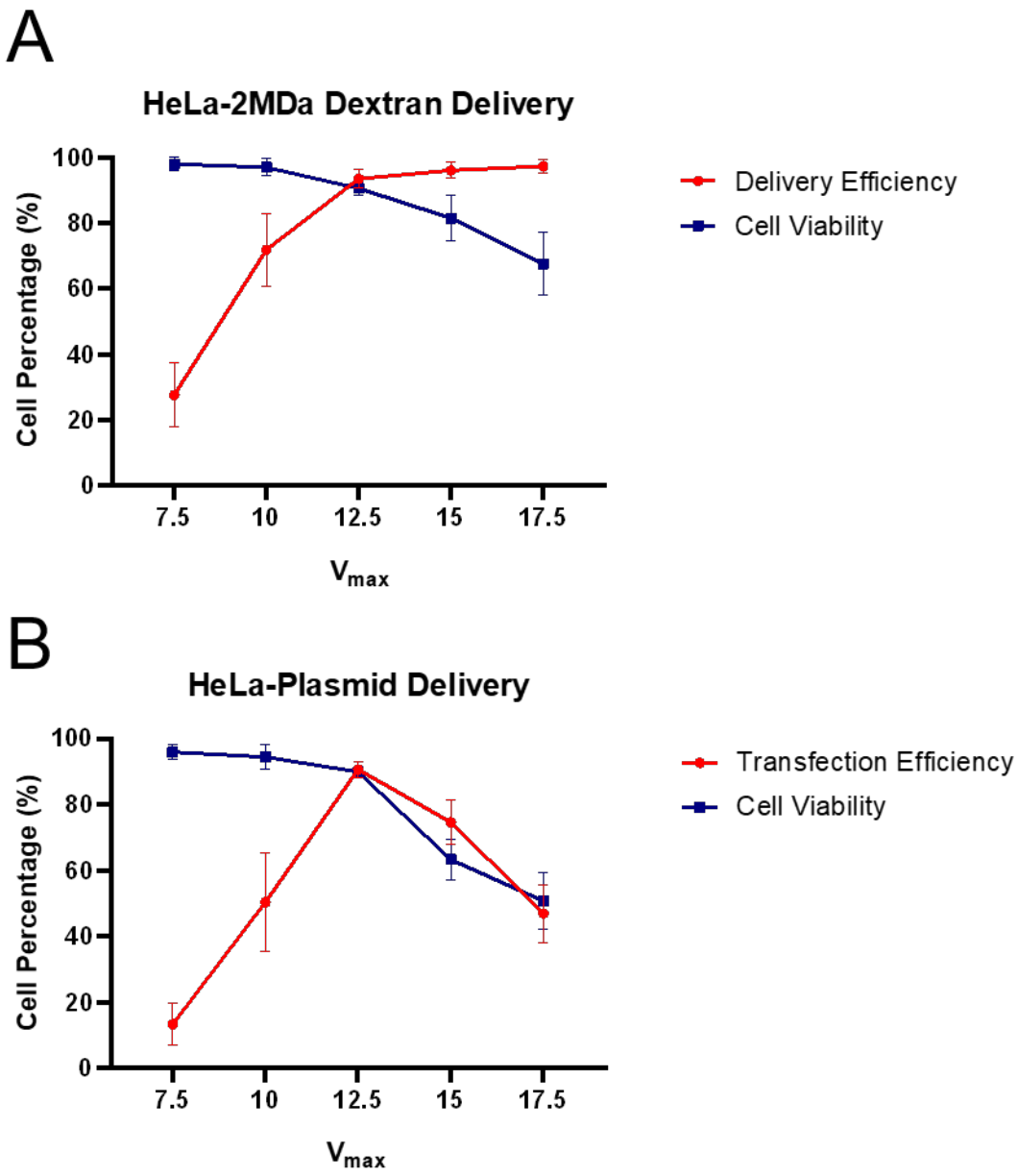

Figure S7 Optimization of electric field voltage (V_{max}) for (A) 2 MDa dextran delivery, and (B) eGFP plasmid transfection of HeLa cells at T=10ms and f=10kHz. Based on the results, V_{max}=12.5V was found as the optimum applied voltage that resulted in >80% transfection efficiency and >80% cell viability.

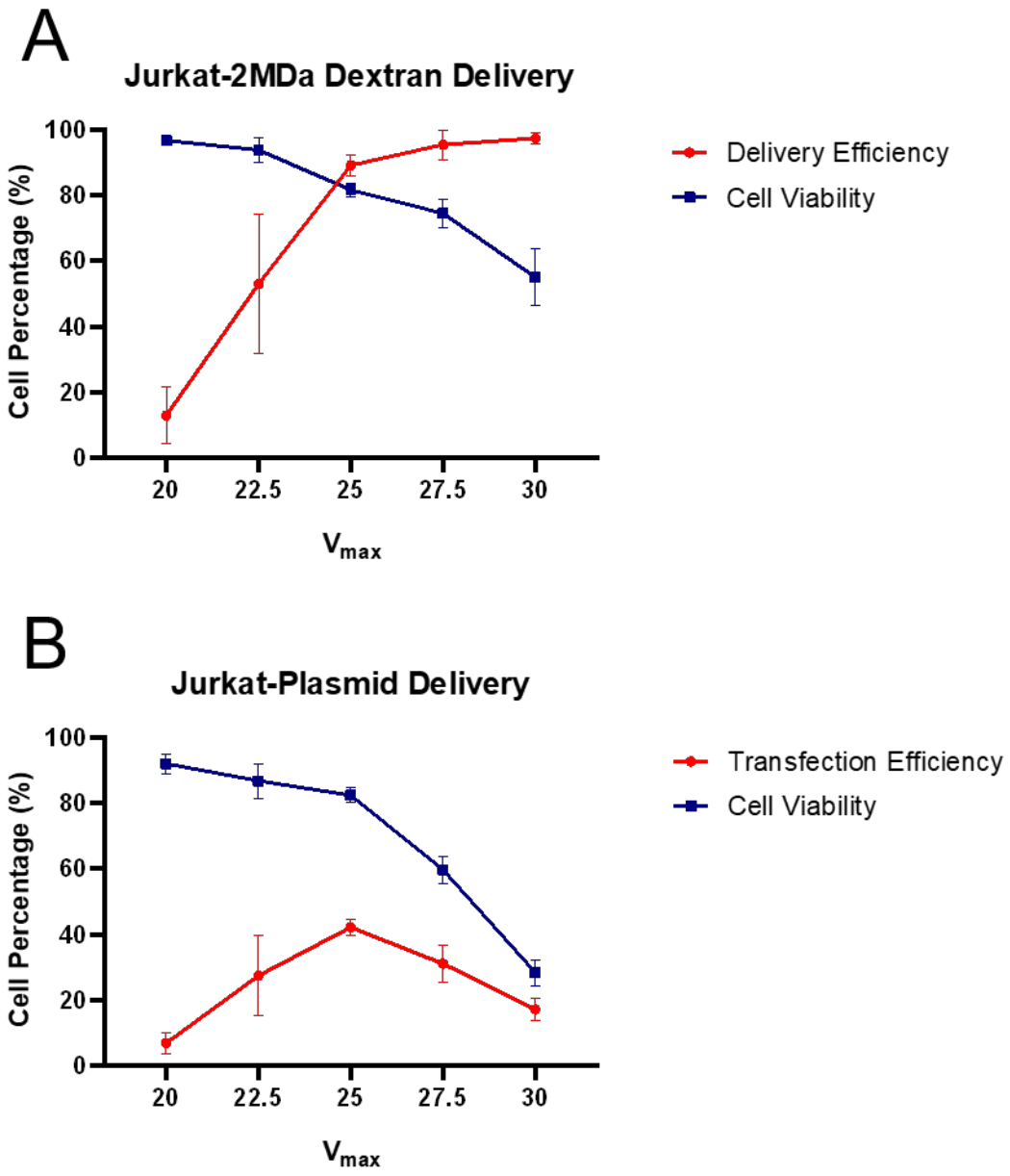

Figure S8 Optimization of electric field voltage (V_{max}) for (A) 2 MDa dextran delivery, and (B) eGFP plasmid transfection of Jurkat cells at T=10ms and f=20kHz. Based on the results, V_{max}=25V was found as the optimum applied voltage that resulted in >40% transfection efficiency and >80% cell viability (For better demonstration, the data points ±5V of optimum V_{max} are shown).

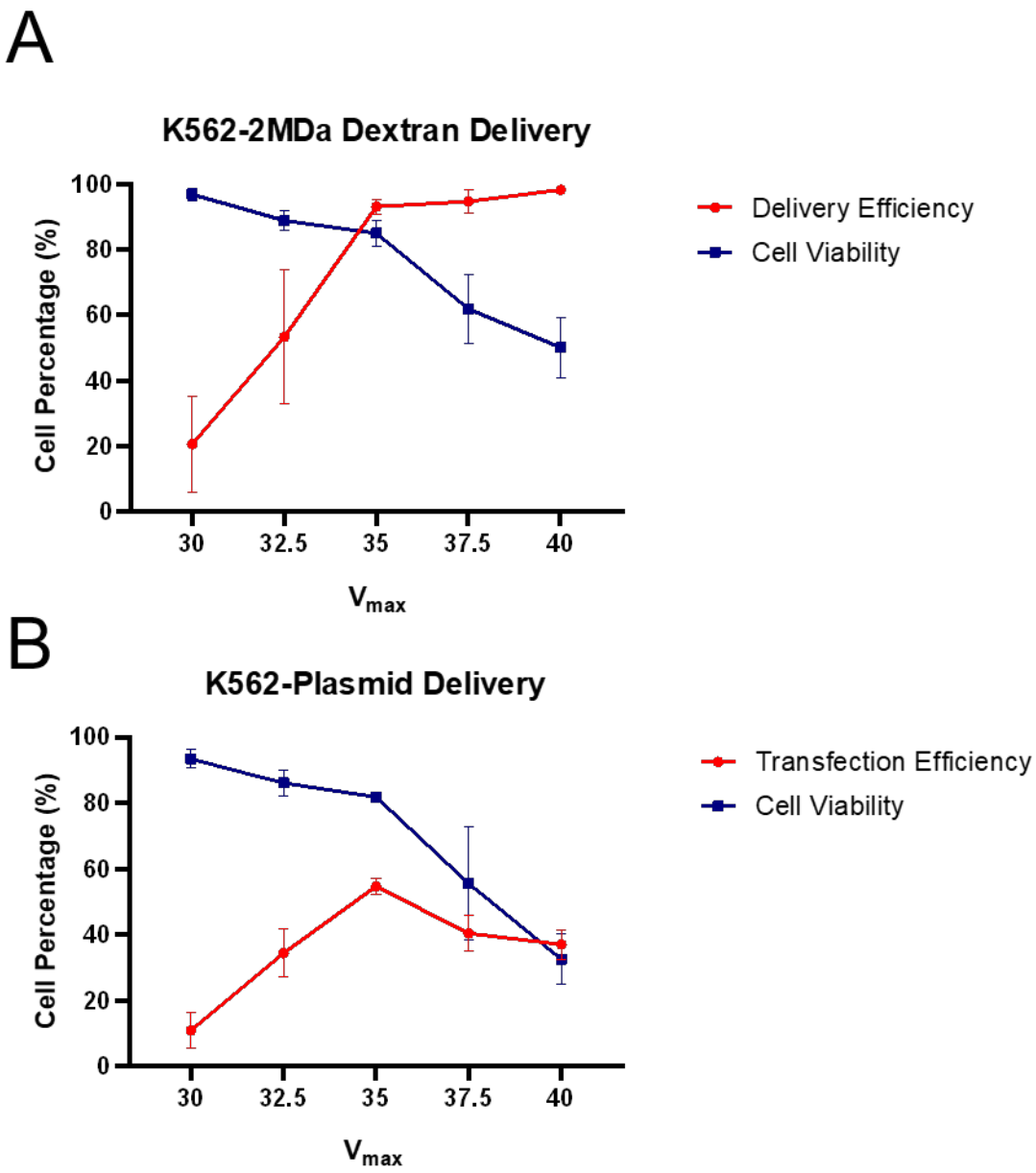

Figure S9 Optimization of electric field voltage (V_{max}) for (A) 2 MDa dextran delivery, and (B) eGFP plasmid transfection of K562 cells at T=10ms and f=30kHz. Based on the results, V_{max}=35V was found as the optimum applied voltage that resulted in >50% transfection efficiency and >80% cell viability (For better demonstration, the data points ±5V of optimum V_{max} are shown).

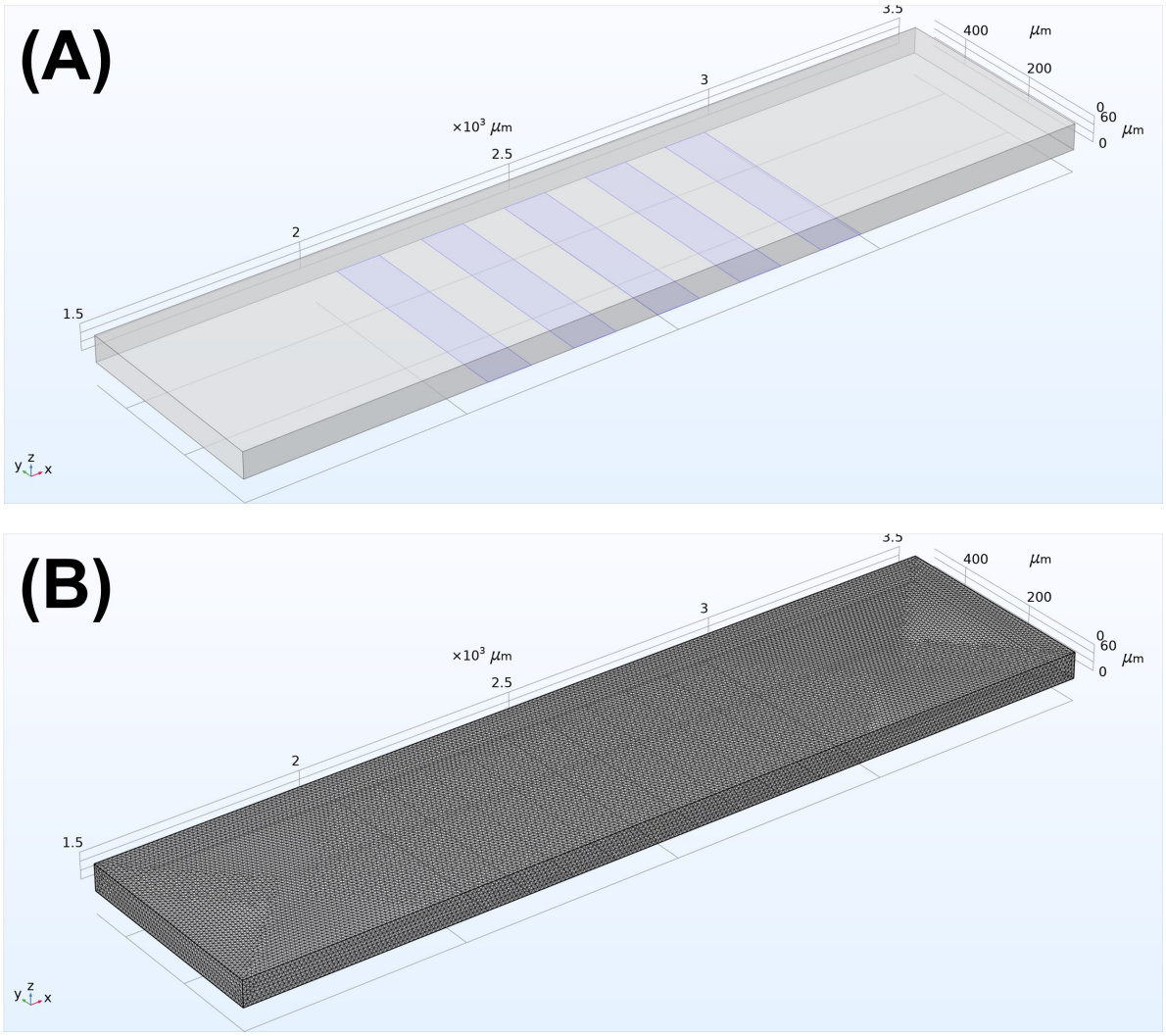

Figure S10 (A) a simplified 3D version of microfluidic channel with 5 interdigitated array (IDA) electrodes, and (B) 3D meshed model of the geometry mainly consists of tetrahedra elements with 2D triangular elements on faces and boundaries.

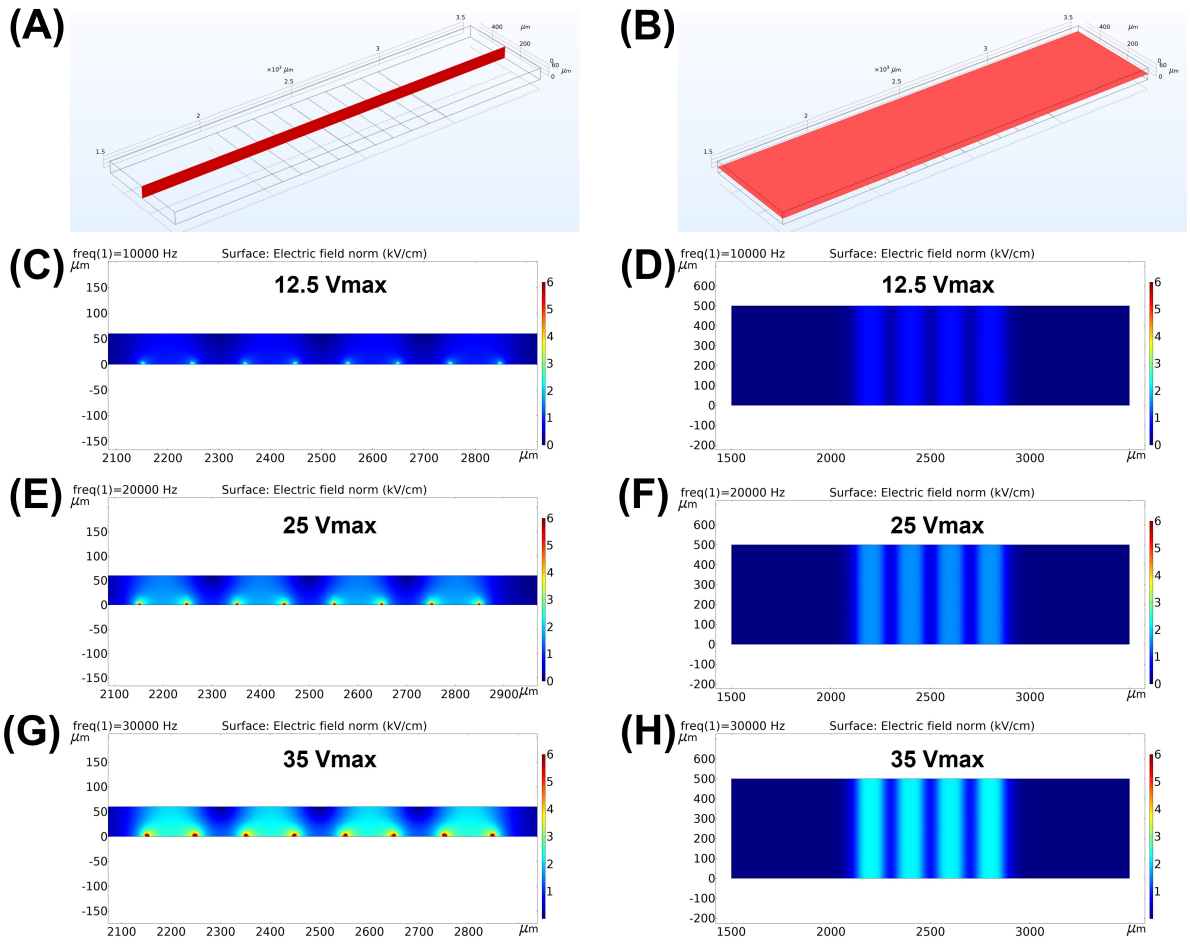

Figure S11 Electric field norm/strength distribution at (A) XZ plane (Y = 250 µm) and (B) XY plane (Z = 30 µm). The results are plotted for (C and D) 12.5 V_{max} and 10 kHz, (E and F) 25 V_{max} and 20 kHz, and (G and H) 35 V_{max} and 30 kHz.

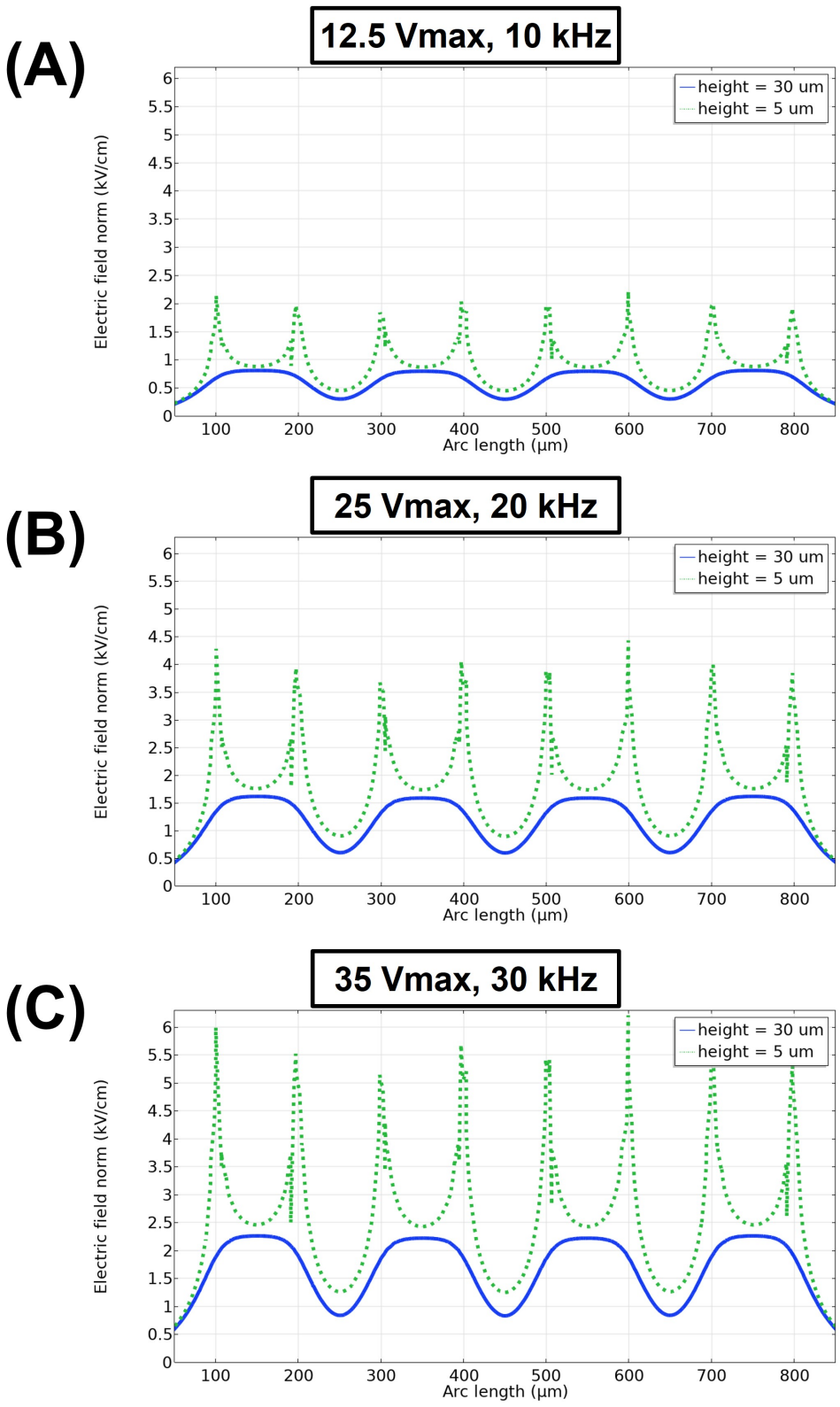

Figure S12 Electric field norm/strength variation at 30 μm (blue lines) and 5 μm (green dotted lines) above the interdigitated array (IDA) electrodes. The results are plotted for (A) 12.5 V_{max} and 10 kHz, (B) 25 V_{max} and 20 kHz, and (C) 35 V_{max} and 30 kHz.

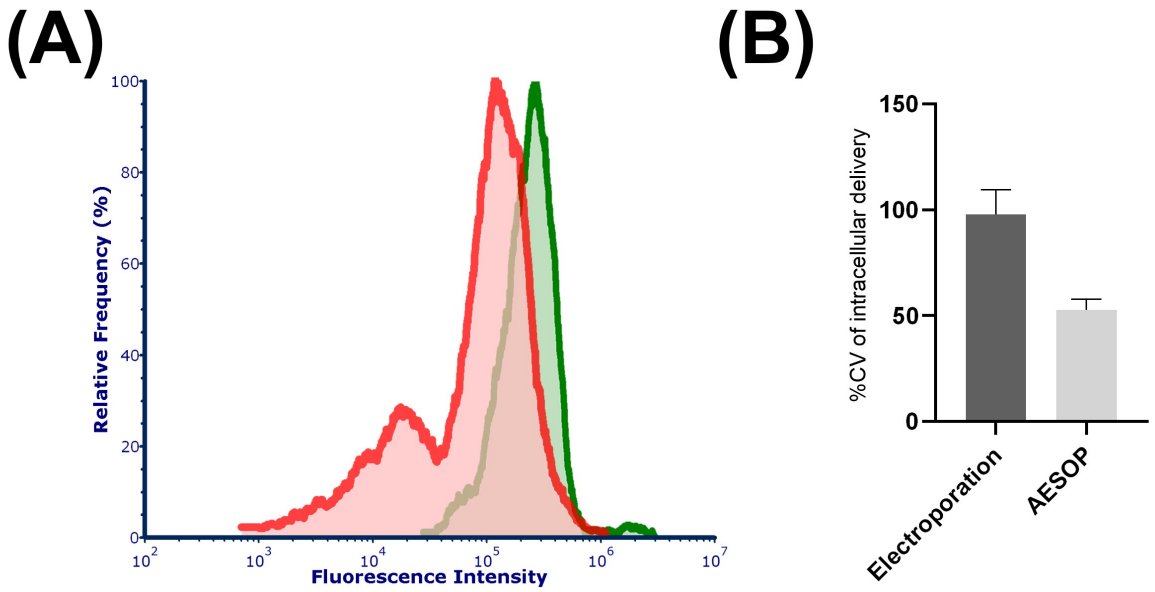

Figure S13 The histogram of fluorescent intensity of YOYO-1 labeled plasmid DNA delivered into K562 cells using Lonza Nucleofector™ (red) and AESOP (green), (B) the corresponding %CV of intracellular delivery for Lonza Nucleofector™ and AESOP

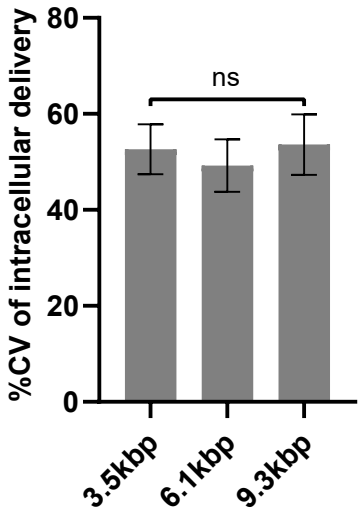

Figure S14 %CV for intracellular delivery of 3.5 kbp, 6.1 kbp, and 9.3 kbp plasmids into K562 cells. The results show that AESOP offers low and consistent %CV of intracellular delivery regardless of cargo size.

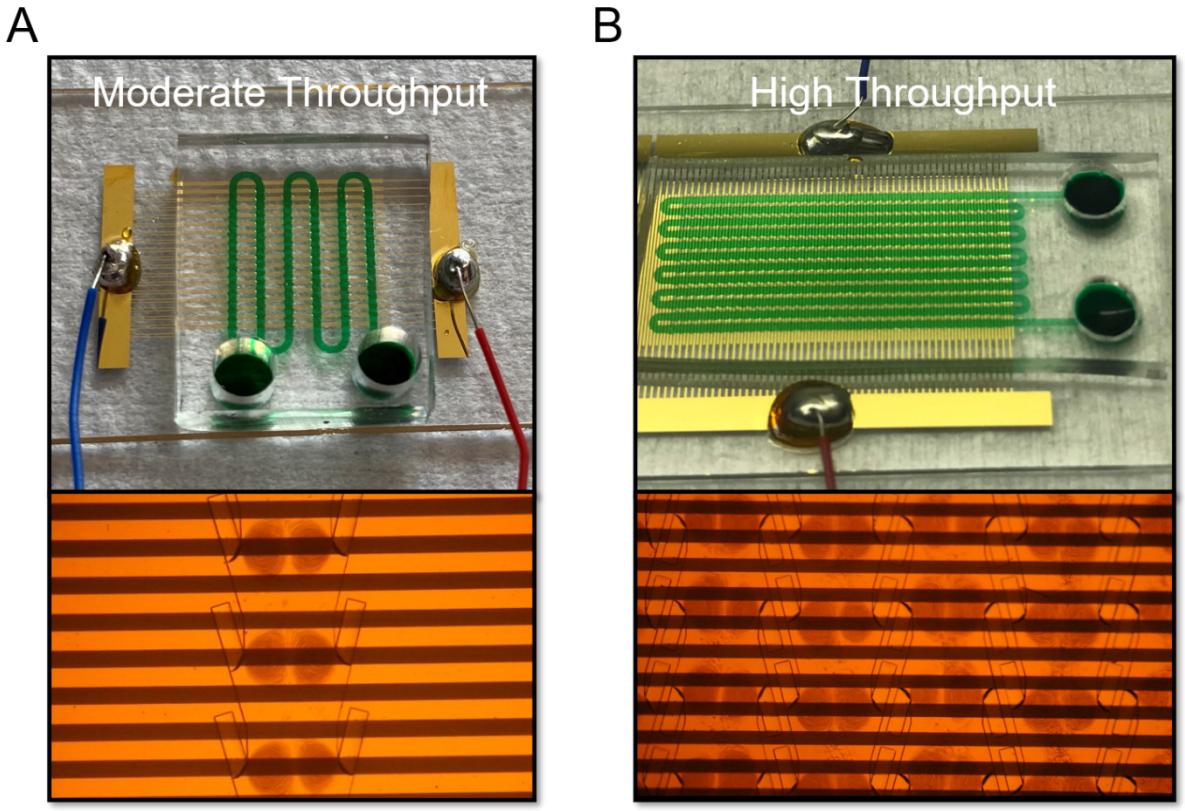

Figure S15 Two different AESOP versions. (A) Moderate throughput: capable of processing up to 200K cells/min, and (B) High throughput: capable of processing up to 1M cells/min

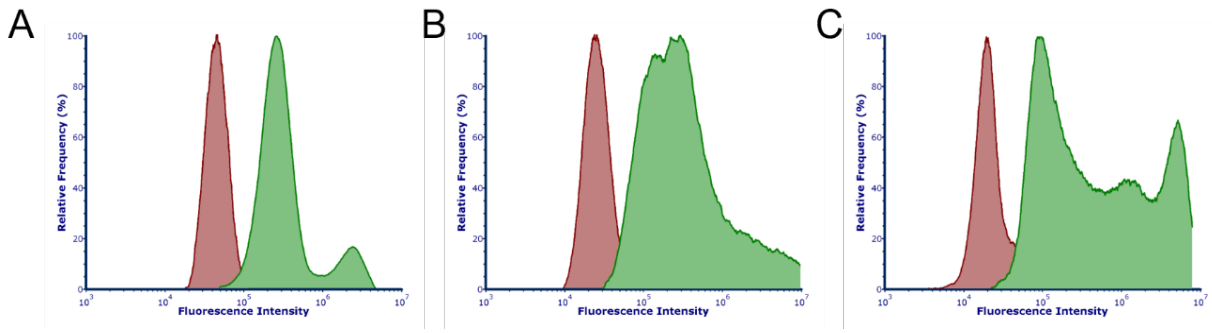

Figure S16 Flow cytometry quantification of eGFP expression for experimental (green) and control (red) groups for (A) HeLa, (B) Jurkat, and (C) K562 cells

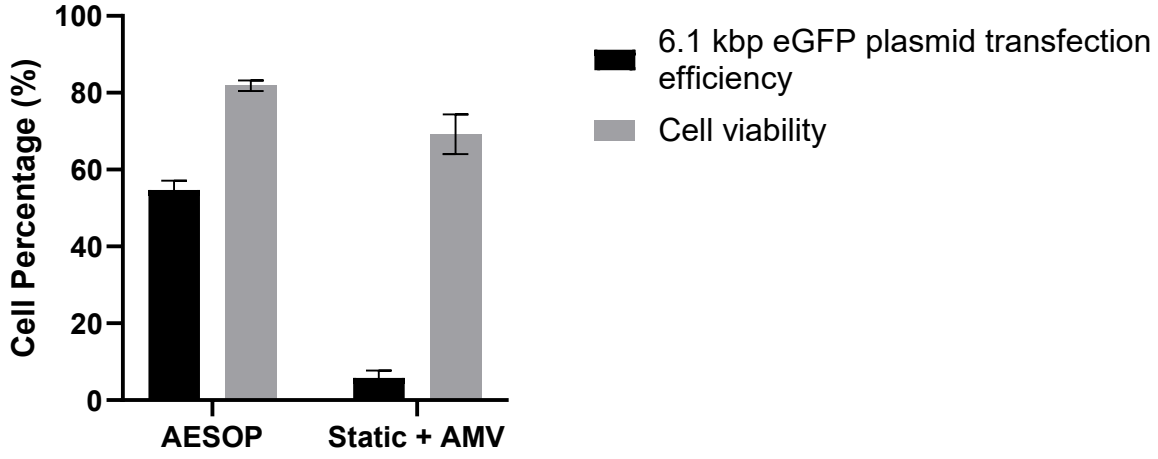

Figure S17 6.1 kbp eGFP plasmid transfection efficiency and the corresponding cell viability for AESOP and "Static + acoustic microstreaming vortices (AMV)" groups.

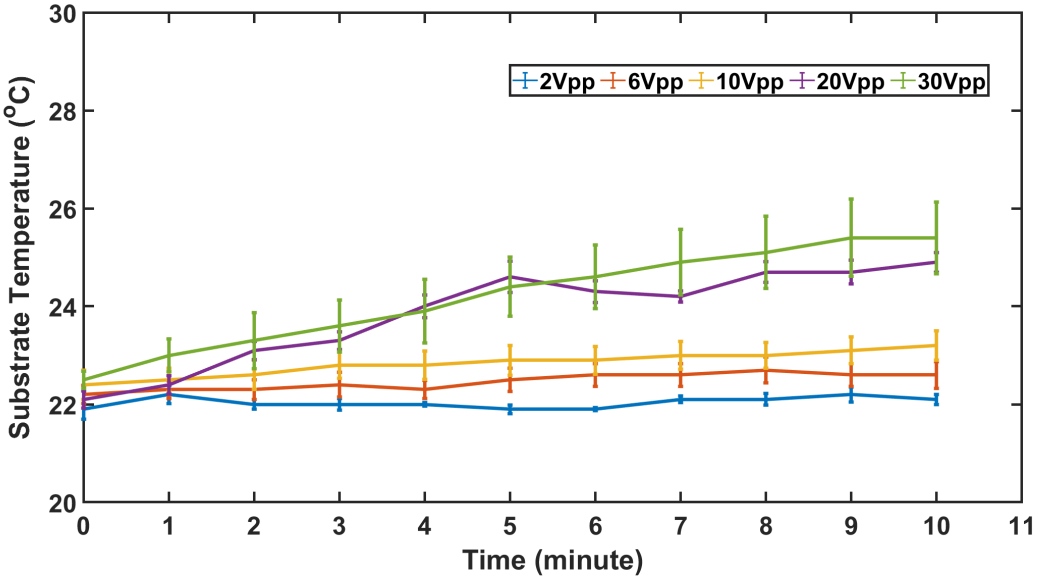

Figure S18 Measurement of substrate (glass placed on top of PZT with ultrasound gel smeared in between) temperature throughout 10 minutes operation of PZT for applied voltages of 2V, 6V, 10V, 20V, and 30V.

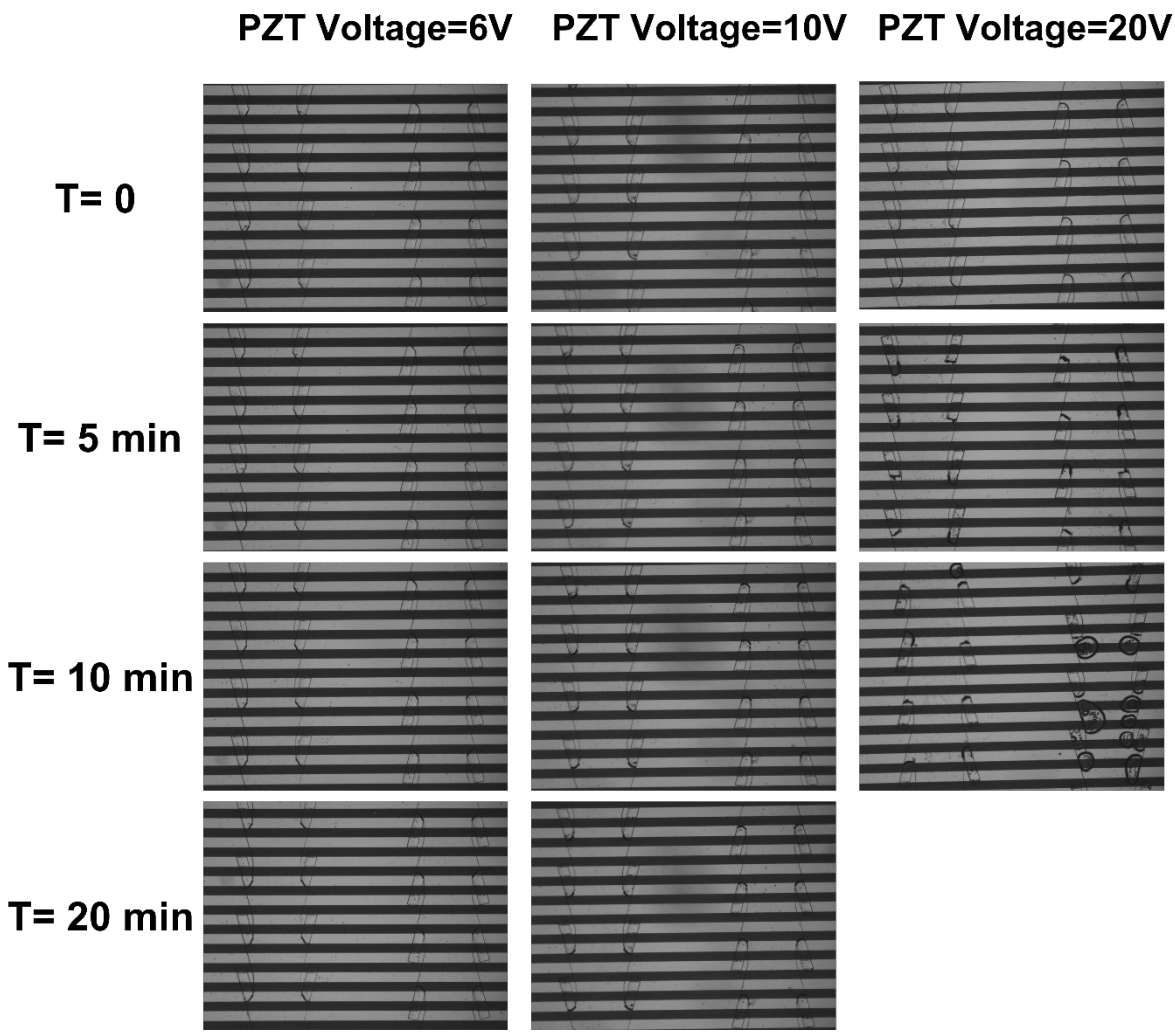

Figure S19 Investigation of stability of air-liquid interfaces at different PZT applied voltages. Based on the results, the interfaces are stable throughout 20 minutes system operation at applied voltages of 6V and 10V. However, at 20V, the interfaces become unstable. In addition, additional bubbles are generated possibly due to localized heating.

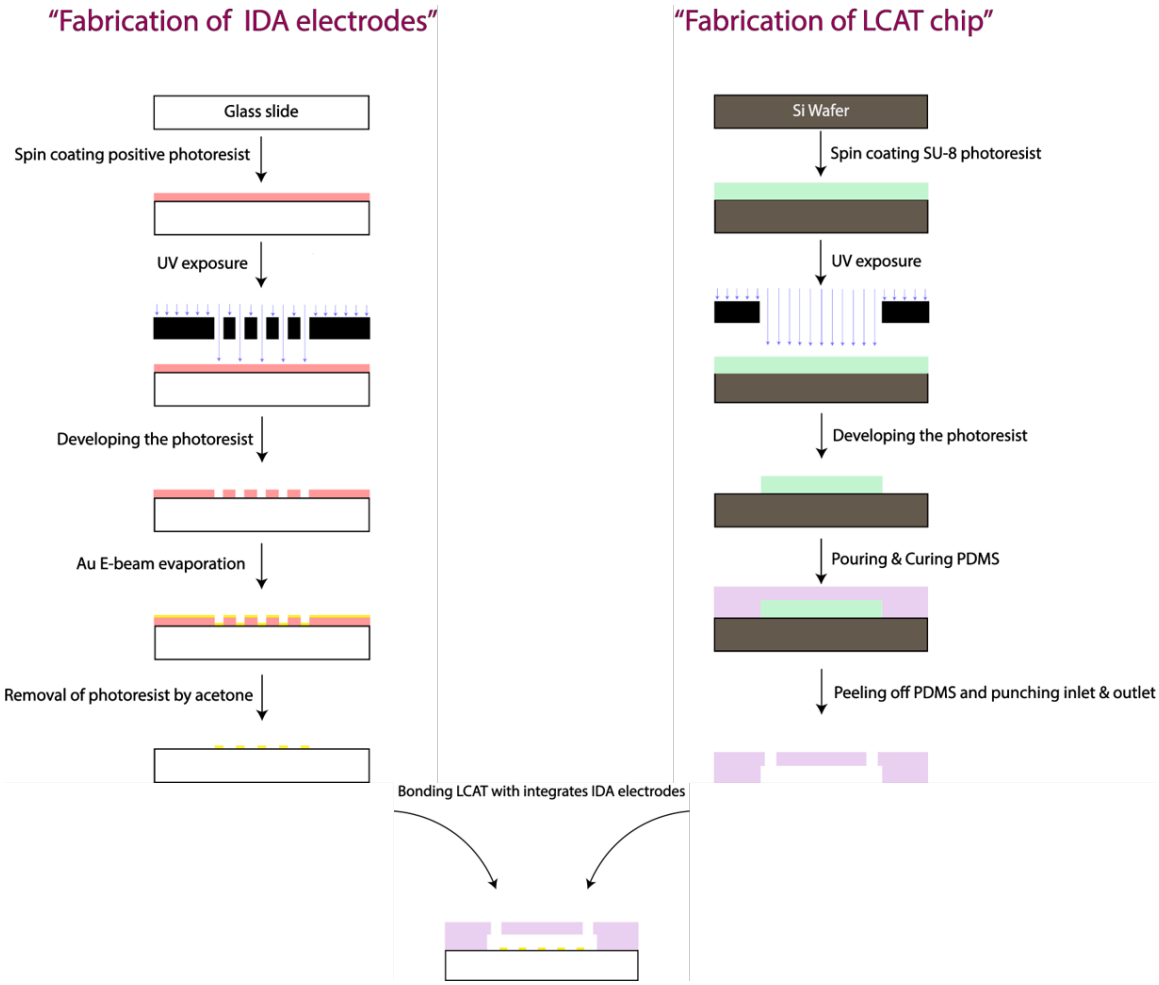

Figure S20 Schematics for device fabrication. AESOP integrates interdigitated array (IDA) electrodes with LCAT chip. Lift-off technique was adopted for batch electrode fabrication and soft lithography technique was employed for fabrication of the LCAT chip

DETAILED DESCRIPTION OF THE MOVIES

Movie 2.1 (separate file). Moderate-throughput AESOP platform for intracellular delivery of cargos into cells.

Video shows the cells that are trapped in the array of acoustic microstreaming vortices generated by the LCATs and are rotated on top of interdigitated array (IDA) electrodes. Moderate-throughput AESOP has a throughput of 200k cells/min. For this video, the camera captured 30 frames per second.

Movie 2.2 (separate file). High-speed video of a vibrating air-liquid interface in an LCAT device

Video shows an air-liquid interface vibrating when LCAT is actuated with PZT voltage of 10V and frequency of 50.2 kHz. The video is captured using a high-speed camera (Phantom, vision research) connected to a L150 Nikon Eclipse upright microscope. The video is recorded at 120000 fps and played back at 10 fps.

Movie 2.3 (separate file). LCAT technology for applying tunable mechanical shear on cells.

Video shows the cells trapped in acoustic microstreaming vortices at three different PZT applied voltages of 2V, 6V, and 10V. For this video, the camera captured 30 frames per second.

Movie 2.4 (separate file). High-throughput AESOP platform for intracellular delivery of cargos into cells.

Video shows the cells that are trapped in the array of acoustic microstreaming vortices generated by the LCATs and are rotated on top of interdigitated array (IDA) electrodes. High-throughput AESOP has a throughput of 1M cells/min. For this video, the camera captured 30 frames per second.

Movie 3.1 (separate file). Simulation results for droplet generation in 3D (Ca=0.12).

Movie 3.2 (separate file). Simulation results for droplet generation in 2D (Ca=0.12).

Movie 3.3 (separate file). The tracked trajectory of two particles of the same size (10 μm), trapped and recirculating in the two independent vortices

Movie 3.4 (separate file). Multimedia views of the symmetric three-dimensionally micro-vortices for the low (θ=120°) contact angle case.

Movie 3.5 (separate file). Multimedia views of the symmetric three-dimensionally micro-vortices for the high (θ=160°) contact angle case.